

Copyright
by
Jeremy Steven Ritter
2018

The Dissertation Committee for Jeremy Steven Ritter certifies that this is the approved version of the following dissertation:

Supernova-Driven Evolution of the First Stars and Galaxies

Committee:

Miloš Milosavljević, Supervisor

Volker Bromm

Steven L. Finkelstein

Mike Boylan-Kolchin

Ralf S. Klessen

Supernova-Driven Evolution of the First Stars and Galaxies

by

Jeremy Steven Ritter

Dissertation

Presented to the Faculty of the Graduate School of
The University of Texas at Austin
in Partial Fulfillment
of the Requirements
for the degree of
Doctor of Philosophy

The University of Texas at Austin

August, 2018

Supernova-Driven Evolution of the First Stars and Galaxies

by

Jeremy Steven Ritter, Ph.D.

The University of Texas at Austin, 2018

SUPERVISOR: Miloš Milosavljević

Heavy elements like carbon and oxygen are ubiquitous throughout the observed Universe yet only hydrogen, helium, and a few trace light elements are predicted to have been created in the Big Bang. Massive stars fuse light elements to form heavier elements during their brief lifetimes and die as supernova (SN) explosions that enrich the surrounding gas clouds. The chemical evolution history of a galaxy can be traced back through cosmic time from the highly enriched young stars like the Sun to the ancient, extremely metal-poor stars in the outer halo. This dissertation presents a series of high-resolution cosmological numerical simulations designed to explore the initial stages of SN-driven galactic evolution, from the collapse of the very first stars in unenriched dark matter halos to the formation of hot, enriched outflows in a first galaxy. These 3D hydrodynamical simulations of discrete, expanding SN remnants show that they were capable of enriching their host dark matter mini halos and the surrounding gas sufficiently to satisfy the theoretical minimum threshold required to form new low mass metal-enriched stars. Hydrodynamical biases skew our ability to trace the enrichment of individual stars back to a single progenitor SN, however there is hope that we can characterize the enrichment signature of the first stars from the elemental abundance trends observed in the most ancient, metal-poor stars. Primordial gas enriched by a single progenitor SN, assuming Type II-like yields, can have abundance ratios that fall within the parameter-space for the observed populations of extremely metal-poor stars. Finally, galactic outflows are a common feature found in the outer halos of star-forming galaxies. It has long been theorized that the combined effects of many SNe could be responsible for powering the supersonic velocities observed in these outflows. A pilot simulation is performed to explore the effects of a continuous succession of discrete SNe, exploding one at a time in a small starburst galaxy, the results of which will provide insights

into the expected thermodynamic and spectroscopic features we might expect when future missions like the James Webb Space Telescope begin to unlock this era in our cosmic history.

Table of contents

List of Figures	ix
Chapter One: Introduction	1
1.1 Supernovae of the first stars	2
1.2 Hydrodynamical bias in metal enrichment	3
1.3 Enriching the most ancient metal-poor stars	4
1.4 Supernova-driven outflows from the first galaxies	5
Chapter Two: Confined Population III enrichment and the prospects for prompt second-generation star formation	7
2.1 Simulating a Supernova in a Minihalo	10
2.1.1 Cosmological Initial Conditions and Gravity	10
2.1.2 Chemistry and Cooling	11
2.1.3 Adaptive Mesh Refinement Strategies	14
2.1.4 The First Star and Ionizing Radiation Transfer	14
2.1.5 Supernova and Metal Transport	17
2.2 Results	17
2.2.1 The HII Region	19
2.2.2 blast wave Evolution and Fallback	21
2.2.3 Metal Enrichment	26
2.3 Discussion	30
2.3.1 Metal-Enriched Star Formation: Continuous, Bursty, or Self-Limiting?	32
2.3.2 Uncertainties Related to the Nature of First Stars	34
2.4 Conclusions	36

Chapter Three: Metal transport and chemical heterogeneity in early star forming systems	38
3.1 Numerical Methodology	40
3.1.1 Thermodynamic Evolution	42
3.1.2 Adaptive Mesh Refinement Control	44
3.2 Hydrodynamic Evolution	46
3.3 Monolithic and Biased Enrichment	49
3.4 Confronting the Empirical Record	52
3.5 Summary and Conclusions	54
Chapter Four: Toward <i>ab initio</i> extremely metal poor stars	56
4.1 Numerical methodology	59
4.2 Results	64
4.3 Analysis and discussion	68
4.3.1 Metal enrichment	68
4.3.2 Cooling thresholds	69
4.3.3 Gravitational instability	71
4.3.4 The relation to extremely metal-poor stars	74
4.4 Summary	75
Chapter Five: Simulating galactic outflows one supernova at a time	79
5.1 The First Galaxies	82
5.1.1 Modeling the First Galaxy	83
5.1.2 Stars in the First Galaxy	84
5.1.3 Supernovae in the First Galaxy	85
5.1.4 Hot Winds in the First Galaxy	93
5.2 Numerical Methods	95

5.2.1	FLASH Configuration	96
5.2.2	Initial Conditions	97
5.2.3	Stellar Feedback	98
5.2.4	Supernova Feedback	100
5.3	Results	102
5.3.1	HII Region	102
5.3.2	Superbubble Expansion	106
5.4	Discussion	109
5.4.1	Snowplow Breakout	109
5.4.2	Towards Simulating Galactic Outflows One Supernova at a Time . .	110
5.5	Summary	112
Chapter Six: Conclusion		114
Bibliography		117

List of Figures

- 2.1 The halo mass M_{200} and radius R_{200} as a function of redshift, over the course of 50 Myr. The dotted line marks the formation of the star, and dashed line the supernova explosion. The steps are an artifact of the method we use to estimate R_{200} 13
- 2.2 Density-temperature phase plot for the gas within 1 kpc (physical) from the center of the minihalo at redshifts, from left to right, $z = 19.7$ (right before the insertion of the star), $z = 19.5$ (in the Sedov-Taylor phase of the supernova, 8 kyr after the explosion), and at $z = 17$ (end of the simulation, 40 Myr after the explosion). By the end of the simulation, the gas heated by photoionization and the supernova has cooled and the halo has resumed central gravitational collapse, albeit at four times higher halo mass and now a nonzero metallicity. The dashed line shows the CMB temperature. 13
- 2.3 Spherically averaged density (upper panel) and radial velocity (lower panel) profiles for all baryons (blue line) and the ionized gas (red line), before the insertion of the star at $z = 19.7$ (dashed lines), and before the insertion of the supernova at $z = 19.5$ (solid lines). For reference, we also show the density profile of gravitational mass density (including dark matter) in the units of the proton mass (black line). The neutral gas density peak located inside the HII region is a clump of dense neutral gas that has withstood photoionization. The gas with positive (negative) radial velocity is flowing away from (toward) the star. 18
- 2.4 Volume rendering of the number density of neutral (left panel) and ionized (right panel) hydrogen at $z = 19.5$, right before the insertion of the supernova, in a 200 pc cube centered on the star particle. The colors show gas density ranges (in units of cm^{-3}) as indicated in the legend. The densest ionized gas clumps $n_{\text{HII}} > 10^{-1} \text{cm}^{-3}$ in the center of the cube seem to be fed by photoablation from even denser, $n_{\text{HI}} > 10^{1.5} \text{cm}^{-3}$, persistent cold neutral clumps in this region. 19
- 2.5 Baryon mass-weighted projection of hydrogen density, temperature, and fluid-based metallicity in units of the solar metallicity 8.5 Myr after the explosion. The circle shows the virial radius of the halo, which is here 180 pc (physical). 21

- 2.6 Characteristic radii corresponding to Lagrangian mass coordinates enclosing baryonic masses of, from top to bottom, $(2, 1.0, 0.5, \dots) \times 10^6 M_\odot$ (left panel; the masses are labeled on the curves in the units of M_\odot) and ejecta mass fractions, as tracked by passive tracer particles, of $(100\%, 50\%, 25\%, \dots)$ (right panel; percentages are labeled on the curves), both as a function of time since the explosion. The dotted line shows the virial radius R_{200} of the host halo. The baryonic radii are computed from the gravitational potential minimum of the halo. Supernova-driven expansion is evident in the mass coordinates inside the virial radius, but all mass coordinates return to infall owing in part to a persistent filamentary streaming of fresh, cold baryons from the cosmic web into the halo center. For ejecta radii, at times $t < 0.02 \text{ Myr}$, the location of the progenitor star is taken as the coordinate origin; at later times, the origin is the location of the gravitational potential minimum; the change of origin is visible as a discontinuity in the curves. By the end of the simulation, a half of the ejecta has turned around and is falling back toward the center of the halo. At late times, the curves plunge steeply as the material approaches the central unresolved fluid elements with a finite free-fall velocity. 23
- 2.7 Metal dispersal and fallback at the end of the simulation, 40 Myr after the supernova explosion, at $z = 17$. The left panel is 1.1 kpc (physical) wide and centered on the gravitational potential minimum; the right panel is a 360 pc detail. The black points are the metal particles in projection, while the color shows a slice through the physical hydrogen density n_H . Metal-bearing Rayleigh-Taylor fingers have a positive radial velocity and have breached the virial radius of the halo, while a majority of the metal mass is falling back into the halo center and remains incompletely mixed with the primordial gas. Density in the central unresolved core exceeds coverage of the color scale and is $\sim 10^4 \text{ cm}^{-3}$ 25
- 2.8 Metal (lower curve; \dot{M}_Z) and total baryon (upper curve; \dot{M}_b) net mass flow rate through a sphere of radius 20 pc centered on the gravitational potential minimum. Dashed lines indicate outflows and solid lines inflows. The total mass of ejecta in the simulation is $M_{SN} = 40 M_\odot$ and the metal mass is $M_Z = Z_{SN} M_{SN} = 4 M_\odot$. Net outflow reverses into an inflow earlier in the baryons because of the presence of cold filaments delivering metal-free gas from the cosmic web into the halo center. 28

2.9	<p>Absolute metallicity distribution at four different times after the supernova. The histograms show the fraction of total metal mass as a function of absolute metallicity calculated in three different ways: by computing the metallicity and metal mass from the fluid variables defined on the AMR grid (black curve), by computing metallicity from the fluid variables and metal mass from the Lagrangian particles tracing the supernova ejecta assuming ejecta metallicity of $Z_{SN} = 0.1$ (red curve), and by computing both metallicity and metal mass with the Lagrangian particles (blue curve). The blue column in the first histogram shows the initial metallicity of the ejecta. The peak at $Z \approx (2, 0.7, 0.3) \times 10^{-4}$ at $t - t_{SN} = (1.187, 13.367, 40.127)$ Myr contains the fluid that has become incorporated in the central unresolved core (please see text for additional explanation).</p>	29
2.10	<p>The kinetic (blue curve), internal (green curve), and combined kinetic and internal (red curve) energy of the metal enriched fluid, defined as the fluid with absolute metallicity $Z \geq 10^{-6}$.</p>	30
3.1	<p>Simulation 7SN 200 Myr after the first supernova explosion: density-weighted density projection ($\int \rho^2 dz / \int \rho dz$, left), metal-density-weighted metal density projection ($\int \rho_Z^2 dz / \int \rho_Z dz$, middle), and metallicity slice through the cell with maximum density (right). The metal density is derived from the advected passive scalar tracing supernova ejecta. The cosmic web filament extends diagonally from top left. Note the relatively low metallicity near the center, resulting from a dilution of supernova ejecta with metal-free gas streaming down the cosmic web filament.</p>	41
3.2	<p>A slice of vorticity magnitude $\nabla \times \mathbf{v}$ in the center of 1SN (left) and 7SN (right) overplotting ejecta tracer particles in a 5 pc thick slab containing the slice (black dots). Note that metal ejecta are unmixed outside the central high-vorticity core, tens of parsecs in radius.</p>	46
3.3	<p>Metallicity as a function of gas density at the end of the simulation 1SN at 56 Myr after the first explosion (left plot) and 7SN at 200 Myr after the first explosion (right plot). From red to blue, the color scales with the logarithm of the fluid mass in the density and metallicity bin. Solid curve is the mean metallicity and colored curves are the fractional contributions from the seven radial mass bins (1SN) and seven supernovae (7SN).</p>	48

- 4.1 Number density projections (density-weighted, color scale showing $m_{\text{H}}^{-1} \int \rho^2 dz / \int \rho dz$) centered on the densest gas cell at the end of the simulation, 13.7 Myr after the explosion. The top-left panel shows the cosmic web filaments feeding into the halo center. The supernova ejecta bubble extends beyond the virial radius $r_{\text{vir}} = 175$ pc. The top-right panel shows that the dense neutral clouds that have survived photoionization are streaming into the halo center marked with a white “×”; the tip of a cosmic web filament is still a few dozen parsecs away. The bottom-right shows dense, self-gravitating clumps at the apocenter of an elliptical gas flow pattern. Each clump contains a few hundred solar masses of gas. The clumps loiter at density $n_{\text{H}} \sim 10^4 \text{ cm}^{-3}$ for several million years and then enter runaway collapse. The bottom-left panel shows the first runaway clump in which the collapse facilitated by metal line cooling rapidly increased the density above $n_{\text{H}} > 10^8 \text{ cm}^{-3}$ 61
- 4.2 The same as Figure 4.1, but now showing metallicity projection (density-weighted, color showing $Z_{\odot}^{-1} \int Z_{\text{scal}} \rho dz / \int \rho dz$). Here we overplot density contours to provide context for the clumps and filament locations. In the bottom panels we also overplot metal tracer particles. 62
- 4.3 A slice through the cold cloud that would ultimately collapse and fragment into metal-enriched pre-stellar clumps showing passive scalar metallicity (left panel) and temperature (right panel) with gas density contours overplotted. Also overplotted are Lagrangian passive ejecta tracer particles (white dots) in a 1 pc thick slab containing the slice. Note the superficial enrichment of the cloud as well as evidence of numerical passive scalar diffusion where the scalar metallicity is $> 10^{-6} Z_{\odot}$ and yet no particles are present. 63
- 4.4 Density-temperature phase diagrams for gas within 1 kpc of the minihalo at the end of the simulation, 13.7 Myr after the explosion. The color scale shows the mass-weighted average metallicity (left panel) and the relative log-metallicity dispersion (right panel). Dispersions near unity reflect unmixed, chemically heterogenous medium whereas lower values indicate homogenization. The densest gas with metallicity $\bar{Z}_{\text{scal}} \approx 10^{-3.3} Z_{\odot}$ has very low dispersion. We also show the lines of constant entropy (dotted; see Equation 4.3 and Figure 4.5). The solid line is the cosmic microwave background temperature $T_{\text{CMB}} = 53 \text{ K}$ at redshift $z = 18.5$ 66

- 4.5 Metallicity-entropy phase diagram for gas within 1 kpc of the minihalo at the end of the simulation, 13.7 Myr after the explosion. Entropy here is as defined in Equation 4.3. Very low metallicity gas $Z_{\text{scal}} \leq 10^{-6} Z_{\odot}$ was placed in the leftmost column. The color scale is the total gas mass contained in each two-parameter bin. The unmixed, diffuse, shocked ejecta, some of which escaped the halo, are on the upper-right. The shock-heated dense clouds that were blasted with metals have cooled and homogenized near metallicity $\sim 10^{-3.3} Z_{\odot}$ and then undergo gravitational collapse to form the low-entropy peninsula in the bottom-middle. 70
- 4.6 Mass profile plots of the enclosed mass as well as the thermal (Eq. 4.4) and turbulent (Eq. 4.5) Jeans masses, all calculated using averages within a sphere centered on the densest cell. We shade the region red, light blue, or dark blue, depending on whether neither or only the thermal criterion, or in turn both criteria are satisfied. The left panel at 12.6 Myr is before the onset of collapse, when the gas density loitered at $n_{\text{H}} \sim 10^4 \text{ cm}^{-3}$ and the enclosed mass was well below the Jeans mass (minimum cell size $\Delta x = 0.02 \text{ pc}$). The middle panel at 13.3 Myr is on the cusp of runaway gravitational collapse when the enclosed mass has exceeded the thermal Jeans mass on radial scales of $\sim 1 \text{ pc}$ ($\Delta x = 0.01 \text{ pc}$). The panel on the right at 13.7 Myr is when the gas has entered runaway collapse and the enclosed mass has exceeded the thermal and turbulent Jeans masses on all scales shown between 0.01 and 1 pc ($\Delta x = 4 \times 10^{-4} \text{ pc}$). 72
- 4.7 Chemical abundance log-ratios $[\text{Fe}/\text{H}]$ and $[\text{C}/\text{Fe}]$ in the known metal-poor stars compiled from Caffau et al. (2011), Yong et al. (2013a), Norris et al. (2013), Keller et al. (2014), and Howes et al. (2015). The stars are colored depending on whether they are normal (black) or carbon-rich without (red) or with neutron capture enhancement (blue). Metal-poor stars from the Galactic bulge are identified using crosses, while all other stars are identified using circles. The carbon-rich, iron-poor star SMSS J031300.36-670839.3 (Keller et al., 2014) is an open red circle. The carbon-normal, iron-poor star SDSS J102915+172927 (Caffau et al., 2011) is an open black circle. The diagonal dashed lines trace constant $[\text{C}/\text{H}]$, which, assuming $[\text{C}/\text{O}] \approx 0$, is approximately equal to the metallicity. The shaded region $-3.8 < [\text{C}/\text{H}] < -3.3$ represents the stars that could have formed in our simulated gas clump assuming a range of carbon enhancements $1 < [\text{C}/\text{Fe}] < 4$ 76

5.1	Face-on (<i>left column</i>) and edge-on (<i>right column</i>) projections of the density-weighted average number density (cm^{-3}) of the host galaxy disk before photoionization (<i>top row</i>), and after 3.25 Myr (<i>bottom row</i>). The black 'x' denotes the gravitational galactic center and location of the radiative point source. The virial radius at $R_{\text{virial}} = 3 \text{ kpc}$ is beyond the edge of these images. After photoionization, the thin host disk has been disrupted and the satellite halos are puffed up.	103
5.2	Radial profiles of the volume averaged density (top) and the mass averaged temperature (bottom) for photo-heated gas prior to the first SN explosion. Radial profiles are shown for $t = 0$ and 3 Myr after the initial starburst. The dotted line shows the 1d solution (Shu et al. 2002).	104
5.3	Maximum radius of the SB as a function of time (solid black), defined by the maximum distance from any SN explosion origin to its farthest tracer particle. The black dashed line shows the ST and PDS phase evolution for a single SN with fixed ambient density $n_{\text{amb}} \sim 30 \text{ cm}^{-3}$. The black dotted line shows the evolution of a continuous PDS with $\Delta t_{\text{sn}} = 66 \text{ kyr}$, where the ambient density $n_{\text{amb}} \sim 10 \text{ cm}^{-3}$ has been reduced to account for the decreasing density gradient outside the vicinity of the central gas cloud. Horizontal red dotted lines mark the scale height H and $2H$. The red vertical ticks indicate the temporal position of SNe numbers 2 through 10.	107
5.4	Phase plot of the radius vs radial velocity at $t = 1.9 \text{ Myr}$ after the first SN, with the mass-averaged temperature in color. The black dotted line approximates the local escape velocity $v_{\text{escape}} \sim \sqrt{2GM(r)/r}$. The red dashed lines represent the galaxy escape velocity (horizontal) and the virial radius of the galaxy (vertical). Note the temperature gradient between 25 and 90 pc that highlights the asymmetrical snowplow shell, and the presence of fast-moving hot gas behind it.	108

Chapter One: Introduction

Cosmic star formation drives the hydrodynamical evolution of galaxies by feeding energy back into the gas that has yet to collapse and form stars. Stellar radiative feedback heats and ionizes nearby gas, increasing the pressure and resisting gravitational infall that ultimately leads to the formation of new stars. On the other hand, nucleosynthesis transforms hydrogen and helium inside stars into heavier elements, known collectively as "metals" to astronomers, that aid in the cooling and collapse of ionized gas. Massive stars can explode as supernovae (SNe) at the end of their lives, ejecting the heavy elements they have synthesized back into the circumstellar medium. The precise balance of energetic feedback, metal-enhanced cooling, and gravity act together to regulate the rate of star formation in a galaxy. If there are too few stars then cooling can be more efficient than heating and gravity wins, however too many stars will keep the gas hot and prevent more stars from forming.

The early Universe contained only hydrogen, helium, and trace light elements following its creation in the Big Bang. The first stars, Population III (Pop III), formed from this primordial metal-free gas and began the process of nucleosynthesis. Early investigations concluded that the Pop III stars were characteristically massive (Bromm, Coppi & Larson, 1999, 2002; Abel, Bryan & Norman, 2000, 2002; Gao et al., 2007; O’Shea & Norman, 2007, $\gtrsim 100 M_{\odot}$), due to the lack of metals that aid in cooling during their formation in cosmic dark matter mini halos. In more recent works, fragmentation (Stacy, Greif & Bromm, 2010; Clark et al., 2011a; Greif et al., 2011, 2012) and radiation-limited accretion (McKee & Tan, 2008; Hosokawa et al., 2011; Stacy, Greif & Bromm, 2012a,b; Stacy, Bromm & Lee, 2016) have been shown to produce Pop III stars with masses on the order of $\sim 10 M_{\odot}$. No extant Pop III stars have yet been discovered so their initial mass function (IMF) remains theoretical and uncertain, yet consensus still holds that the Pop III IMF was characteristically more top heavy than the low-mass-dominated IMF observed in metal-poor Pop II and chemically mature Pop I stars (Chabrier, 2003). In the following sections we introduce a series of high-resolution cosmological numerical simulations that explore the hypothesis that the signature of moderate mass Pop III stars imprinted on their host mini halos and descendant stellar populations differs in observable ways from the signatures of exotic or very massive stars.

1.1 Supernovae of the first stars

It is expected that metal-free stars with masses $15 - 50 M_{\odot}$ undergo core collapse after exhausting their nuclear fuel, and explode as Type II-like SNe (e.g., Heger & Woosley, 2002; Heger et al., 2003). When a Pop III star explodes the momentum, energy, and products of nucleosynthesis are injected back into the pristine, chemically primitive environment (Karlsson et al., 2012). If we model the SN of a moderate mass Pop III star based on the typical Type II core collapse SN, we can use the usual parameters for explosion energy ($\sim 10^{51}$ erg) and metal yield ($\sim 1 M_{\odot}$). The α -element enhanced abundance patterns characteristic of core collapse SN yields are also consistent with currently available observational data for ancient, extremely metal-poor stars that could have formed directly from gas enriched by the first SNe (e.g., Tumlinson, 2006; Vangioni et al., 2011; Keller et al., 2014). The relic HII region can leave behind density perturbations that interact with the expanding SN blastwave and drive turbulence that aids in mixing with a potentially clumpy ionized medium (Whalen & Norman, 2008).

In chapter 2 we report results from a cosmological hydrodynamical simulation of the radiative and supernovae feedback by a single isolated Pop III star on the metal-free gas in its host dark matter mini halo. The transport of newly synthesized heavy elements was simulated, from the point of injection by the expanding supernova remnant, until an enriched cloud recondensed with the aid of metal-enhanced cooling. These numerical results allow us to constrain both the degree of metal-enrichment by a single SN and the physical timescale between the death of the first stars and the recollapse of enriched gas that could form the first metal-poor stars, specifically investigating the hypothesis that the first stars had moderate masses $\sim 10 M_{\odot}$. While we did not track the detailed chemical abundance patterns in this study, others have argued that the observed abundances in ancient, extremely metal-poor stars (e.g., Cayrel et al., 2004; Beers & Christlieb, 2005; Frebel et al., 2005; Lai et al., 2008) could be explained by moderate-mass Pop III SNe (e.g., Joggerst et al., 2010; Tumlinson, 2010). Our result broadly agrees with those interpretations of the cosmic abundance record, but require more detailed investigations into the possible sources of enrichment bias.

1.2 Hydrodynamical bias in metal enrichment

The spectroscopic abundance patterns in the atmospheres of ancient, extremely metal-poor stars contain signatures of their chemical enrichment history (for reviews, see Beers & Christlieb, 2005; Karlsson, Bromm & Bland-Hawthorn, 2013; Frebel & Norris, 2013a, 2015). Although the most metal-poor stars were likely enriched by only a few discrete progenitors, significant complexity remains forcing one to carefully interpret the observed abundance patterns in relation to theoretical models (Audouze & Silk, 1995; Shigeeyama & Tsujimoto, 1998). Star formation is inherently stochastic and the properties of individual progenitors (e.g. metallicity and individual abundances) may differ in significant ways from their averages. Turbulent hydrodynamics add additional complexity to the deposition of metals onto enriched clouds where incomplete mixing during the star formation process may confuse and obscure individual abundance signatures. This complexity is expected to persist even in the case of a single progenitor, due to the differentiation of elements within the ejecta of a SN remnant, and requires one to model the hydrodynamics as much as possible from first principles.

High-resolution (e.g., Wise & Abel, 2008a; Greif et al., 2010; Wise et al., 2012, 2014; Ritter et al., 2012; Jeon et al., 2014) and moderate-resolution (e.g., Ricotti, Gnedin & Shull, 2008; Bovill & Ricotti, 2009; Tassis, Gnedin & Kravtsov, 2012; Muratov et al., 2013; O’Shea et al., 2015) simulations of metal enrichment in early star systems are especially timely, but have so far only been concerned with the total amplitude of metal enrichment and have not investigated the implications of biased enrichment that could lead to specific abundance patterns that differ from the progenitor averages. Theoretical models of core collapse SN yields (e.g., Heger & Woosley, 2002, 2010, among others) have not yet converged, and worse, the true yields may not be deterministic and could be significantly influenced by local instabilities within the explosion and expanding remnant (e.g., Arnett & Meakin, 2011; Ellinger et al., 2012; Wongwathanarat, Janka & Müller, 2013; Smith et al., 2015a; Couch et al., 2015). If abundance patterns contributed by individual SN could be represented as monolithic basis vectors, powerful statistical tools (e.g. Principal Component Analysis Ting et al., 2012) exist to identify the different nucleosynthetic source classes, especially with the wealth of new spectroscopic survey data from large-scale surveys such as HERMES-GALAH (Zucker et al., 2012; De Silva et al., 2015) and GAIA-ESO (Gilmore et al., 2012). However, intrinsic explosion anisotropy could cause irreducible scatter in the abundances of enriched gas even for progenitors with the same

mass (Sluder et al., 2016), and the utility of these statistical tools may be diminished until the hydrodynamical enrichment biases are properly characterized.

In chapter 3 we attempt to identify these biases with a pair of high-resolution cosmological hydrodynamic simulations that quantify the heterogeneity in enriched gas, both by a single progenitor and a cluster of 7 SNe. Supernovae from both simulations explode into the same metal-free host dark matter halo assembled realistically from cosmological initial conditions, a plausible progenitor for the class of extremely low mass galaxies known as ultra-faint dwarfs (Ricotti, Gnedin & Shull, 2008; Salvadori & Ferrara, 2009). Individually tagged tracers are inserted that resolve the radial mass coordinates within the ejecta of the single progenitor, and the temporal order of consecutive explosions in the clustered case, in order to identify the pre-explosion sources of tracers that end up recollapsing in enriched clouds. Statistical analysis of the coarsely binned tracers from both cases place a lower limit on the heterogeneity of enriched gas that indicates that the source bins do not contribute equally, and that significant hydrodynamical bias does exist in the mapping of metal-poor abundances to their nucleosynthetic sources which could skew the abundance patterns towards certain elements and away from others.

1.3 Enriching the most ancient metal-poor stars

Connecting the abundance record preserved in the atmospheres of ancient, metal-poor stars to their formation sites at high redshifts is crucial for understanding the history of early star formation and metal enrichment (Frebel & Norris, 2015). If fine-structure line cooling by carbon and oxygen is the primary ingredient necessary to trigger low mass star formation, then we do not expect to detect ancient, metal-poor stars below a minimum critical metallicity, $Z_{\text{crit,fs}} = 10^{-3.5} Z_{\odot}$ (Bromm et al., 2001; Bromm & Loeb, 2003b; Santoro & Shull, 2006; Smith et al., 2009). This hypothesis is supported by the complete absence of observed stars with metallicities $Z \lesssim 10^{-5} Z_{\odot}$, below which we must invoke the theoretically uncertain processes of dust grain formation, though there are now a handful of ultra metal-poor candidates, such as SDSS J102915+172927 with $Z = 10^{4.35} Z_{\odot}$ (Caffau et al., 2011), that exist in the sub-critical regime and may require a hybrid explanation. The most extreme metal-poor stars could have been enriched by only a *single* Pop III SN. The complete lack of detectable iron in the atmosphere of SMSS J031300.36-670839.3 (Keller et al., 2014), for example, could be explained if it had been enriched by a single SN with a $\sim 60 M_{\odot}$ Pop

III progenitor (Ishigaki et al., 2014; Kobayashi et al., 2014; Takahashi, Umeda & Yoshida, 2014; Chen et al., 2016). On the other hand if Pop III SNe eject metals from their host dark matter halos efficiently enough to enrich nearby halos (Smith et al., 2015b), or if the timescale for the first SNe to enrich gas that forms new stars is sufficiently long, it may be likely that the typical second-generation star has been polluted by ejecta from multiple Pop III SNe. The transition from metal-free Pop III to metal-poor Pop II star formation is a crucial first step in the chemical evolution of all known galaxies, and the recycling of Pop III SNe ejecta into new stars is an active topic in numerical studies (e.g., Whalen et al., 2008a; Ritter et al., 2012, 2015; Cooke & Madau, 2014; Jeon et al., 2014; Sluder et al., 2016).

In chapter 4 we demonstrate one possible pathway toward the formation of the first metal-enriched stars in the aftermath of a single Pop III SN with an *ab initio* cosmological simulation that is designed to test the single progenitor enrichment hypothesis (Frebel & Bromm, 2012). The hydrodynamics of the SN explosion are followed until the first metal-enriched gas cloud undergoes gravitational collapse to high density, heralding the imminent formation of the first metal-enriched star. For the first time, this simulation answers the question of where in abundance space these new stars should exist in comparison to the spectroscopically observed metal-poor populations.

1.4 Supernova-driven outflows from the first galaxies

Galactic outflows play a vital role in the evolution of galaxies by regulating the gas reservoir available for star formation through the balance of cosmological gas accretion with the ejection of gas from a galaxy (Dekel & Silk, 1986), and it has long been theorized that SNe could be responsible for powering galactic winds (Chevalier & Clegg, 1985; McCray & Kafatos, 1987). There is strong observational evidence that the outflows, often multi-phase with cold dense clouds or warm ionized gas embedded within a tenuous hot wind, are ubiquitous around star-forming galaxies both in the nearby universe and at high redshift (Heckman, Armus & Miley, 1990; Heckman et al., 2000; Pettini et al., 2001; Martin, Kobulnicky & Heckman, 2002; Martin, 2005; Strickland & Heckman, 2009). The methods and assumptions used in semi-analytic models of hot galactic winds do not scale down to the very first galaxies, which were more compact, extremely metal poor, and likely did not form stars as efficiently (Filho et al., 2016). Likewise, most of the numerical simulations

SN-powered winds seek to reproduce observations of outflows from mature galaxies, such as starburst galaxy M82, by aggregating the effects of many SNe into an unresolved mass and energy injection region (Cooper et al., 2008; Sarkar et al., 2015; Schneider & Robertson, 2018), only briefly speculating about the role of winds in low mass galaxies where individual SNe could have a more significant impact. These medium resolution simulations presuppose the existence of an idealized clumpy or stratified galactic disk, where the embedded injection region is assumed to have already overtaken the central region, and a continuous star formation relation, e.g. Kennicutt (1998), has already been established to replenish outflowing mass and energy in the injection region at a constant rate. Early moderate-to-high resolution outflow simulations that explore the effects of individual SNe, such as Creasey, Theuns & Bower (2013); Scannapieco (2017); Kim, Ostriker & Raileanu (2017), initialize their remnants in an advanced stage where one must make assumptions about the thermalization efficiency and density structure of the remnant at a point when interaction with the surrounding medium may have already significantly modified the blast wave away from these assumptions. Because the first galaxies did not already exist in a self-regulated steady state, these same arguments can not be used to arrive at a self-consistent model for the driving of outflows from the first galaxies.

In chapter 5 we lay out a numerical framework for simulating the formation of a SN-powered outflow from a low mass galaxy while resolving both the SN remnants when they are inserted and the large-scale evolution of the combined superbubble (SB) from many overlapped SN remnants. The adaptive simulation mesh is zoomed in on individual SN blastwaves in the free expansion phase when their evolution is still well-described by simple analytical arguments, before interactions with the surrounding medium introduce additional hydrodynamical bias, and continue to follow them at high resolution until they have fully merged with the bubble. Thus we may simultaneously follow the evolution of the intergalactic medium between galaxies, the circumgalactic medium within the virial radius, the interstellar medium within a galactic disk, and the individual supernovae that shock gas, both heating and imparting the radial momentum necessary to potentially drive a galactic outflow.

Chapter Two: Confined Population III enrichment and the prospects for prompt second-generation star formation¹

The first stars forming from metal-free gas in the early universe, the Population III (Pop III), profoundly transformed their cosmic environment. Radiation from these stars first ionized the otherwise neutral, chemically pristine gas. In their final demise, likely involving supernovae or the collapse into a black hole, the Pop III stars injected momentum, energy, and nucleosynthetic products into the environment (Karlsson et al., 2012). The amplitude and character of these effects depended sensitively on the Pop III stellar masses, as well as on theoretically uncertain aspects of stellar evolution. Early numerical investigations of the formation of Pop III stars in metal-free cosmic halos concluded that the stars were isolated and rather massive, with masses $\gtrsim 100 M_{\odot}$ (Bromm, Coppi & Larson, 1999, 2002; Abel, Bryan & Norman, 2000, 2002; Gao et al., 2007; O’Shea & Norman, 2007). Recent numerical investigations, however, have shown that angular-momentum-aided fragmentation (Stacy, Greif & Bromm, 2010; Clark et al., 2011a; Greif et al., 2011, 2012) and radiative termination of accretion (Hosokawa et al., 2011; Stacy, Greif & Bromm, 2012a, see, also, McKee & Tan 2008 for an analytical approach) during protostellar accretion could limit the masses to as low as a few tens of solar masses. The final stellar mass range remains uncertain but could plausibly be $\sim 1 - 50 M_{\odot}$ with a characteristic mass $\sim 10 M_{\odot}$.

For a wide range of stellar masses and ambient gas densities, Pop III stars have sufficient luminosities and effective temperatures to form extended HII regions, unless they form in especially high mass halos (e.g., Whalen et al., 2008b) or with unusually high accretion rates during the protostellar phase (e.g., Hosokawa, Omukai & Yorke, 2012). The raised pressure of the interior ionized gas produces a hydrodynamic response that reduces the circumstellar gas density, and it is the density profile modified by HII region dynamics that the supernova blast wave expands into. The density structure imprinted by the HII region can interact with the blast wave to drive turbulence and compositional mixing of the supernova ejecta.

Because the stellar ionizing photon production rate is a strong function of stellar mass (e.g., Bromm et al., 2001; Schaerer, 2002), the properties of HII regions of the first stars

¹This chapter was published as Ritter J. S., Safranek-Shrader C., Gnat O., Milosavljević M., Bromm V., 2012, ApJ, 761, 56, under the supervision of Miloš Milosavljević.

will depend on the mass. A metal-free star with mass $> 100M_{\odot}$ could emit $> 10^{50}$ ionizing photons per second, which would ionize not only the parent cosmic minihalo, but a larger volume of the primordial intergalactic medium (IGM). The pressure of the photoionized gas drives a supersonic, radially propagating pressure wave, which ultimately shocks (Whalen, Abel & Norman, 2004; Whalen et al., 2008b; Kitayama et al., 2004; Alvarez, Bromm & Shapiro, 2006; Abel, Wise & Bryan, 2007; Yoshida et al., 2007). This expels a fraction of the baryons from the halo even before the supernova explodes. Only the densest clumps residing in the filaments streaming into the halo from the cosmic web are able to avoid ionization (Abel, Wise & Bryan, 2007). Furthermore, the HII regions may also be prone to violent dynamical instabilities that could create a clumpy medium (Whalen & Norman, 2008), with interesting consequences for supernova blast wave dynamics. Most of these features should carry over to lower mass Pop III stars with lower ionizing photon production rates, but the magnitude of the effects is weaker: the temperature of the photoionized gas (at a fixed distance from the star) is lower, the pressure wave is less pronounced, and the final ionized mass fraction inside the halo and the ionizing photon escape fraction from the halo are lower.

Similarly, the outcome of the stellar demise is expected to depend sensitively on stellar mass. Restricting to nonrotating, metal-free stars with minimum mass loss (e.g., Heger & Woosley, 2002; Heger et al., 2003), it is expected that the stars with masses $15 - 50M_{\odot}$ undergo core collapse, leaving behind a neutron star, or with fallback, a black hole. The stars with masses $50 - 140M_{\odot}$ can produce a black hole directly, though the stars above $100M_{\odot}$ may be affected by pair-pulsational instability. The stars with masses $140 - 260M_{\odot}$ explode as pair-instability supernovae (PISNe), and even more massive stars can also directly collapse into a black hole. Stellar rotation introduces new effects and significant theoretical uncertainties, e.g., the stars might first form a central black hole and the subsequent accretion of the rotating stellar envelope onto the black hole might power an outflow that could produce an explosion (see, e.g., MacFadyen & Woosley, 1999; MacFadyen, Woosley & Heger, 2001; Kohri, Narayan & Piran, 2005; Milosavljević et al., 2012; Lindner et al., 2012), with a peculiar nucleosynthetic imprint that can be sought in especially metal-poor stars (e.g., Iwamoto et al., 2005).

Much of the theoretical work on the formation of the first stars and galaxies (e.g., Wise, Turk & Abel, 2008; Wise et al., 2012; Greif et al., 2010), and on strategies for detecting metal-free stellar populations in the observations of galaxies and supernovae (e.g., Schaerer, 2003; Johnson et al., 2009; Raiter, Schaerer & Fosbury, 2010; Zackrisson et al.,

2011), has postulated the massive character of metal-free stars. The prospect of PISNe has been particularly interesting in view of the large expected explosion energy $\sim 10^{53}$ ergs and large nucleosynthetic yield, and many investigations have focused on this type of explosion (see, e.g., Pan, Kasen & Loeb, 2012; Hummel et al., 2012; Whalen et al., 2013). Such an explosion further reduces the residual baryonic content of the halo (Bromm & Loeb, 2003a) and the metals are dispersed far outside, thus enriching a relatively large region of the surrounding medium (e.g., Wise & Abel, 2008b; Greif et al., 2010; Maio et al., 2010; Wise et al., 2012). While this enrichment has only a minor effect on the ultimate metal budget of the IGM (Scannapieco, Ferrara & Madau, 2002; Yoshida, Bromm & Hernquist, 2004), it has the potential to raise the metallicity of larger collapsing halos above a “floor” (e.g., Bromm, Yoshida & Hernquist, 2003; Smith, Sigurdsson & Abel, 2008), itself a function of the dust content (e.g., Schneider et al., 2012), thought to be necessary for fragmentation into low-mass stars.

There has been much less work done on the cosmic imprint of Pop III stars with masses in the range tentatively favored by recent investigations (Stacy, Greif & Bromm, 2010, 2012a; Clark et al., 2011a; Greif et al., 2011; Hosokawa et al., 2011). The ionizing luminosities of these moderate-mass Pop III stars could be up to an order of magnitude lower than those of their massive counterparts, the supernova energies could be $\sim 10^{51}$ ergs, the nucleosynthetic yields could be at most a few solar masses per supernova, and the characteristic abundance patterns could be more consistent with currently available observational data (e.g., Tumlinson, 2006; Vangioni et al., 2011). Thus the evolution of minihalos forming only moderate mass Pop III stars should differ in critical ways from that of objects forming very massive ones.

Here we report the first results from a program to study the detailed transport of the nucleo-synthetic output of the first stars, from the point of injection in supernovae, until at least a fraction of the new metals have recondensed in descendant cosmic halos where they may contribute to the formation of second-generation, metal-enriched stars. The specific aim of the chapter is to investigate the implications of the hypothesis that the first stars had moderate masses—masses that are insufficient to produce extraordinarily extended HII regions and ultra-energetic supernovae. We present a cosmological simulation tracking the supernova ejecta of one such intermediate-mass Pop III star. It is expected on theoretical grounds that the character of the new star formation in the descendant halo will depend on the rate of gas inflow \dot{M}_{inf} into the nucleus of the halo, where the gas can rapidly cool and fragment into stars. Also, the cooling rate of the gas and the compressibility of the

turbulence in the flow depend on the average metallicity Z_{inf} and the degree of metallicity homogeneity in the gas. The simulation allows us to measure these parameters and thus shed light on the conditions for the formation of metal-enriched stars in the aftermath of a Pop III supernova.

Our focus is the gross dynamics of the supernova remnant, and to trace the dispersal of the metals produced. We here do not attempt to make detailed predictions for chemical abundance patterns in second-generation stars that may in part survive to the present day, and that can be compared with the extensive data on metal-poor stars in the Milky Way (e.g., Cayrel et al., 2004; Beers & Christlieb, 2005; Frebel et al., 2005; Lai et al., 2008). It has been argued that the observed abundances in these ancient stars can be explained with Pop III supernovae from moderate-mass ($\sim 15 - 40 M_{\odot}$) progenitors (e.g., Joggerst et al., 2010; Tumlinson, 2010). This interpretation resonates with the basic assumption on the Pop III mass-scale made here. In view of possibly strong selection effects in the existent metal-poor abundance data, it is important, however, to keep an open mind in this regard. One key selection bias might result from the high level of enrichment in the immediate neighborhood of a PISN (Wise & Abel, 2008b; Greif et al., 2010), such that second-generation stars could already exhibit overall metallicities of $10^{-3} - 10^{-2} Z_{\odot}$; most surveys targeting the extremely metal-poor tail would then miss such PISN-enriched fossils (Karlsson, Johnson & Bromm, 2008). Future surveys, such as *Gaia*, should provide us with essentially unbiased samples and an opportunity to constrain theoretical models.

The chapter is organized as follows. In Section 2.1, we describe our numerical algorithm. In Section 2.2, we present our results. In Section 2.3, we discuss implications for the formation of metal-enriched star clusters in the early universe, and in Section 2.4, we present our main conclusions. We adopt the cosmological parameters consistent with the *Wilkinson Microwave Anisotropy Probe* seven-year data (Komatsu et al., 2011). We explicitly indicate whether comoving or physical length units are utilized; all other quantities, such as density, are expressed in physical units.

2.1 Simulating a Supernova in a Minihalo

2.1.1 Cosmological Initial Conditions and Gravity

We initialize our simulation in a periodic cosmological box of volume 1 Mpc^3 (comoving) at redshift $z = 146$, large enough not only to permit the formation of such a star, but

also to allow the subsequent growth of the star’s host halo, by accretion and merging, into a larger object that is the potential site of second-generation star formation. The initial conditions are generated with the multiscale cosmological initial conditions package GRAPHIC2 (Bertschinger, 2001) with two levels of nested refinement on top of the 128^3 base grid. The highest refined region had an effective resolution of 512^3 , corresponding to a dark matter particle mass of $230 M_\odot$. While we will focus on the dynamics of an initially $\sim 10^6 M_\odot$ minihalo at redshift $z \sim 20$, the region of high refinement was centered on the overdensity that first collapses to form a more massive $\sim 10^8 M_\odot$ halo at a lower redshift. The time integration was carried out with the multipurpose astrophysical adaptive mesh refinement (AMR) code FLASH (Fryxell et al., 2000), version 3.3, employing the direct multigrid Poisson gravity solver of Ricker (2008). The AMR refinement criteria, which we describe in Section 2.1.3 below, are set to ensure that relevant baryonic processes are sufficiently well resolved in the simulation. In collapsing regions where baryons dominate the gravitational potential, the AMR resolution length quickly becomes smaller than the dark matter particle separation. There, we employ a mass- and momentum-conserving quadratic-kernel-based softening procedure developed in Safranek-Shrader et al. (2012) which is applied to the dark matter density variable during mapping onto the computational mesh, to render the dark matter particle contribution to the gravitational potential smooth on the scale of the local AMR grid.

2.1.2 Chemistry and Cooling

Prior to the initialization of the HII region, we integrate the full nonequilibrium chemical network for hydrogen, helium, deuterium, and their chemical derivatives. The chemical and radiative cooling updates, which include, among other processes, the cooling or heating by the cosmic microwave background (CMB), are operator-split from the hydrodynamic update and are subcycled within each cell. The chemical reaction rates are the same as we have summarized in Safranek-Shrader, Bromm & Milosavljević (2010), except that the chemical and radiative cooling update is isochoric in the present simulation. The network is integrated with the Bulirsch-Stoer-type semi-implicit extrapolation method of Bader & Deuffhard (1983). We test the thermodynamic evolution of the gas in Safranek-Shrader et al. (2012).

After turning on the ionizing source, which we describe in Section 2.1.4 below, we continue to integrate the nonequilibrium chemical network in the neutral gas, but in the ion-

ized gas, we adopt a scheme in which the gas temperature and chemical abundances relax exponentially toward a target photoionization equilibrium. The equilibrium gas temperature and chemical abundances are functions of the photoionization parameter $\xi \equiv 4\pi F/n_{\text{H}}$ only, where F is the radiative energy flux and n_{H} is the number density of hydrogen nuclei, and are precomputed with the same chemical network that we integrate in the neutral gas. The relaxation time scale is chosen to be the true, nonequilibrium thermal time scale $t_{\text{therm}} \equiv (d\ln T/dt)^{-1}$, defined by the instantaneous local radiative cooling and photoionization heating rates.

After inserting the supernova remnant, the gas can contain an arbitrary admixture of metals in addition to the primordial elements. The radiative point source is removed, thus discontinuing the photoionization equilibrium calculation. We revert to an integration of the nonequilibrium chemical network for the primordial species and calculate the ionization state of the metals and their contribution to the cooling by interpolation from precomputed tables. At temperatures above 8000 K, the collisional ionization equilibrium state of each of the metal species, including C, N, O, Ne, Mg, Si, S, and Fe, is calculated separately using methods described in Gnat & Sternberg (2007) and Gnat & Ferland (2012). Below 8000 K but above 200 K, we ignore the metallic contribution to the free electron abundance and tabulate a single density-independent cooling function (such that the volumetric radiative loss rate scales with the square of the density), appropriate for a gas at relatively low densities $\lesssim 10^3 \text{ cm}^{-3}$, using the code CLOUDY (Ferland et al., 1998). The tabulated data extend to a minimum metallicity of $10^{-3} Z_{\odot}$; below this metallicity, we set the metal cooling rate in this range of temperatures to zero. Below 200 K, we disable cooling by metal lines altogether; however, because low-temperature thermodynamics is not the focus of this work, this has no effect on the forthcoming results. The treatment of primordial species takes into account the electrons provided by the metals and vice versa, but we do not include collisional charge exchange reactions between the primordial species and the metal species. We assume that the metals have solar abundance ratios. This is an arbitrary, unnatural choice given that our metals are being produced by a core-collapse supernova, but this choice should have only a very minor effect on the thermodynamic evolution of the supernova remnant.

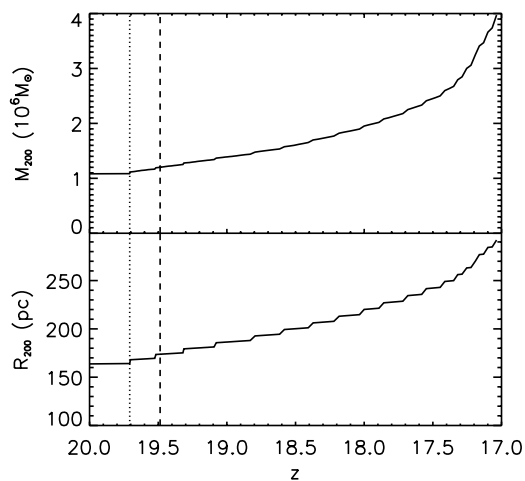


Figure 2.1: The halo mass M_{200} and radius R_{200} as a function of redshift, over the course of 50Myr. The dotted line marks the formation of the star, and dashed line the supernova explosion. The steps are an artifact of the method we use to estimate R_{200} .

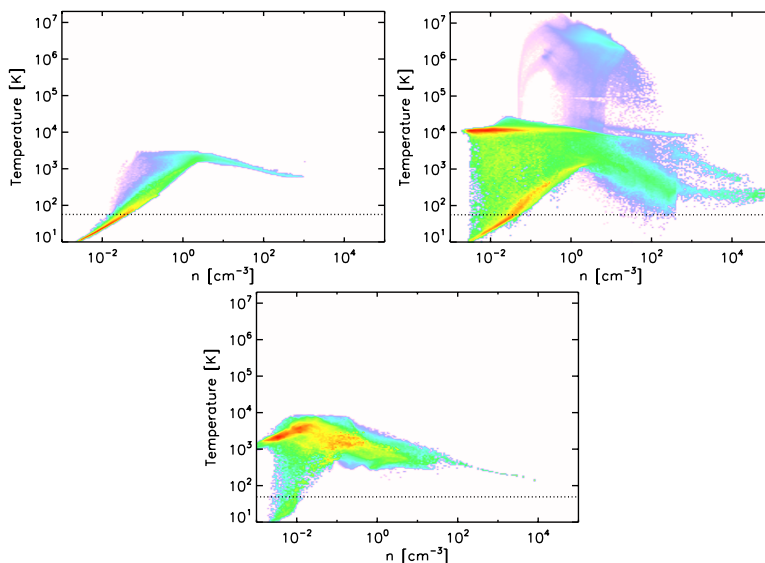


Figure 2.2: Density-temperature phase plot for the gas within 1 kpc (physical) from the center of the minihalo at redshifts, from left to right, $z = 19.7$ (right before the insertion of the star), $z = 19.5$ (in the Sedov-Taylor phase of the supernova, 8kyr after the explosion), and at $z = 17$ (end of the simulation, 40Myr after the explosion). By the end of the simulation, the gas heated by photoionization and the supernova has cooled and the halo has resumed central gravitational collapse, albeit at four times higher halo mass and now a nonzero metallicity. The dashed line shows the CMB temperature.

2.1.3 Adaptive Mesh Refinement Strategies

The simulation is set to adjust the FLASH refinement level ℓ based on the local baryon density ρ_b to ensure that denser regions are more highly refined. The grid separation (cell size) is related to the refinement level via $\Delta x = 2^{-\ell+1-3}L$, where L is the size of the computational box.² As gravitational collapse drives the local fluid density ρ_b to increasingly higher values, the local refinement level is adjusted to satisfy $\rho_b < 3\bar{\rho}_b 2^{3(1+\phi)(\ell-\ell_{base})}$ at all times, where $\ell_{base} = 5$ is the refinement level corresponding to the base grid of size $128 = 2^{\ell_{base}+2}$, we choose the scaling parameter to equal $\phi = -0.3$ (value consistent with Safranek-Shrader et al. 2012). We insert a star particle when the hydrogen number density first exceeds 1000cm^{-3} ; this happens at redshift $z \approx 19.7$ and refinement level $\ell = 14$, corresponding to cell size $\Delta x \approx 0.74\text{pc}$ (physical).

At the end of the star’s life and just prior to inserting the young supernova remnant, we force the simulation to refine further to level $\ell = 21$ at the location of the star particle, corresponding to cell size $\Delta x \approx 0.006\text{pc}$ (physical). This allows us to insert the supernova remnant well within the free-expansion phase, before the ejecta have started to interact with the circumstellar environment. Then, we disable automatic derefinement, and allow the simulation to refine additional computational cells, up to the maximum level ℓ_{max} initially equal to 21, based on the standard second derivative test in FLASH, but in this case, the second derivative test is computed using the cell metallicity. This ensures that the entire region enriched with metals will be resolved at the refinement level ℓ_{max} . As the supernova remnant expands, we gradually and cautiously lower ℓ_{max} , and thus coarsen the resolution of the metal-enriched region, to allow us to use ever longer time steps and integrate the simulation for 40Myr past the insertion of the supernova.

2.1.4 The First Star and Ionizing Radiation Transfer

When the hydrogen number density first exceeds 1000cm^{-3} near the center of the collapsing minihalo, we insert a collisionless star particle.³ The star is free to move in the combined gravitational potential of the dark matter and baryons but does not contribute to the potential, i.e., it is treated as massless. We calculate the transfer of the star’s ion-

²The factor of 2^{-3} arises from the subdivision in FLASH of each computational block relative to which the refinement level is defined into 8^3 cells.

³This threshold density for star formation is ad hoc, but consistent with the choice in, e.g., Wise et al. (2012).

izing radiation and the response of the circumstellar medium to the associated photoheating in the HII region as follows. We assume that it is an isotropic source of hydrogen-ionizing radiation and treat the radiation as monochromatic with photon energy $h\nu = 16\text{ eV}$ and photon emission rate $Q(\text{H}) = 6 \times 10^{49}\text{ photons s}^{-1}$. This ionizing photon rate is about three times as high as has been estimated for a $40M_{\odot}$ metal-free star without mass loss, $Q(\text{H}, 40M_{\odot}) \approx 2 \times 10^{49}\text{ photons s}^{-1}$ (Schaerer, 2002). We deliberately overestimate the ionizing luminosity to allow for the presence of additional, lower-mass, longer-lived stars also producing additional ionizing photons in a compact cluster around the primary $40M_{\odot}$ star. Also, boosting the ionizing luminosity allows the HII region to break out more easily at the moderate spatial resolution at which we insert the star particle and perform ionizing radiation transfer.

Our intention was to calibrate the monochromatic ionizing photon energy to a $40M_{\odot}$ star, but the prescription we used to arrive at the adopted value of 16 eV suffers from lack of physical consistency. In retrospect, the inconsistency could have been avoided by carrying out photon-number-flux-weighted averaging of photoionization cross sections and heating rates as in, e.g., Appendices A.2 and A.3 of Pawlik, Milosavljević & Bromm (2013a), assuming a spectral energy distribution containing a single $40M_{\odot}$ Pop III star with an effective temperature $\sim 8 \times 10^4\text{ K}$ (Schaerer, 2002), as well as perhaps several lower-mass companion Pop III stars with lower effective temperatures. This would have resulted in higher average photoelectron energies than in our monochromatic treatment. The unintended consequence of our crude prescription is that in the simulation, photoionization will heat the gas only to a maximum temperature $\sim 14,000\text{ K}$, whereas for an effective photospheric temperature of, e.g., $\sim 10^5\text{ K}$ (similar in moderate mass and very massive metal free stars), the gas at small distances $\lesssim 1 - 10\text{ pc}$ from the star should be heated to higher temperatures $\sim 30,000\text{ K}$, especially as the ionized gas density drops (see, e.g., Yoshida et al., 2007). An artifact of this is a potential underestimate of the amplitude of the outward-propagating pressure wave resulting from the intense photoionization heating in the HII. We address this issue further in Section 2.2.1 below.

To carry out ionizing radiation transfer, we center a spherical coordinate system on the current position of the star particle, and pixelize the angular coordinate using the HEALPix scheme of Górski et al. (2005) with $N_{\text{pix}} = 3072$ pixels. Within each angular pixel, we split the radial coordinate in the range $4 \times 10^{20}\text{ cm} \leq r < 10^{24}\text{ cm}$ (comoving), corresponding to $0.7\text{ pc} \lesssim r < 17\text{ kpc}$ (physical), into $N_{\text{rad}} = 103$ logarithmic radial bins. For each volume element $E_{p,b}$ defined by an angular HEALPix pixel p and a radial bin b , and for each mesh

cell E_c defined by the cell index c , we compute the volume of the intersection of the two elements $V_{p,b;c} \equiv \text{vol}(E_{p,b} \cap E_c) \geq 0$. In general, only a fraction of the cell lies within $E_{p,b}$. In this case, we recursively split the cell into sub-cells via an octree subdivision procedure and compute the contribution of the subcells lying within $E_{p,b}$ to the intersection volume; the recursion is continued until a desired accuracy is achieved. Armed with the intersection volumes, we compute the average case- B hydrogen recombination rate $\dot{n}_{\text{rec},p,b}$ evaluated under the assumption of full ionization (as in the standard Strömgen calculation) within each $E_{p,b}$ via

$$\dot{n}_{\text{rec},p,b} = \frac{1}{V_{p,b}} \sum_c \alpha_{\text{rec},B}(T_c) n_c^2 V_{p,b;c}, \quad (2.1)$$

where $V_{p,b} = \text{vol}(E_{p,b}) \approx \sum_c V_{p,b;c}$. In Equation (2.1), T_c and n_c , are, respectively the temperature and density of hydrogen nuclei within the cell, and $\alpha_{\text{rec},B}(T)$ is the hydrogen recombination coefficient. Within each bin, we compute the approximate integral of $4\pi r^2 \dot{n}_{\text{rec},p}(r)$ along the radial direction (now replacing the bin index b with the continuous radial coordinate r) and determine the pixel-specific Strömgen radius $R_{S,p}$ that solves the equation

$$Q(\text{H}) = \int_0^{R_{S,p}} 4\pi r^2 \dot{n}_{\text{rec},p}(r) dr. \quad (2.2)$$

We assume that no ionizing radiation penetrates to radii $r \geq R_{S,p}$. At smaller radii, we compute the local ionizing photon number flux (in the units of photons $\text{cm}^{-2} \text{s}^{-1}$) using

$$f_r(r) = \frac{1}{4\pi r^2} \left[Q(\text{H}) - \int_0^r 4\pi r'^2 \dot{n}_{\text{rec},p}(r') dr' \right]. \quad (2.3)$$

The local ionizing flux is then used to compute the local photoionization parameter for cell c lying within the pixel p with a center at a radius r_c via $\xi_p(r) = 4\pi h\nu f_p(r_c)/n_c$. Given a value of the photoionization parameter, the photoionization equilibrium temperature of the gas and the chemical abundances within the cell are evaluated via table lookup (see Section 2.1.2). The computation is fully parallel and is repeated at every hydrodynamic time step. We do not compute the radiation pressure from Thomson scattering and photoionizations. This radiative transfer scheme is not explicitly photon conserving and is not designed to correctly reproduce the ionization front kinematic especially when an R-type ionization front is expected, but it is sufficient to reproduce the basic hydrodynamic response of the gas to photoionization heating.

2.1.5 Supernova and Metal Transport

We insert the supernova 3 Myr after inserting the star. The supernova is initialized in the free-expansion phase, when the remnant is about $t - t_{\text{SN}} = 35$ yr old, well before the freely expanding ejecta have started to interact with the primordial circumstellar medium. This early insertion is possible thanks to our ability to drastically increase the local mesh resolution at a specific time in the simulation—just prior to supernova explosion—and then gradually degrade the resolution as the remnant expands. The ejecta are initially cold and have a total mass $M_{\text{SN}} = 40M_{\odot}$ and a total kinetic energy of $E_{\text{SN}} = 10^{51}$ ergs. The metal yield is assumed to be $Z_{\text{SN}} = 0.1$ and uniformly premixed in the ejecta, implying $4M_{\odot}$ of metals. The velocity of the ejecta is linear in the distance from the center of the explosion and the density is uniform. The initial radius of the remnant is chosen such that its radius is 10% of the radius of the remnant at which the swept up mass equals the ejecta mass, or in this case, $R_{\text{SN}} = 0.075$ pc. The simulation carries out advection of the absolute metallicity Z by treating it as a passive mass scalar quantity. This advection is subject to undesirable numerical diffusion, which is unavoidable in Eulerian solvers of this type (see, e.g., Plewa & Müller, 1999). Therefore, in parallel with passive scalar advection, we also insert a number $N_{\text{part}} = 5 \times 10^5$ of passive Lagrangian tracer particles, originally uniformly distributed in the ejecta. The simulation advances particle positions by integrating the first-order ordinary differential equation $d\mathbf{X}_i/dt = \mathbf{v}(\mathbf{X}_i)$, where \mathbf{X}_i is the location of particle i , and $\mathbf{v}(\mathbf{X}_i)$ is the baryon fluid velocity, quadratically interpolated from the computational grid, at the location of the particle. We do not take into account the possibility that the supernova may be a source of molecules and dust. Both are undoubtedly produced in the free-expansion phase, but their survival of the reverse shock hinges on small-scale clumpiness of the ejecta and on other complex, incompletely-understood physics (see, e.g., Cherchneff & Dwek, 2009, 2010).

2.2 Results

In Figure 2.1, we show the redshift evolution of the radius R_{200} within which the average halo density equals 200 times the critical density, as well as the corresponding enclosed halo mass M_{200} . The star particle is inserted at $z \approx 19.7$ and the supernova at $z \approx 19.5$. The halo radius doubles from $R_{200} \approx 160$ pc to 300 pc in the course of the simulation, and the halo mass quadruples from $M_{200} \approx 10^6 M_{\odot}$ at star insertion to $4 \times 10^6 M_{\odot}$ at the end

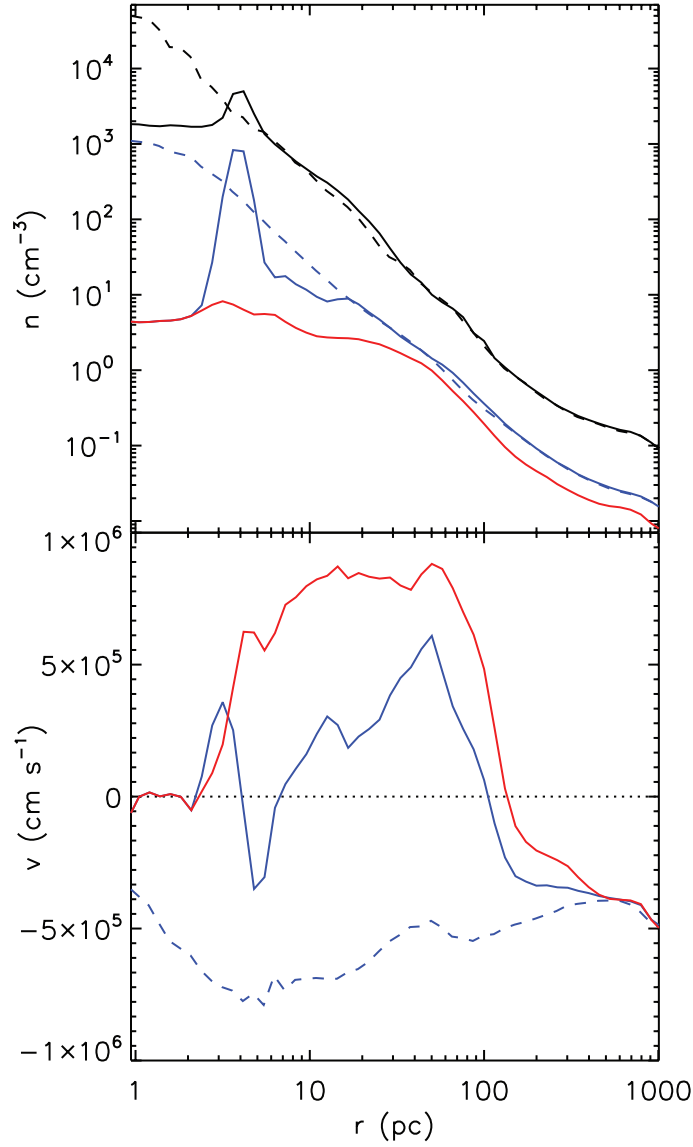


Figure 2.3: Spherically averaged density (upper panel) and radial velocity (lower panel) profiles for all baryons (blue line) and the ionized gas (red line), before the insertion of the star at $z = 19.7$ (dashed lines), and before the insertion of the supernova at $z = 19.5$ (solid lines). For reference, we also show the density profile of gravitational mass density (including dark matter) in the units of the proton mass (black line). The neutral gas density peak located inside the HII region is a clump of dense neutral gas that has withstood photoionization. The gas with positive (negative) radial velocity is flowing away from (toward) the star.

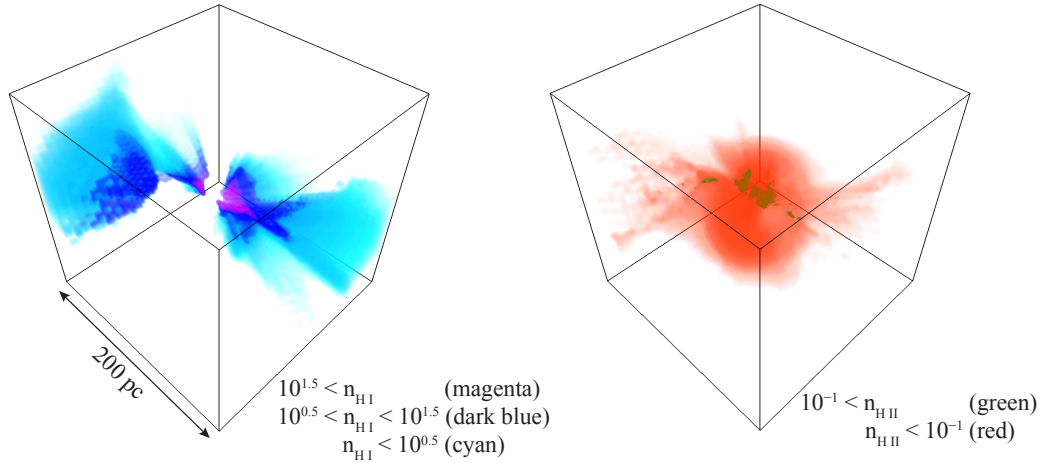


Figure 2.4: Volume rendering of the number density of neutral (left panel) and ionized (right panel) hydrogen at $z = 19.5$, right before the insertion of the supernova, in a 200 pc cube centered on the star particle. The colors show gas density ranges (in units of cm^{-3}) as indicated in the legend. The densest ionized gas clumps $n_{\text{HII}} > 10^{-1} \text{cm}^{-3}$ in the center of the cube seem to be fed by photo-ablation from even denser, $n_{\text{HI}} > 10^{1.5} \text{cm}^{-3}$, persistent cold neutral clumps in this region.

of the simulation. Figure 2.2 shows the density-temperature phase diagram for gas within 1 kpc (physical) from the center of the halo, immediately prior to the formation of the star particle, after the supernova explosion, and finally at the end of the simulation when the halo mass has quadrupled. Before stellar insertion, the thermodynamic structure of the halo is that of an archetypical minihalo in which gas cools by rovibrational transitions of molecular hydrogen. The thermodynamic structure at the end of the simulation is similar, which illustrates that the halo relatively quickly “recovers” from the radiative and kinetic impact of the first star and resumes central gravitational collapse. Photoionization and the supernova blast wave, which we discuss in detail in Sections 2.2.1 and 2.2.2, respectively, only temporarily disrupt the cooling and condensation of gas in the halo center. Then, in Section 2.2.3, we study the transport of the metals injected by the explosion.

2.2.1 The HII Region

The photoionization raises the temperature of the interior of the HII region to $\approx 10^4$ K with a maximum temperature $\approx 1.4 \times 10^4$ K; the latter temperature ceiling is an artifact of our photoionization prescription (see Section 2.1.4). The increase in gas pressure drives an

outflow in the ionized gas, thus lowering the central density. In Figure 2.3, we show the star-centered, spherically-averaged gas density and spherically-averaged, mass-weighted radial velocity profile just before inserting the star, and 3 Myr later, just prior to inserting the supernova. During this interval, the spatial resolution in the vicinity of the star is $\Delta x \approx 0.75$ pc. We separately examine the density and velocity profiles of all gas and of the ionized gas only. The ionized gas has a maximum outward velocity of $\sim 9 \text{ km s}^{-1}$, which can be compared to the maximum gas inflow velocity $\sim -7 \text{ km s}^{-1}$ before photoionization. The central density drops from $\sim 2000 \text{ cm}^{-3}$ to $\sim 4 \text{ cm}^{-3}$. Interestingly, at radii as small as 2–3 pc, the densest gas clumps ($n \sim 10 - 1000 \text{ cm}^{-3}$) resist photoionization and do not acquire the outward velocity of the ionized gas.

An examination of the three-dimensional geometry of the ionized and neutral phases in Figure 2.4 shows that the sustained neutral (i.e., self-shielding) clumps are associated with the photo-ablated terminus of dense gas filaments feeding into the halo from the cosmic web. This outcome was already observed by Abel, Wise & Bryan (2007) in a similar simulation of a primordial HII region with more accurate radiation transfer. It is worth stressing that our simulation may not properly resolve the process of the ionization of dense cloud cores because the method is not explicitly photon conserving, and because it may not resolve the shock that is expected to precede the D-type ionization front in the cold gas (we find that the ionized gas near the D-type front is slightly over-pressured relative to the cold gas). For these reasons, we are not certain that the simulation has converged in terms of the rate of photo-ablation of dense neutral clumps, but qualitative consistency with previous work is reassuring. Continuous photo-ablation presents a source of fresh, dense ionized gas in the vicinity of the star. This, in addition to the temperature ceiling mentioned above, explains why the central ionized gas density in our simulation remains higher than the value $\sim 0.1 \text{ cm}^{-3}$ characteristically observed in one dimensional models.

We do not observe a clear indication of the expected outward propagating pressure wave and the associated shock wave, which would have manifested as a dense, supersonically propagating shell. Such a shell could become important at later times as it would modify the dynamics of the supernova blast wave; e.g., it could drive a reverse shock into the supernova ejecta which could trigger hydrodynamical instability and mixing of the ejecta with the swept up circumstellar medium (Whalen et al., 2008b). The absence of the pressure wave can be attributed to our approximate treatment of ionizing radiation transfer where the ionization front speed is not properly constrained by the finite ionizing photon consumption rate and is resolution dependent, and also because of the artificial tempera-

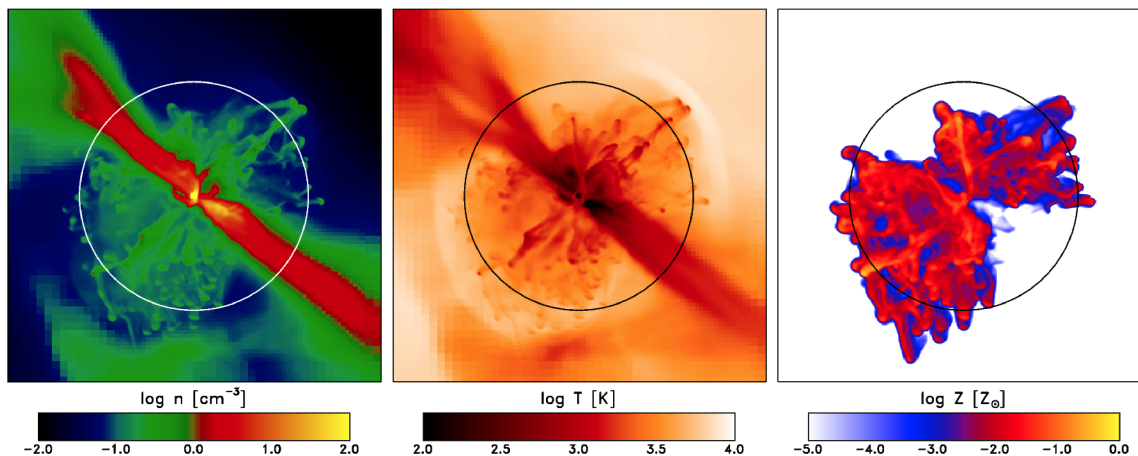


Figure 2.5: Baryon mass-weighted projection of hydrogen density, temperature, and fluid-based metallicity in units of the solar metallicity 8.5 Myr after the explosion. The circle shows the virial radius of the halo, which is here 180 pc (physical).

ture ceiling. However the ionized gas does acquire a positive radial velocity out to radii ~ 120 pc, consistent with expectations for our adopted source luminosity.

2.2.2 blast wave Evolution and Fallback

Because of the low energy and compactness of the remnant, the cooling by inverse Compton scattering off the CMB is relatively unimportant, different from the case of ultra-energetic Pop III supernovae, where this cooling channel dominates the early evolution (Bromm & Loeb, 2003a). The blast wave also largely avoids the dense neutral clumps resisting photoionization, and they remain a repository of low-entropy gas in the halo. This is easily seen in Figure 2.5, which shows mass-weighted projected density, temperature, and metallicity 8.5 Myr after the explosion. Outside of the filaments, after 40 Myr, the effects of photoionization and the blast wave have largely been erased; the thermal phase structure within the halo is similar to that of a higher-mass unperturbed minihalo. The appearance of warmer ($\lesssim 10^4$ K) gas at low densities reflects the higher virial mass of the halo at the end of the simulation and the residual entropy left by the fossil HII region. The presence of metals at local metallicities $Z \gtrsim 10^{-5} \sim 10^{-3} Z_{\odot}$ and an enhanced abundance of hydrogen-deuteride now facilitate more rapid cooling toward low temperatures. The enhanced cooling is now especially apparent at high densities $n_{\text{H}} \gtrsim 100 \text{ cm}^{-3}$ that are found in the central region. The dense gas is insufficiently well resolved at the end of the simulation;

the resolution limit hinders compression of the fluid to densities $n_{\text{H}} \gtrsim 1000 \text{cm}^{-3}$. Nevertheless, it is clear that the dense gas resides at temperatures a factor of a few lower than the gas at the same densities prior to the insertion of the ionizing source. We do not observe the anticipated gas cooling to the CMB temperature, either through metal line cooling or the cooling by hydrogen-deuteride (e.g., Johnson & Bromm, 2006), because we enforced an artificial temperature floor at 200 K.⁴

An insight into the rate of recovery of the halo can be obtained from Figure 2.6, which shows the Lagrangian radii that track the radial location of a grid of mass coordinates of the spherically averaged baryon and supernova ejecta mass as a function of time from the explosion. In this period, we gradually coarsen the spatial resolution from $\Delta x \approx 0.006 \text{pc}$, a high value achieved by telescopic adaptive mesh refinement at the location of the explosion, to $\Delta x \approx 14 \text{pc}$ at the end of the simulation, 40 Myr later. It is worth keeping in mind that the underlying flow is complex and contains simultaneous inflows and outflows that are averaged over; each of the radii reflects only the net displacement of the mass coordinate. The baryonic Lagrangian radii show expansion, driven by the supernova blast wave, starting at $\approx 20 \text{kyr}$ at the innermost radius shown, and appearing at progressively larger mass coordinates until outward-directed motion becomes evident near the virial radius at $\approx 2 \text{Myr}$ after the explosion. Each of the radii corresponding to mass coordinates inside the halo, however, shows a reversal from a net outflow to a net inflow. The reversal commences at $\approx 400 \text{kyr}$ at the innermost radius shown, and reaches progressively larger radii until $\approx 20 \text{Myr}$ when the flow at the virial radius turns into an inflow. Outside of the virial radius, cosmic infall persists largely unabated throughout the remnant’s history.

An examination of the evolution of the actual three-dimensional structure of the baryonic flow (see the projection in Figure 2.5) reveals that the prompt reversal can only in part be attributed to a fallback of the mass that the blast wave has swept up and to which it has transferred momentum. Instead, the filamentary inflow of dense, cold, molecular gas from the nearby cosmic web directly into the center of the minihalo contributes a large fraction of the mass inflow rate. The baryonic filaments are seen diagonally from top left to bottom right in Figure 2.7, which shows a slice of the density field. Because the filaments survive photoionization and the explosion largely intact, they can sustain a net inflow into

⁴The CMB temperature would have been a more natural choice for the temperature floor, but at densities at which radiative cooling below our assumed temperature floor would occur, the simulation would not be resolving the local Jeans length and would thus in any case not be able to accurately reproduce fragmentation in the gas. Thus, we defer a study of the fragmentation to a follow-up simulation.

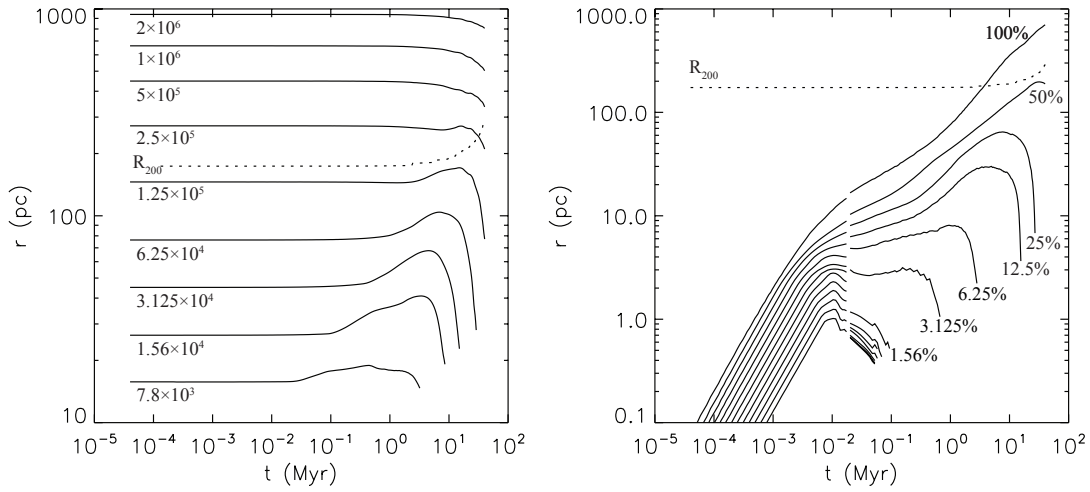


Figure 2.6: Characteristic radii corresponding to Lagrangian mass coordinates enclosing baryonic masses of, from top to bottom, $(2, 1.0, 0.5, \dots) \times 10^6 M_\odot$ (left panel; the masses are labeled on the curves in the units of M_\odot) and ejecta mass fractions, as tracked by passive tracer particles, of $(100\%, 50\%, 25\%, \dots)$ (right panel; percentages are labeled on the curves), both as a function of time since the explosion. The dotted line shows the virial radius R_{200} of the host halo. The baryonic radii are computed from the gravitational potential minimum of the halo. Supernova-driven expansion is evident in the mass coordinates inside the virial radius, but all mass coordinates return to infall owing in part to a persistent filamentary streaming of fresh, cold baryons from the cosmic web into the halo center. For ejecta radii, at times $t < 0.02 \text{ Myr}$, the location of the progenitor star is taken as the coordinate origin; at later times, the origin is the location of the gravitational potential minimum; the change of origin is visible as a discontinuity in the curves. By the end of the simulation, a half of the ejecta has turned around and is falling back toward the center of the halo. At late times, the curves plunge steeply as the material approaches the central unresolved fluid elements with a finite free-fall velocity.

the center of the halo even when a majority of the ejecta and the swept up mass are moving outward.

The Lagrangian radii for the supernova ejecta in Figure 2.6, right panel, show first signs of interaction of the ejecta with the circumstellar medium around 1 – 10 kyr after the explosion. What follows is a similar picture of expansion eventually reversing into fallback. Fractions of (3.125%, 6.25%, 12.5%, 25%, 50%) of the ejecta mass turn around and start falling back at around (0.2, 1.0, 4.0, 8.0, 30.0) Myr after the explosion. The corresponding turnaround radii are (3, 8, 30, 60, 200) pc. The outer $\sim 50\%$ of the ejecta passes the virial radius and continues to travel outward until the end of the simulation. The net outflow of ejecta at $r \gtrsim R_{200}$ can be contrasted with the net inflow of baryons at the same radii, underscoring the three-dimensional nature of the flow and an inadequacy of one-dimensional integrations in treating the long-term dynamics of supernova remnants in cosmic mini-halos. Spherical symmetry implicit in one-dimensional integrations forces the ejecta and the swept up circumstellar medium into a spherical thin shell at late times. It does not allow for the presence of the dense, low-entropy clouds that enter the halo by infall from the filaments of the cosmic web. The expanding shell may pass and leave behind such clouds. The spherical symmetry also does not allow radial segregation of the ejecta as a result of the instability of the decelerating thin shell.

Rayleigh-Taylor fingering is evident in Figure 2.5 at 8.5 Myr after the explosion. The long term evolution of the fragmented shell is seen in Figure 2.7, left panel, which shows the ejecta tracer particles in projection, superimposed on a slice of the density field through the center of the halo. It is also clear in these figures that the blast wave has expanded biconically perpendicular to the sheet-like baryonic overdensity deriving from the cosmic web; this pristine gas, unpolluted by the ejecta, is still able to stream into the halo center. In the right panel of Figure 2.7, showing the central 360 pc, pristine baryonic streams arrive diagonally into the central few tens of parsecs, where they form a two-armed spiral and join a self-gravitating central core. At this point in the simulation, the spatial resolution is insufficient to resolve the internal structure of the core.

Strikingly, we observe filamentary accretion of ejecta-enriched gas perpendicular to the pristine sheet. This is the return of the ejecta from the supernova remnant back into the center of the halo. A closer examination of the time evolution of the ejecta kinematics shows that in the snowplow phase, the ejecta are compressed into a thin shell, as expected. The thickness of the shell is itself not well resolved, thus we are not in the position to explore its susceptibility to direct gravitational fragmentation (e.g., Mackey, Bromm & Hern-

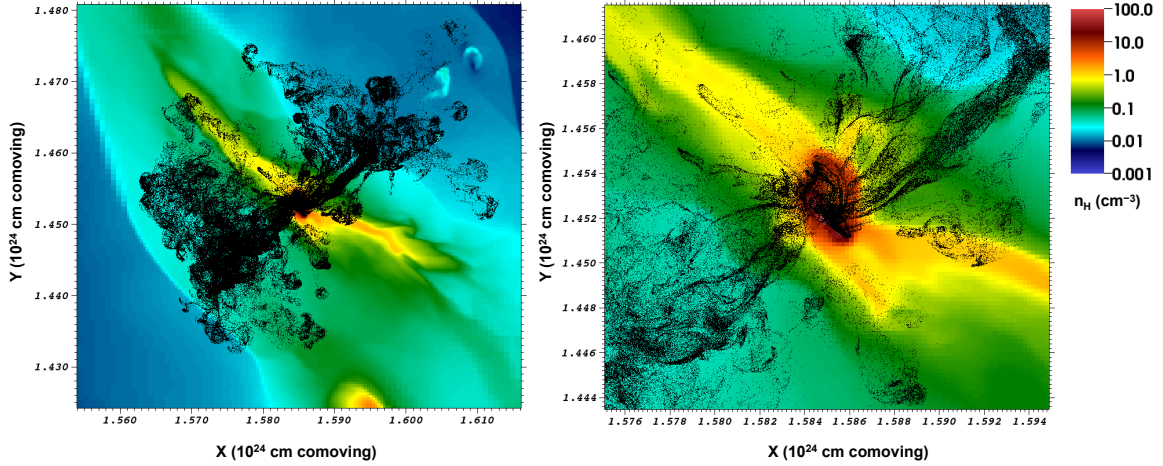


Figure 2.7: Metal dispersal and fallback at the end of the simulation, 40 Myr after the supernova explosion, at $z = 17$. The left panel is 1.1 kpc (physical) wide and centered on the gravitational potential minimum; the right panel is a 360 pc detail. The black points are the metal particles in projection, while the color shows a slice through the physical hydrogen density n_{H} . Metal-bearing Rayleigh-Taylor fingers have a positive radial velocity and have breached the virial radius of the halo, while a majority of the metal mass is falling back into the halo center and remains incompletely mixed with the primordial gas. Density in the central unresolved core exceeds coverage of the color scale and is $\sim 10^4 \text{ cm}^{-3}$.

quist, 2003; Salvaterra, Ferrara & Schneider, 2004; Machida et al., 2005; Chiaki, Yoshida & Kitayama, 2013). The Rayleigh-Taylor instability buckles and redistributes momentum in the shell. The highest momentum fragments continue semi-ballistically outward, consistent with the observation by Whalen et al. (2008b) that the blast wave of even a moderate 10^{51} ergs explosion has enough momentum to escape a standard minihalo. The low-momentum fragments, however, do not have sufficient momentum to escape; they turn around, fall back, and eventually join the central unresolved core. The falling ejecta make thin multiply-folded streams and filaments, indicating what seems to be a certain lack of mixing with the halo gas. The pristine gas accreting through the filaments of the cosmic web, and the ejecta-enriched gas accreting from the supernova remnant, meet in the central core. If the core is turbulent—poor resolution at this stage of the simulation would not allow us to detect such turbulence—turbulent mixing of the ejecta, now containing some swept up pristine gas, with a much larger mass of pristine gas would ensue.

2.2.3 Metal Enrichment

In Figure 2.8, we show the net rates of baryon and metal outflow from or inflow into the central 20pc of the halo. Some baryonic inflow is already evident early on, after 50kyr from the explosion, and after ≈ 1.5 Myr, baryons transition to permanent inflow. After ≈ 5 Myr, the inflow rate settles at $\dot{M}_b \approx 0.002 M_\odot \text{yr}^{-1}$. The metal flow transitions from outflow to inflow at ≈ 4 Myr after the explosion, and fluctuates in the range $\dot{M}_Z \sim (0.5 - 5) \times 10^{-7} M_\odot \text{yr}^{-1}$. The average asymptotic absolute metallicity of the inflowing material is

$$Z_{inflow} = \frac{\dot{M}_Z}{\dot{M}_b} \sim 10^{-4} \left(\frac{Z_{SN}}{0.1} \right) \sim 0.005 Z_\odot \left(\frac{Z_{SN}}{0.1} \right), \quad (2.4)$$

where we are referring to the total metal mass ignoring fractional abundances of individual metal species.

We proceed to examine the evolution of the metal-mass-weighted metallicity probability density function (PDF). The metallicity PDF is computed in three different ways. In the first, “fluid-fluid” method, the metallicity is obtained by summing the amplitudes of the passive scalars defining metal abundances on the computational grid. The metal mass at metallicity Z is then calculated by computing a volume integral of $Z\rho$ over the cells with metallicities in a narrow logarithmic bin containing Z . The shortcoming of this method is that it yields, as a consequence of a well-known shortcoming of passive scalar transport schemes, nonvanishing, small metallicities even in many cells that ejecta could not have reached on hydrodynamic grounds.⁵

With this in mind, the first method is more accurate where the metallicity is near its peak value, and is highly inaccurate elsewhere. Our remaining two methods for computing the metallicity PDF are designed to alleviate the impact of spurious diffusion.

In the second, “fluid-particle” method, the metallicity Z of a computational cell is calculated in the same way as in the first method, but the metal mass is calculated by summing

⁵The spurious diffusion can easily be understood by considering a step-function compositional discontinuity $Z(x) = H(x)$ in an otherwise uniform medium traveling in the x -direction with velocity $v_x > 0$, and let Δx be the grid cell size. The code approximates the solution to the transport equation $\partial Z / \partial t + v \partial Z / \partial x = 0$ by computing cell boundary fluxes with the piecewise-parabolic method; here, we adopt a simpler scheme after assuming that just to the right of the discontinuity, the metallicity of every cell is much smaller than that of the cell immediately to the left. Let Δt denote the computational time step and $\delta \equiv v \Delta t / \Delta x$ the dimensionless Courant parameter for fluid velocity, and assume that the discontinuity is slow, $\delta \ll 1$. Then it is straightforward to show that after $t / \Delta t$ steps, the metal-free region to the right of the traveling discontinuity will develop a spurious tail of nonzero metallicities of the asymptotic form $Z(x) \sim \binom{t/\Delta t}{x/\Delta x} \delta^{x/\Delta x}$, where the first factor is the binomial coefficient. The tail establishes itself with an unphysical speed $\Delta x / \Delta t \gg v$.

the mass of the ejecta tracer particles in the cell, and multiplying by the ejecta absolute metallicity $Z_{SN} = 0.1$. The tracer particle mass inside a cell is calculated with the cloud-in-cell method, with the weighting function taken to correspond to spreading the particle mass over a cubical kernel identical to the host cell, but centered on the particle. In the second method, only the cells having non-vanishing overlap with at least one tracer particle cloud-in-cell kernel contribute to the metallicity PDF. It should be kept in mind, however, that a metal particle displaced from the center of its host cell contributes mass to the neighboring cell that may be separated from the host cell by a shock transition or a contact discontinuity.

In the third, “particle-particle” method, the metallicity inside the cell is itself computed by summing up the metal mass inside the cell (again, as in the second method, computed by adding up tracer particle mass inside the cell and multiplying by Z_{SN}), and dividing this by the sum of the metal mass and the fluid hydrogen and helium masses in the cell. Since the combined abundance of hydrogen and helium is near unity, the third method completely ignores the fluid metallicity as defined by the passive scalar advected on the computational grid. Ejecta particles as tracers of metallicity obviously do not suffer from the same spurious diffusion as the fluid metallicity, but they are affected by systematic issues of their own. In convergent flows such as near the insufficiently well resolved snowplow shell, metal particles can get trapped in discontinuous flow structures, which can produce a spurious *increase* of local metallicity as computed by the third method. Thus, while the fluid metallicity is bounded from above by its maximum value, $Z_{SN} = 0.1$, at the point of injection, the particle-based metallicity can exceed this value and even approach unity.

In Figure 2.9, we show the metal-mass-weighted metallicity PDF at four different times: first, in the Sedov-Taylor phase, and, then at approximately 1, 13, and 40 Myr after the explosion. It is immediately clear that already at early times, the metallicity PDF exhibits a tail $dM_Z/d\ln Z \propto Z$ extending toward very low metallicities, where differences between the PDFs computed with the three methods became more severe. Spurious diffusion across compositional discontinuities in the fluid-based methods, and cloud-in-cell smearing in particle-based methods, both contribute to the tail. We also notice that the particle-particle method has developed a tail extending into the forbidden region, $Z > Z_{SN}$, a clear signature of spurious particle trapping.

As the supernova remnant ages, metal mixing in the complex interior flow, which is numerical in the simulation but can be facilitated by turbulence in nature (e.g., Pan, Scannapieco & Scalo, 2012), broadens the metallicity peak from its initial location at $Z \approx Z_{SN}$ to an approximate range $10^{-5} \lesssim Z \lesssim Z_{max}(t)$, where $Z_{max}(t)$ is a time- and PDF-extraction-

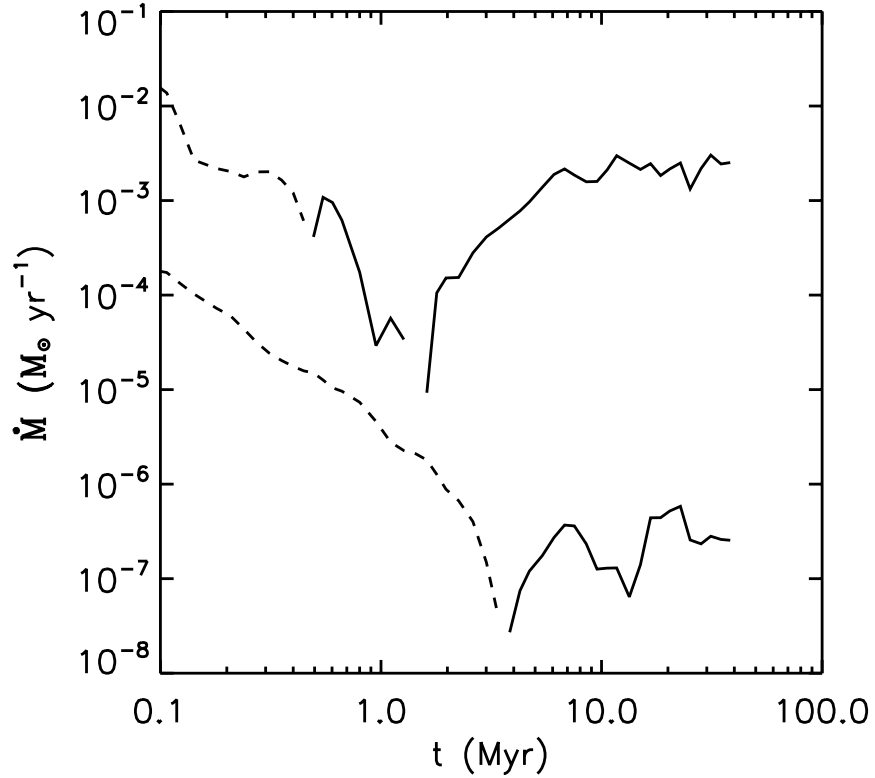


Figure 2.8: Metal (lower curve; \dot{M}_Z) and total baryon (upper curve; \dot{M}_b) net mass flow rate through a sphere of radius 20pc centered on the gravitational potential minimum. Dashed lines indicate outflows and solid lines inflows. The total mass of ejecta in the simulation is $M_{SN} = 40M_\odot$ and the metal mass is $M_Z = Z_{SN}M_{SN} = 4M_\odot$. Net outflow reverses into an inflow earlier in the baryons because of the presence of cold filaments delivering metal-free gas from the cosmic web into the halo center.

method-dependent maximum absolute metallicity. For fluid-based metallicity PDFs, we find that $Z_{max} \approx (0.07, 0.02, 0.002)$ at $t - t_{SN} \approx (1, 13, 40)$ Myr. We also notice a prominent narrow metallicity peak, built from cells belonging to the central, unresolved core that is accreting both from the pristine filaments of the cosmic web and from the ejecta-enriched supernova remnant fallback. The peak is migrating slowly toward lower metallicities, covering $Z_{core} \approx (2, 0.7, 0.3) \times 10^{-4}$ in the same three epochs. The metallicity of the unresolved core is consistent with the average metallicity of the accreting fluid given in Equation (2.4).

Finally, we turn to the energetics of the metal-enriched material. In Figure 2.10, we show the evolution of the total kinetic and internal (thermal) energy of fluid elements having absolute metallicity $Z \geq 10^{-6}$. At 1 kyr after the explosion, the kinetic energy decreases

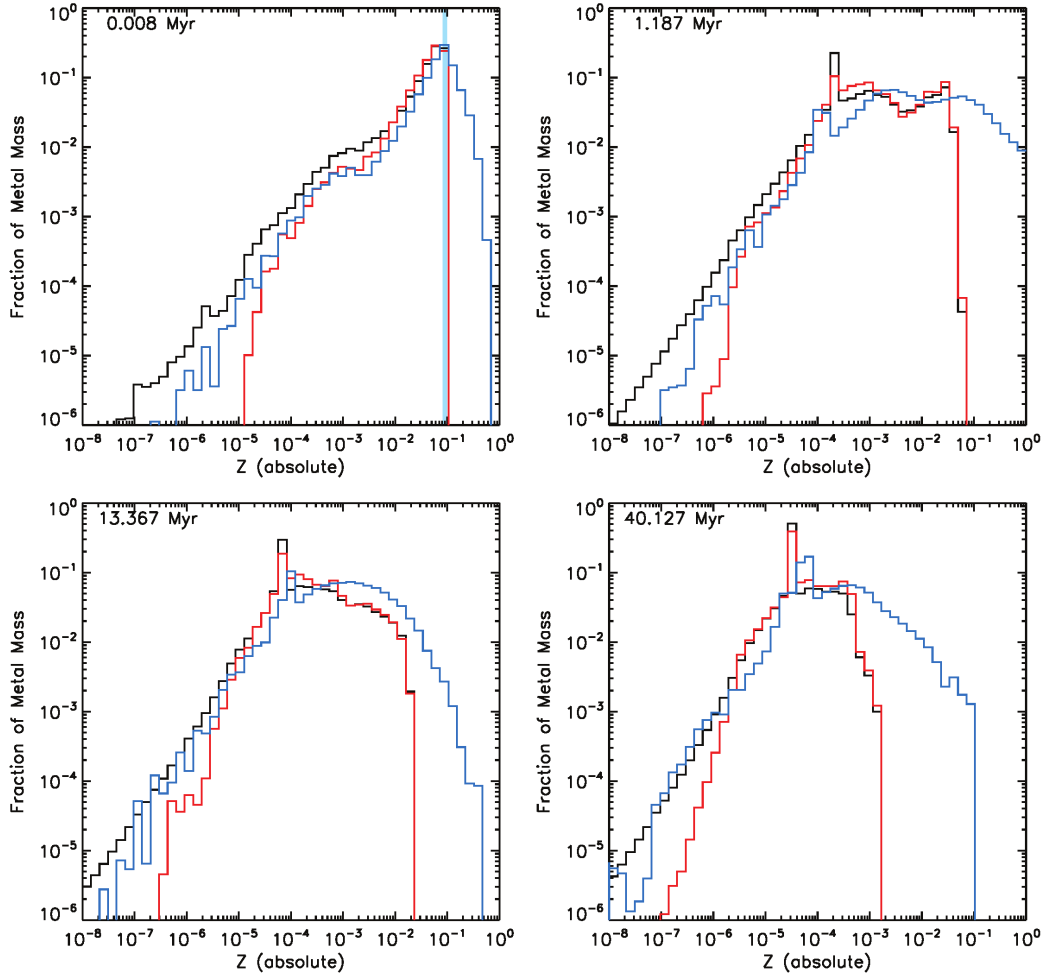


Figure 2.9: Absolute metallicity distribution at four different times after the supernova. The histograms show the fraction of total metal mass as a function of absolute metallicity calculated in three different ways: by computing the metallicity and metal mass from the fluid variables defined on the AMR grid (black curve), by computing metallicity from the fluid variables and metal mass from the Lagrangian particles tracing the supernova ejecta assuming ejecta metallicity of $Z_{SN} = 0.1$ (red curve), and by computing both metallicity and metal mass with the Lagrangian particles (blue curve). The blue column in the first histogram shows the initial metallicity of the ejecta. The peak at $Z \approx (2, 0.7, 0.3) \times 10^{-4}$ at $t - t_{SN} = (1.187, 13.367, 40.127)$ Myr contains the fluid that has become incorporated in the central unresolved core (please see text for additional explanation).

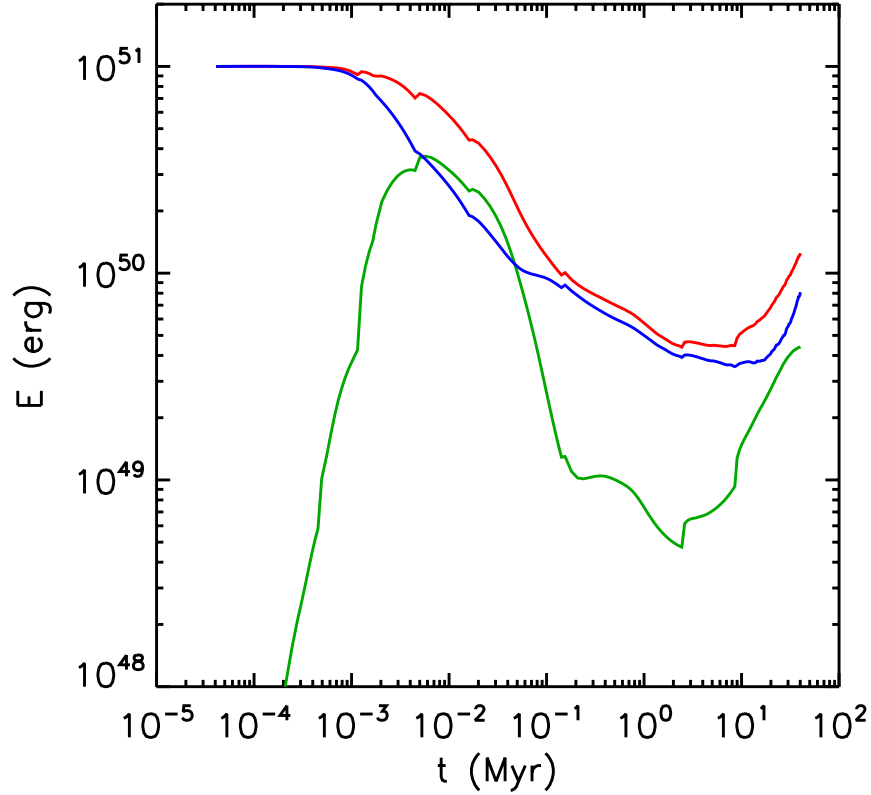


Figure 2.10: The kinetic (blue curve), internal (green curve), and combined kinetic and internal (red curve) energy of the metal enriched fluid, defined as the fluid with absolute metallicity $Z \geq 10^{-6}$.

below its initial value when the ejecta start interacting with the ambient medium and the well-resolved reverse shock facilitates kinetic-to-internal conversion. Adiabatic and radiative cooling both contribute to the rapid decrease of internal energy at $0.01 - 1.0$ Myr after the explosion. The renewed rise of both energies in the old remnant reflect the fallback of ejecta-enriched fluid into the halo center.

2.3 Discussion

Existing treatments of metal injection by Pop III supernovae have followed the excursion of the metal-endowed ejecta into the cosmic environment and their possible fallback into dark matter halos, but usually with one-dimensional simulations (Kitayama & Yoshida, 2005; Whalen et al., 2008b) or relatively low-resolution three-dimensional, grid-based or

smoothed particle hydrodynamic simulations (Nakasato & Shige-
yama, 2000; Bromm & Loeb, 2003a; Greif et al., 2007; Wise & Abel, 2008b). These treatments point to a prompt and widespread dispersal of supernova ejecta into the primordial IGM if one assumes that the supernovae were extraordinarily energetic, e.g., consistent with the popular hypothesis that the Pop III stars exploded as PISNe. However, in particularly high mass halos or those hosting moderate mass stars, the detailed dynamics of the ejecta is sensitive to the pre-supernova evolution of the HII region. With one-dimensional hydrodynamic simulations, Whalen et al. (2008b) showed that the HII region of a moderate mass star at the center of the minihalo may remain confined within the minihalo. They calculated that the blast wave of a 10^{51} ergs supernova in $\lesssim 10^6 M_\odot$ minihalos, does, after ~ 10 Myr, reach the virial radius of the halo, and concluded that this results in the “disruption” of the baryonic component of the halo. They also considered high-mass $\sim 10^7 M_\odot$ minihalos in which a strong photodissociating background had prevented star formation (e.g., O’Shea & Norman, 2008), and found that there the HII region may not break out and the supernova blast wave may be confined at very small radii. They speculated that the subsequent prompt fallback of metal-enriched supernova ejecta into the center of the halo could lead to the formation of a globular-cluster-like stellar system, similar to the suggestion of Wada & Venkatesan (2003) that a relatively small number of supernovae exploding in a more massive, $\sim 10^8 M_\odot$ cosmic halo could also lead to a fallback and prompt star cluster formation. This is a particularly interesting possibility, in view of the unexplained origin of metal-poor globular clusters (Brodie & Strader, 2006): do they form in the centers of their own low-mass dark matter halos (e.g., Peebles, 1984; Rosenblatt, Faber & Blumenthal, 1988; Bromm & Clarke, 2002; Boley et al., 2009; Griffen et al., 2010), or do they form off-center in the merging and fragmentation of more massive protogalactic disks (e.g., Kravtsov & Gnedin, 2005, and references therein)?

It is important to realize that the fate of the supernova ejecta may be influenced by dynamical processes operating on relatively small spatial scales and strongly violating spherical symmetry. In addition to the likely intrinsic asphericity of the explosion itself, one such process is the Rayleigh-Taylor instability of the decelerating contact discontinuity after the ejecta have started to interact with the ambient medium. The ambient medium into which the supernova expands is bound to be inhomogeneous, especially if the luminosity of the progenitor stars and other hot stars that have formed with it is insufficient to completely photoionize the densest clumps remaining from the progenitor gas cloud. On the somewhat larger ~ 100 pc scales of the host minihalo, a pronounced departure from spherical

symmetry will arise from the filamentary geometry of the cosmic web. Such asymmetry can interact with the expanding blast wave. Further, as an aging supernova remnant forms a thin, momentum-conserving snowplow shell, the decelerating shell is itself unstable to the Rayleigh-Taylor instability and forms fingers. Finally, while the blast wave instabilities lead to partial entrainment of the ejecta and the shocked primordial gas, any ejecta-enriched gas falling back toward the center of the halo, where it may engage in a new round of star formation, may not necessarily be chemically homogeneous (full chemical mixing requires at least a few turbulent eddy turnover times which may not be available in the blast wave). Most of these phenomena remain to be explored in the context of Pop III stars; the results we have presented here are one of the first steps in that direction.

2.3.1 Metal-Enriched Star Formation: Continuous, Bursty, or Self-Limiting?

The prompt resumption of baryonic infall into the center of the cosmic minihalo suggests that star formation could resume on similarly short, $\sim 1-5$ Myr, time scales. In the simulation presented here, the metals that the supernova has synthesized begin returning to the halo center ~ 4 Myr after the explosion. The mean metallicity of the inflow, averaged over the primordial streams and the metal-enriched collapsing supernova remnant streams converging in the center of the halo, is $\sim 0.005 Z_{\odot}$ assuming a net supernova metal yield of $4 M_{\odot}$. If the metal-rich gas successfully mixes with the primordial gas, then, according to a prevailing belief, the metallicity of the combined streams is well sufficient to ensure that new star formation in this gas should be producing normal, low-metallicity Pop II stars. The Pop III to II transition cannot be ascertained in the present simulation because we do not adequately resolve the cold gas at densities $n_{\text{H}} \gtrsim 100 \text{ cm}^{-3}$. This gas belongs to the central core and is colder than primordial gas at the same densities preceding the insertion of the first star. It is at unresolved densities that the metallicity of the gas strongly affects the thermodynamic evolution and thus governs the outcome of fragmentation (e.g., Omukai et al., 2005; Santoro & Shull, 2006; Schneider et al., 2006; Smith et al., 2009; Safranek-Shrader, Bromm & Milosavljević, 2010, assuming low metallicities, $Z \lesssim 0.01 Z_{\odot}$).

The gaseous core in the center of the minihalo that is fed by metal-enriched streams can be compared to the star-forming core of a giant molecular cloud (GMC). We attempt such comparison with an eye on the overall hydrodynamics of the gas flow, putting aside any differences in chemical composition, dust content, CMB temperature, etc., in the two

systems. Dense GMC cores grow by accreting from larger-scale, lower-density cloud environments which are supersonically turbulent. Smaller cores and their embedded proto star clusters merge with each other to form larger associations. Star formation in the cores is thought to be self-regulated, with the “feedback” from ongoing star formation controlling the amount of star-forming gas available and eventually leading to GMC dissolution (e.g., Murray, Quataert & Thompson, 2010; Murray, 2011; Goldbaum et al., 2011; Lopez et al., 2011). The feedback entails, e.g., the pressure of the HII regions and the pressure of direct stellar radiation. While the baryonic mass of a cosmic minihalo is perhaps smaller than that of a GMC, the centrally concentrated underlying dark matter halo renders the gravitational potential depth in a minihalo’s central gaseous core similar to that in a GMC’s star-forming core. The underlying dark matter gravitational potential may make a cosmic minihalo less susceptible to star-formation-induced dissolution than a GMC, assuming that the two systems are forming stars at the same rate.

GMCs are thought to sustain star formation over tens of millions of years, in spite of the HII regions, supernovae, and other feedback activity that commences quickly following the formation of the first massive stars. The feedback’s impact preceding the eventual dissolution of the cloud complex may be limited to reducing the average star formation rate. We do not know whether star formation in metal-enriched minihalos and their descendent $\gtrsim 10^7 M_\odot$ halos can be sustained as in GMCs in spite of the feedback, or is the feedback from second-generation stars so effective as to evacuate baryons from the halo and prevent further star formation on cosmological time scales (see, e.g., Mori, Ferrara & Madau, 2002; Frebel & Bromm, 2012). It seems that these two scenarios can be evaluated only with attention to the detailed, small-scale mechanics of star formation and its feedback. A corollary of the first scenario would be the presence of multiple, chemically distinct stellar populations in the stellar system that forms this way.

The statistics of low-luminosity stellar systems in the Local Group in conjunction with theoretical modeling of structure formation in a Λ CDM universe suggests that star formation must have, to some extent, been suppressed in low-mass cosmic halos (e.g., Susa & Umemura, 2004a; Ricotti & Gnedin, 2005; Gnedin & Kravtsov, 2006; Moore et al., 2006; Madau, Diemand & Kuhlen, 2008; Bovill & Ricotti, 2009, 2011; Kaposov et al., 2009; Muñoz et al., 2009; Salvadori & Ferrara, 2009; Busha et al., 2010; Gao et al., 2010; Griffen et al., 2010; Macciò et al., 2010; Okamoto et al., 2010; Font et al., 2011; Lunnan et al., 2012; Rashkov et al., 2012). This suppression, however, could have arisen both internally, as in GMCs, and externally, where the suppression is driven by the heating of the IGM

by the background ionizing radiation coming from other, more massive but less common halos (e.g., Thoul & Weinberg, 1996; Kepner, Babul & Spergel, 1997; Barkana & Loeb, 1999; Shapiro, Iliiev & Raga, 2004; Susa & Umemura, 2004b; Mesinger, Bryan & Haiman, 2006; Mesinger & Dijkstra, 2008; Okamoto, Gao & Theuns, 2008). The heating could have shut off the inflow of fresh gas into the halo, eventually stunting star formation. The prevalence of either suppression mechanism as a function of halo properties cannot be understood without first understanding the detailed mechanics of star formation and feedback following the initial fallback of Pop III supernova ejecta.

2.3.2 Uncertainties Related to the Nature of First Stars

A source of uncertainty regarding the formation and nature of the first metal-enriched star clusters is the incomplete understanding of the precise character of metal-free Pop III stars, and of the energetics and nucleosynthetic output of the associated supernovae. Theoretical investigations of Pop III star formation have not yet converged and the precise functional form of the resulting initial mass function is not yet known. The evolution of metal-free stars is very sensitive to their poorly-understood internal rotational structure starting with the protostellar phase (see, e.g., Stacy, Bromm & Loeb, 2011; Stacy et al., 2013), and on the potential presence of a close companion. Similarly, the explosion mechanism in metal-poor stars is not known. Each of the suggested mechanisms, including the standard delayed-neutrino mechanism hypothesized to drive Type II explosions, and the pair-instability and pulsational pair-instability mechanisms expected in relatively massive metal-free stars (see, e.g., Heger & Woosley, 2002; Chatzopoulos & Wheeler, 2012; Yoon, Dierks & Langer, 2012, and references therein), as well as the more exotic “hypernova”-type mechanisms involving a (possibly magnetized) outflow from a central compact object, implies its own characteristic explosion energy and nucleo-synthetic imprint.

Another aspect of the final stellar demise that should be very sensitive to both the stellar mass and rotation is the nature of the compact remnant, if any, that it leaves behind. While the pair instability disperses the star completely, leaving no remnant, core collapse in stars with initial masses $\gtrsim 15 - 25 M_{\odot}$ (the precise threshold mass depending on unknown aspects of the explosion; see, e.g., Heger et al., 2003; Zhang, Woosley & Heger, 2008) leaves behind a black hole, either via direct collapse into one, or by fallback of the ejecta onto the neutron star. The black hole may be produced with an initial kick that would eject it from the dark matter halo (Whalen & Fryer, 2012), but if the kick is small and the black hole

is retained near the gravitational center, it could accrete the gas collecting in this region. The energy liberated in this accretion could be another, potentially significant source of feedback. The accretion rate and the luminosity of this source would be subject to complex radiation-hydrodynamic couplings that are only understood under the most idealized assumptions, such as in an absence of shadowing by or radiation trapping within the innermost accretion flow (see, e.g., Milosavljević, Couch & Bromm, 2009; Milosavljević et al., 2009; Park & Ricotti, 2011, 2012; Li, 2011). To date, only very few cosmological simulations investigating the impact of the radiation emitted by accreting first-star remnants on hydrodynamics in the host halo have been carried out (e.g., Kuhlen & Madau, 2005; Alvarez, Wise & Abel, 2009; Johnson & Khochfar, 2011; Jeon et al., 2012) and only a partial picture of the feedback on second generation star formation is available. Jeon et al. (2012) show that X-rays from the remnant impact the cosmic neighborhood in complex ways but do not entirely prevent (and can actually promote) gas cooling and star formation. Much remains to be understood about the role of compact remnants in the evolution of the first galaxies.

Many investigations of the formation of first stars and galaxies and their role in reionization have explored implications of the hypothesis that Pop III stars had high masses, explosion energies, and metal yields. We find that the opposite limit of moderate masses, explosion energies, and metal yields might imply sharply divergent outcomes, not only for the parent cosmic minihalos, but also for the overall pace of transformation of the early universe. A related issue is the nature of the first galaxies (for a review, see Bromm & Yoshida, 2011). Their assembly process is influenced by the feedback from the Pop III stars that formed in the minihalo progenitor systems, and this feedback in turn sensitively depends on the mass scale of the first stars. In the case of extremely massive stars, negative feedback is very disruptive, completely sterilizing the minihalos after only one episode of star formation. Only after $\sim 10^8$ yr did the hot gas sufficiently cool to enable the recollapse into a much more massive dark matter halo, where a second-generation starburst would be triggered (Wise & Abel, 2008b; Greif et al., 2010). This separation into two distinct stages of star formation would be smoothed out in the case studied here. Indeed, the first galaxies may then already have commenced their assembly in massive minihalos, as opposed to the atomic cooling halos (e.g., Oh & Haiman, 2002) implicated in the previous scenario.

2.4 Conclusions

We have carried out a cosmological hydrodynamical simulation designed to investigate the evolution of a cosmic minihalo in the aftermath of the formation of the first, Pop III star, assuming that the star has a moderate mass and explodes as a moderate-energy Type II-like supernova, consistent with the recent downward revision of Pop III stellar mass estimates (Stacy, Greif & Bromm, 2010, 2012a; Clark et al., 2011a; Greif et al., 2011, 2012; Hosokawa et al., 2011). We analyzed the dynamics of supernova ejecta and gas flow inside the minihalo. These can be compared to similar studies involving massive Pop III stars exploding as ultra-energetic PISNe. Our main conclusions are as follows.

The moderate-mass star and the moderate-energy supernova it produces inflict significantly smaller damage to the host minihalo than that inflicted by a massive star exploding as an ultra-energetic supernova. The star only partially photoionizes the host halo. The densest gas flowing from the filaments of the cosmic web into the star’s parent cloud remains neutral and survives the supernova blast wave. This dense gas resumes accretion into the center of the minihalo only ~ 1 Myr after the explosion. After ~ 20 Myr, all spherically-averaged baryonic mass coordinates are moving inward and the accretion rate at the center of the halo is $\sim 0.002 M_{\odot} \text{yr}^{-1}$.

Following instability of the blast wave during the snowplow phase, a fraction of the supernova ejecta starts falling back to the center of the halo. The ejecta fallback accretion rate reaches a steady state after ~ 5 Myr. The accreting ejecta are incompletely mixed with the primordial gas and are confined in thin sheets and filaments. Less than a half of the ejecta escape the virial radius; the escaping ejecta can be traced back to the outermost Rayleigh-Taylor fingers.

The average metallicity of the accreting matter is in the range $0.001 - 0.01 Z_{\odot}$. This result depends on the assumed supernova energy and metal yield, but in this study, we did not pursue parameter space exploration. The metallicity of the accreted gas is sufficient to ensure that new stars forming in the central core, unresolved in the simulation, will have even lower characteristic masses.

These results bring into focus metal-enriched star formation in cosmic minihalos and their immediate descendant halos. The character of post-supernova metal transport and gravitational fragmentation of the metal-enriched gas, and of the impact of subsequent star formation and supernovae, are both worth addressing in follow-up investigations. The early universe likely exhibited a range of different explosion settings, from modest to ultra-

energetic. It will be intriguing to see how these high-redshift systems are matched with possible local fossils, such as the ultra-faint dwarf galaxies (e.g., Bovill & Ricotti, 2009; Salvadori & Ferrara, 2009; Tumlinson, 2010) and metal-poor globular clusters (e.g., Brodie & Strader, 2006). From what we have already learned, Pop III supernova feedback appears to play a key role in shaping early cosmic history and the nature of relic stellar systems.

Chapter Three: Metal transport and chemical heterogeneity in early star forming systems¹

The chemical abundance patterns of metal-poor and ancient stellar populations and intergalactic absorption systems provide information about the earliest stages of chemical enrichment (for reviews, see Beers & Christlieb, 2005; Frebel & Norris, 2013a; Karlsson, Bromm & Bland-Hawthorn, 2013; Frebel & Norris, 2015). Because the first stellar systems were likely enriched by only a few discrete sources, one must interpret the inherent complexity of enrichment in relating the abundance patterns measured in metal-poor stars to theoretical models (Audouze & Silk, 1995; Shigeyama & Tsujimoto, 1998). Cosmic star formation, the driver of enrichment, is already stochastic thanks to the randomness of cosmic primordial density fluctuations. Significant additional complexity enters chemical enrichment through the turbulent hydrodynamics of the intergalactic, circumgalactic, and interstellar medium, the stochasticity of the star formation process, and the mechanics of the dispersal of nucleosynthetic products from their sources—supernovae and stellar mass loss. The effects of complexity are partially, though perhaps not completely erased through the stirring and mixing in mature star forming systems like the Milky Way’s disk. But in ancient stellar populations, we expect vestiges of the complexity to persist, requiring us to model it as much as possible from first principles.

The recent years have seen a class of high-resolution simulations of small numbers of primordial star forming systems (e.g., Wise & Abel, 2008a; Greif et al., 2010; Wise et al., 2012, 2014; Ritter et al., 2012; Jeon et al., 2014) as well as of moderate-resolution simulations (somewhat farther removed from the first-principles philosophy) that allow the authors to track large samples of such systems (e.g., Ricotti, Gnedin & Shull, 2008; Bovill & Ricotti, 2009; Tassis, Gnedin & Kravtsov, 2012; Muratov et al., 2013; O’Shea et al., 2015). Without exception, these works study the local enrichment amplitude as quantified by the metallicity but do not attempt to investigate potential complex effects that could influence differential chemical abundance patterns.

A critical source of uncertainty entering chemical evolution models is the chemical yields of supernovae. The yields could vary drastically with the progenitor mass, rotation

¹This chapter was published as Ritter J. S., Sluder A., Safronek-Shrader C., Milosavljević M., Bromm V., 2015, MNRAS, 451, 1190, under the supervision of Miloš Milosavljević.

rate, the presence of a binary companion, and initial metal content (e.g., Heger & Woosley, 2002, 2010). In the case of core-collapse supernovae, first-principles theoretical modeling is still not sufficiently predictive to permit direct synthesis of the observed stellar chemical abundance patterns. What is worse, the yields may not be deterministic and could be sensitive to instabilities taking place immediately prior to and in the course of the explosion (e.g., Arnett & Meakin, 2011; Ellinger et al., 2012; Wongwathanarat, Janka & Müller, 2013; Smith et al., 2015a; Couch et al., 2015). It has therefore been a longstanding hope that the process of nucleosynthesis will be reverse engineered from the abundance patterns (e.g., Talbot & Arnett, 1973; Nomoto, Kobayashi & Tominaga, 2013). Principal component analysis (PCA) can be applied in the stellar chemical abundance space to discern the contributing classes of nucleosynthetic sources, be they individual stars or star clusters (e.g., Ting et al., 2012), if one posits that abundance patterns of the sources define monolithic basis vectors of the resulting stellar chemical abundance space. This is becoming a particularly promising direction with the arrival of large spectroscopic surveys such as HERMES-GALAH (Zucker et al., 2012; De Silva et al., 2015) and Gaia-ESO (Gilmore et al., 2012) surveys. However, the applicability of PCA becomes less clear if the hydrodynamics of metal dispersal skews the patterns, introducing biases deviating the patterns from linear superpositions of the patterns of well-defined nucleosynthetic source classes. Properly characterizing such biases would place the recovery of the properties of nucleosynthetic sources from stellar abundance data on much firmer footing.

The most primitive and metal-poor stellar populations known are the ultra-faint dwarf spheroidal satellites of the Milky Way (UFDs; Brown et al., 2012; Frebel & Bromm, 2012; Vargas et al., 2013; Frebel, Simon & Kirby, 2014), the Milky Way’s stellar halo which is thought to have formed (at least in part) through the disruption of dwarf satellite galaxies (Kirby et al. 2008, Norris et al. 2010a, Lai et al. 2011, but see, e.g., Lee et al. 2013) and possibly an old, metal-poor sub-population within the Milky Way bulge.² The prominent chemical heterogeneity in UFDs is often invoked as a potential indicator of poor mixing of supernova ejecta or an enrichment by a small number of contributing supernovae (e.g., Norris et al., 2010b; Simon et al., 2015). The primitive populations could be particularly sensitive to hydrodynamical biases, given the low masses and gravitational potential well depths of the progenitor star-forming systems and the low numbers of contributing supernovae and AGB stars.

²We can define a stellar population as “primitive” if the number of times the nucleosynthetic output of individual supernovae and AGB stars has been recycled is small.

Here we make an initial attempt to identify these biases with ultra-high-resolution cosmological hydrodynamic simulations. We track the degree of chemical heterogeneity in the enrichment by a single supernova, and by a cluster of seven consecutive supernovae. The supernovae explode in a previously metal-free cosmic minihalo, a plausible UFD progenitor (Ricotti, Gnedin & Shull, 2008; Salvadori & Ferrara, 2009). The two simulations are initialized from Gaussian cosmological fluctuations, ensuring that the cosmic environment being enriched is realistic.

The finite resolution of the simulations implies that we are able to directly place only a lower limit on the degree of *coarse-grained* chemical heterogeneity. Perfect chemical homogeneity, down to molecular scales, is expected only if the gas has been stirred by such processes as gravitational infall, the mechanical feedback from star formation, and thermal instability, to the extent that would facilitate microscopic diffusion across chemically heterogeneous sheets produced by turbulent folding. Efficient stirring generally requires that the vortical time $\sim |\nabla \times \mathbf{v}|^{-1}$ be much shorter than the lifetime of a cloud before it collapses to form new stars (see, e.g., Pan & Scannapieco, 2010, and references therein). This condition can be fulfilled in specific sites, but certainly not in general.³

We study the transport of supernova ejecta resolved by the mass coordinate inside the progenitor star (in the simulation with one supernova) and by the temporal order of the explosion (in the simulation with multiple supernovae). We follow the transport until gas clouds have assembled in which second-generation stars can be expected to form. This allows us to determine if these nucleosynthetic sources contribute monolithically, defining invariant basis vectors of the chemical abundance space, or if, perhaps, the hydrodynamics of supernova remnant evolution favors the reprocessing into new stars of only a biased subsample of the gross nucleosynthetic yields, skewing toward the reprocessing of some elements but not others.

3.1 Numerical Methodology

The simulations were initialized from the same realization of cosmological initial conditions as in Safranek-Shrader et al. (2012) and Ritter et al. (2012). We simulated the gravitational collapse of collisionless dark matter and baryonic fluid in a box of size 1 Mpc (co-moving) starting at redshift $z = 146$. The initial density and velocity perturbations were gen-

³Microscopic chemical mixing is a sufficient, but not a necessary condition for chemical homogeneity, since any residual heterogeneity on sub-stellar mass scales is erased in the stars themselves.

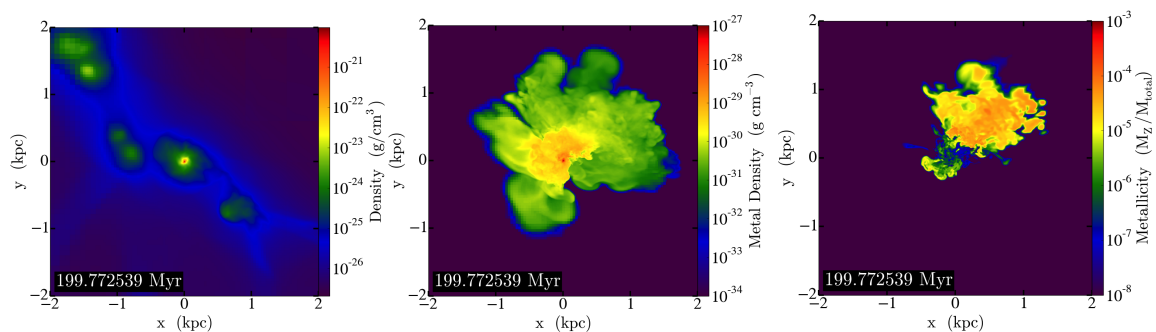


Figure 3.1: Simulation 7SN 200 Myr after the first supernova explosion: density-weighted density projection ($\int \rho^2 dz / \int \rho dz$, left), metal-density-weighted metal density projection ($\int \rho_Z^2 dz / \int \rho_Z dz$, middle), and metallicity slice through the cell with maximum density (right). The metal density is derived from the advected passive scalar tracing supernova ejecta. The cosmic web filament extends diagonally from top left. Note the relatively low metallicity near the center, resulting from a dilution of supernova ejecta with metal-free gas streaming down the cosmic web filament.

erated with the multiscale cosmological initial conditions package GRAFIC2 (Bertschinger, 2001) with Wilkinson Microwave Anisotropy Probe 7-year cosmological parameters (Komatsu et al., 2011). We utilized two levels of nested refinement to achieve an effective resolution of 512^3 , corresponding to $230 M_\odot$ per dark matter particle, in a patch encompassing the density maximum on mass scales $10^8 M_\odot$. Time integration was carried out with the adaptive mesh refinement (AMR) code FLASH (Fryxell et al., 2000) as described in Safranek-Shrader et al. (2012). In what follows, we use physical units as opposed to comoving units. Metallicities are quoted in absolute metal mass fractions unless specified otherwise.

Gas cooled by H_2 ro-vibrational emission collapsed to form a $\approx 10^6 M_\odot$ minihalo at redshift $z \sim 19.6$. We inserted a single collisionless particle at the location of the gas density maximum within the minihalo to represent a Population III star (simulation 1SN) or a small cluster of such stars (simulation 7SN). The equivalent gas mass was removed by reducing the nearby gas density to a constant maximum level. In view of the recent realization that protostellar disk fragmentation (Stacy, Greif & Bromm, 2010; Clark et al., 2011c,b; Greif et al., 2011, 2012) and evaporation by protostellar radiation (Hosokawa et al., 2011; Stacy, Greif & Bromm, 2012b) can limit the masses of Population III stars in the few tens of solar masses, we picked their masses to be in the range $20 - 80 M_\odot$ with typical values $\sim 40 M_\odot$ and assumed for simplicity that they all exploded with energies 10^{51} erg. Preceding the

first explosion, we let the collisionless particle emit ionizing radiation for 3 Myr with an ionizing luminosity Q_{ion} and create an H II region. Hydrodynamic expansion of the ionized gas reduced the central gas density to $n \sim 0.3 \text{ cm}^{-3}$. After 3 Myr, we either inserted a single supernova remnant (1SN; $Q_{ion} = 6 \times 10^{49} \text{ photons s}^{-1}$) or initiated a sequence of 7 consecutive supernovae (7SN; $Q_{ion} = 2.2 \times 10^{50} \text{ photons s}^{-1}$), all centered on the location of the collisionless particle.

In 1SN we excised from the cosmological simulation a 1 kpc region centered on the collisionless particle, replacing the dark matter particles with a simple, parametric, spherically symmetric, time-dependent analytical dark matter density profile. The analytical profile was centered in the initial, instantaneous local rest frame of the host dark matter halo. The baryonic density and velocity field from the cosmological box was mapped directly onto the excised region, allowing us to continue the simulation in the interior of the excised region at high spatial resolution. The supernova ejecta mass was set to $40 M_{\odot}$. In 7SN, the seven supernova delay times 3.1–7.7 Myr (measured after collisionless particle insertion) were selected to represent the lifetimes of stars with masses decreasing from 80 to $20 M_{\odot}$, following a stellar IMF with a flat $dN/d \ln M$. Each of the supernovae was inserted in the free expansion phase, with $E_{SN} = 10^{51} \text{ erg}$ in kinetic energy and an initial radius smaller than one-tenth of the radius containing gas mass equal to that of the ejecta. The ejecta masses were in the range 25– $18.5 M_{\odot}$, decreasing with the order of the explosion.

We terminated each simulation when sufficient gas returned to the halo center to form a self-gravitating cloud with density $> 10^3 \text{ cm}^{-3}$, which happened 56 and 198 Myr after collisionless particle insertion in simulations 1SN and 7SN, respectively.

3.1.1 Thermodynamic Evolution

Preceding the insertion of the collisionless star particle we integrated the full set of coupled rate equations of the nonequilibrium chemical network for the primordial chemical species H, He, and D, their common ions, and the molecules H_2 and HD (Safranek-Shrader et al., 2012). After insertion of the star particle we turned on an ionizing point source. We mapped the gas density onto a source-centered spherical grid partitioned using the HEALPIX (Górski et al., 2005) algorithm in the angular coordinate (3000 pixels) and logarithmically in the radial coordinate (100 radial bins). The flux in any spherical cell was diminished by the cumulative extinction in the cells at smaller radii. We then mapped the flux from the spherical grid back onto the Cartesian simulation grid. On the basis of the

mapped flux, we determined if a cell was expected to be ionized. We assumed photoionization equilibrium in ionized cells and interpolated the local thermodynamic state of the gas from data tabulated with the code CLOUDY (Ferland et al., 2013) as a function of the ionization parameter proportional to the local hydrogen-ionizing flux divided by the total hydrogen number density.⁴

When the first supernova remnant was inserted, we switched off the photoionizing source and began computing the cooling rates assuming that the species’ abundances were in collisional ionization equilibrium. Here, the cooling rate and the ionization state were again interpolated from tables pre-computed with CLOUDY, now as a function of density, temperature, and metallicity. For the interpolation we used the metallicity as defined by the passive mass scalar metallicity on the Cartesian grid. Artificial diffusion (or, better, “numerical teleportation”) of the passive scalar metallicity is a problem hitherto unsolved in Eulerian codes (see, e.g., Footnote 6 in Ritter et al., 2012). It produces pseudo-exponential low-metallicity tails ahead of advancing metallicity fronts. In the hot, shocked shell preceding the supernova ejecta, the teleportation tail is present, but the metallicity in the tail is too low to contribute to gas cooling. In gas with temperature $\gg 10^4$ K, metal cooling begins to dominate only at metallicities $\gtrsim 0.1 Z_{\odot}$, higher than in the artificial tail. On the other hand, at low temperatures $\ll 10^4$ K, metallicities even as low as $\lesssim 10^{-3} Z_{\odot}$ (and $\sim 10^{-6} Z_{\odot}$ in the presence of dust) can define the cooling rate.

Similar to the numerical teleportation of chemical abundance scalar tracers, there is the potential of insidious mass teleportation at the contact discontinuity separating the hot, shock-heated gas of the supernova bubble from the much colder gas inside the enveloping dense cooling shell. Our calculations do not include the conduction of heat from the hot to the cold side of the interface. The net effect of thermal conduction should either be a cooling flow condensing the hot into the cold phase, or a reverse, evaporation flow, depending on the structure of the interface. For the specific temperature gradients and densities in our simulations, one would expect the heat conduction to produce an evaporation rather than a cooling flow (e.g., Cowie & McKee, 1977; Draine, 2011). The simulations exhibit a pressure dip at the interface, implying a narrow cooling layer. This arises from the artificial numerical smearing of the contact discontinuity. Dense gas from the cold side smears over onto the hot side thus artificially lowering the cooling time in a layer one cell thick. The cell-thick pressure dip is an under-resolved hydrodynamic feature. The numerical artifacts

⁴While not photon-conserving, this method is sufficient to simulate the anisotropic H II region expansion in the relatively dense gas of our minihalo.

that it may produce should be sensitive to the particulars of the numerical scheme such as the choice of slope limiter and approximate Riemann solver.

Since accurate tracking of molecular processes requires integration of stiff and computationally expensive chemical rate equations, to accelerate the computation, we did not track the H_2 abundance and did not include molecular cooling after the first supernova remnant insertion. This is a potential oversimplification as H_2 should form as the photo- and supernova-ionized gas recombines. Absent a high dust abundance that would drive molecule formation on grains (we do not track dust but its abundance is limited from above by the metallicity that remains low), H_2 abundance in the recombined gas should be $n_{\text{H}_2}/n_{\text{H}} \sim 10^{-3} - 10^{-2}$ (e.g., Mac Low & Shull, 1986; Shapiro & Kang, 1987; Kang & Shapiro, 1992). Molecule abundance reaches maximum within about a million years after gas cools below 10^4 K. In our simulation, this gas has metallicity $\ll 10^{-2} Z_{\odot}$ and cooling by H_2 should dominate (Glover & Clark, 2014), at least in a relatively narrow density range $n_{\text{H}} \sim 10 - 100 \text{ cm}^{-3}$ (see, e.g., Figure 6 in Safranek-Shrader, Milosavljević & Bromm, 2014a). Again barring a full atomic-to-molecular transition that would require abundant dust, at still higher densities $\gtrsim 100 \text{ cm}^{-3}$, metal line cooling dominates even before molecular transitions thermalize at $\sim 10^4 \text{ cm}^{-3}$.

The artifact of our neglecting molecular cooling at densities $\sim 10 - 100 \text{ cm}^{-3}$ is that the supernova-enriched, recollapsed gas will linger longer under quasi-hydrostatic conditions; a longer interval will pass before gravitational potential well becomes deep enough to compress the quasi-isothermal gas to the threshold of runaway gravitational collapse. The results that follow should be interpreted as placing an upper limit on the cooling and recollapse time in a supernova-enriched dark matter minihalo following a single supernova or a cluster of supernovae. The limit is strictly valid only in the fine-tuned regime in which molecule formation is completely suppressed by a dissociating UV background. The true recollapse time could be factor of a few shorter than in our simulations if the molecular abundance is significant. We will specifically address molecular cooling in our next work on this topic.

3.1.2 Adaptive Mesh Refinement Control

Throughout the simulation, the AMR resolution was dynamically and adaptively adjusted to resolve the structures of interest. The refinement level ℓ of AMR blocks relates the size of the computational box L to size of an individual AMR grid cell by $\Delta x = 2^{-\ell+1-3}L$,

where the factor of 2^{-3} arises from the subdivision of AMR blocks into 8 cells along each axis ($8^3 = 512$ cells per block). During the initial gravitational collapse of dark matter and gas leading to the formation of a minihalo we refined based on the gas density ρ . Specifically we raised the refinement to level ℓ to satisfy the condition $\rho < 3\bar{\rho}2^{3(1+\phi)(\ell-\ell_{base})}$, where $\ell_{base} = 5$ is the initial refinement level at the start of the simulation, $\bar{\rho}$ is the mean density in the box, and $\phi = -0.3$ (see, e.g., Safronek-Shrader et al., 2012, and references therein). After the insertion of a star particle, which takes place in the most massive dark matter minihalo in the box, we discontinued enforcing density-based refinement in other halos. At the evolving location of the star particle we maintained the maximum refinement level attained when refining based on gas density even after the H II region broke out and gas density dropped.

In order to resolve the free expansion phase of a supernova remnant, it is necessary to resolve scales much smaller than the radius at which the expanding blast wave sweeps up a gas mass similar to the ejecta mass. The grid resolution at each supernova insertion was forced to be ≤ 0.03 pc and somewhat coarser for the later supernovae in 7SN that explode in the bubble containing gas shocked by early supernovae. We additionally refined the grid up to the maximum resolution anywhere in the box using the standard second-derivative refinement criterion in FLASH tuned to aggressively refine ahead of compositional discontinuities where metallicity jumps. This ensured that the forward shock wave, contact discontinuity, and reverse shock were maintained at the highest available grid refinement level. As each remnant expanded, we degraded the resolution while ensuring that the diameter of the remnant (or superbubble) was resolved by at least 256 cells. In the late stages of the simulations focused on the recollapse in the halo, we degraded the resolution in regions causally disconnected from the halo center, outside the virial radius of the halo.

In all supernovae we assumed that 10% of the ejecta mass was in metals, with α -enhanced solar abundances ($[\alpha/\text{Fe}] = 0.5$). In the thermodynamic calculations (but not in tracking metal dispersal in 1SN), we assumed that the metal abundances were homogeneous within each supernova's ejecta. The tracking of ejecta was carried out with Lagrangian passive tracer particles, $N_{trace} = 10^7$ in 1SN and $(2-3) \times 10^6$ per supernova or a total of $N_{trace} \approx 2 \times 10^7$ in 7SN. The tracers allowed us to connect ejecta fluid elements to their origin in the explosions. In 1SN they allowed us to distinguish between the ejecta originating in distinct mass shells within the explosion, and in 7SN between the ejecta originating in different supernovae. It is worth noting that the numerical limitations affecting tracers, e.g., associated with the finiteness of the order of the velocity field representation on the

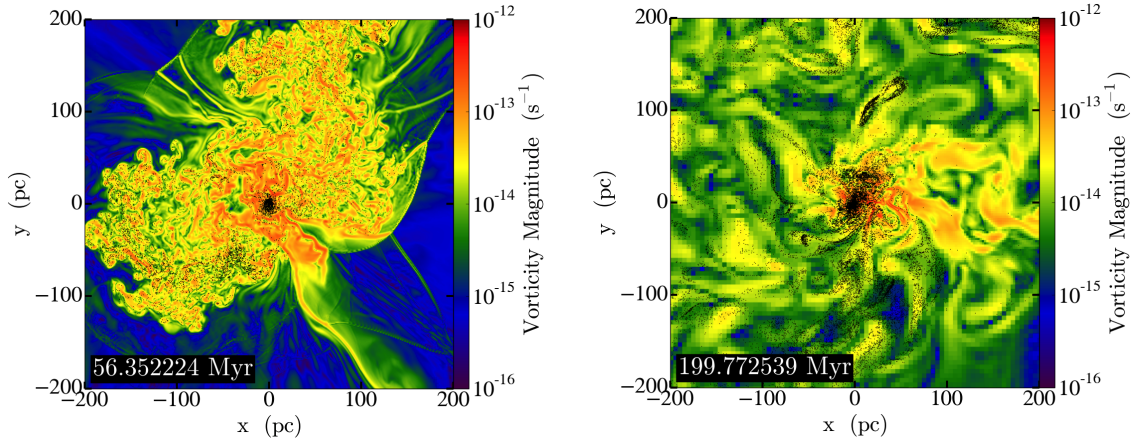


Figure 3.2: A slice of vorticity magnitude $|\nabla \times \mathbf{v}|$ in the center of 1SN (left) and 7SN (right) overplotting ejecta tracer particles in a 5pc thick slab containing the slice (black dots). Note that metal ejecta are unmixed outside the central high-vorticity core, tens of parsecs in radius.

computational mesh, are distinct from the numerical teleportation problem mentioned in Section 3.1.1. Thus, the simulated metallicity is generally to be trusted in cells in which the Eulerian and Lagrangian tracers indicate consistent values of the metallicity.

3.2 Hydrodynamic Evolution

The supernova remnants evolved through the free expansion, Sedov-Taylor, pressure-driven and momentum-conserving snowplow phases, and eventually, underwent partial collapse along the direction of the cosmic gas inflow, parallel to the filaments of the cosmic web. In 7SN, the later exploding supernovae expanded in the hot, low-density bubble evacuated by earlier ones, with blast waves colliding with the dense radiative shell before the reverse shocks have completed traversal of the ejecta.

For the hydrodynamic and chemical evolution of the entire remnant or bubble, it is important that the photoionization by the supernova progenitor stars did not completely photoevaporate the densest primordial clouds inside the halo (Abel, Wise & Bryan, 2007; Bland-Hawthorn, Sutherland & Karlsson, 2011; Ritter et al., 2012). While the photoevaporation flows are difficult to adequately resolve in cosmological simulations, survival of neutral clouds inside the primordial HII region is expected from the analytical evaporation solutions of Bertoldi & McKee (1990). The densest clouds with central densities

$n \lesssim 10 \text{ cm}^{-3}$ and distances $\sim 50\text{--}100 \text{ pc}$ from the center of the halo are associated with the filamentary inflow from the cosmic web. Supernova blast waves swept past these clouds, partially ablating them and depositing some ejecta material at the perimeters of the clouds. The blast wave-cloud interaction drove turbulence inside the bubble. The ablated primordial gas found itself inside the hot, turbulent interior, where it appeared to be susceptible to turbulent-stirring-aided mixing, especially in the multi-supernova simulation. This intra-bubble mixing resulted in a modest, factor of $\lesssim 10$ dilution of the ejecta by the primordial gas.

After ~ 0.13 and $\sim 1 \text{ Myr}$ from the (first) explosion in simulation 1SN and 7SN, respectively, the ejecta material started to accumulate in the pressure-driven snowplow shell. The shell was thin $< 10 \text{ pc}$ and not adequately resolved at grid resolution $\sim 0.5\text{--}1 \text{ pc}$. The insufficient resolution blurred the contact discontinuity and its associated compositional gradient. As a result, the metallicity derived from the passive mass scalar was diluted to $Z \sim 10^{-4}\text{--}10^{-3}$ in the thin shell. Rayleigh-Taylor (RT) fingers first became prominent in the shell after $\sim 3 \text{ Myr}$ and then became extended, with length scales comparable to the radius of the bubble, at $\sim 20 \text{ Myr}$. The long-term hydrodynamical evolution of the supernova bubble was highly anisotropic, with a fraction of the ejecta and swept-up primordial medium traveling many halo virial radii perpendicular to the cosmic web filaments, and another $\sim 50\%$ of the ejecta remaining within the virial radius.⁵

After the supernova bubbles started to collapse, the bubble interiors cooled to $\sim 10^4 \text{ K}$ and began intermixing with the ambient unshocked gas. Dual inflows fed toward the halo center: from the infall of unenriched, primordial clouds (including from merging halos in 7SN), and from the fragments of the buckling thin shell. The terminus of the inflows was a turbulent quasi-virialized (or quasi-hydrostatic) cloud in which turbulence was stirred by gravitational infall. Figure 3.1 illustrates the overall geometry of the metal distribution at this stage. It shows a homogenized low-metallicity interior surrounded by more metal rich, inhomogeneous clouds.

Figure 3.2, plotting the amplitude of the fluid vorticity, shows that vortical time scales in the quasi-virialized cloud are $|\nabla \times \mathbf{v}|^{-1} \sim 0.1\text{--}1 \text{ Myr}$, short enough to facilitate turbulent-cascade-aided fluid mixing in $\sim 10 \text{ Myr}$. Vorticity is the highest near the center of each plot, where the metal-enriched gas has gone into runaway gravitational collapse. We expect the collapse to ultimately lead to the formation of second-generation stars. Outside the

⁵The morphological evolution of the metal-enriched volume bears similarities to both the centered and off-center idealized non-cosmological simulations of Webster, Sutherland & Bland-Hawthorn (2014).

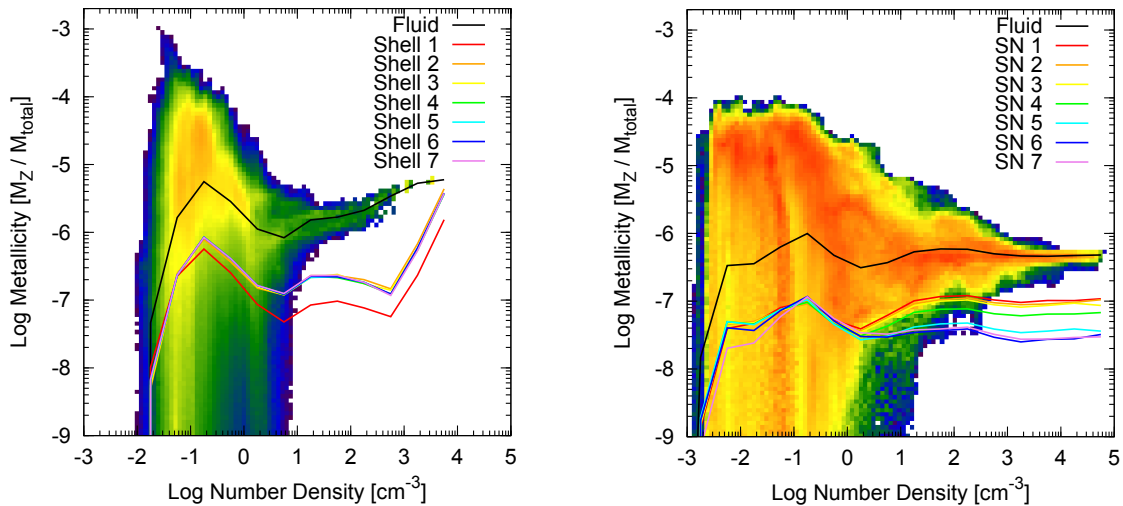


Figure 3.3: Metallicity as a function of gas density at the end of the simulation 1SN at 56 Myr after the first explosion (left plot) and 7SN at 200 Myr after the first explosion (right plot). From red to blue, the color scales with the logarithm of the fluid mass in the density and metallicity bin. Solid curve is the mean metallicity and colored curves are the fractional contributions from the seven radial mass bins (1SN) and seven supernovae (7SN).

quasi-virialized cloud, the vortical time scales are longer, 10–100 Myr, precluding mixing. Figure 3.3 shows the joint distribution of gas density and metallicity in the two simulations. Metallicity spread in low-density gas is high, indicating a high degree of inhomogeneity. The spread decreases with increasing density, becoming narrow for $n \gtrsim 10\text{--}100\text{ cm}^{-3}$. The narrowing of the metallicity spread is a consequence of rapid turbulent homogenization. The densest gas has negligible metallicity spread with $Z \approx 5 \times 10^{-6}$ in 1SN and 5×10^{-7} in 7SN. We can conclude that the very first generation of metal-enriched stars will be chemically homogeneous on the scale of a stellar group or cluster. Recently, Feng & Krumholz (2014) observed the same in simulations of star clusters forming in a very different environment, the Milky Way disk (see, also, Bland-Hawthorn et al., 2010). We shall see in the following section, however, that stellar abundance patterns in the first metal-enriched star forming systems will not be simple superpositions of the yield patterns of the contributing supernovae.

3.3 Monolithic and Biased Enrichment

We proceed to analyze how hydrodynamic dispersal depends on the nucleosynthetic site. In analyzing simulation 1SN, we split the ejecta at supernova insertion into $N_{bin} = 7$ radial bins containing equal ejecta masses and treat the bin index $i = 1, \dots, N_{bin}$ as a crude proxy for the isotopic group synthesized in the corresponding bin. For example, the innermost bins could contain the explosively synthesized Fe peak and α elements, the intermediate bins could be rich in light hydrostatic elements (C and O), and the outermost bins would contain H and He. This idealizes the explosion as preserving spherical symmetry, which is certainly not the case, as symmetry is strongly broken by convection preceding and during the collapse and by RT fingering during the explosion (our simulations can capture the RT instability in the remnant but not in the explosion). However, we expect that the radial “dredging” of elements by instabilities (and rotation-driven mixing, see, e.g., Maeder & Meynet, 2012) is incomplete and that some radial stratification is preserved until the ejecta enter free expansion. In analyzing simulation 7SN, we ignore the stratification inside each explosion and take the bin index $i = 1, \dots, N_{bin}$ to range over the $N_{bin} = N_{SN} = 7$ supernovae.

We first examine the degree to which the ejecta in different bins are stirred with each other. In 1SN, the outer, high-velocity mass shells of the ejecta are well-stirred between themselves, but inner mass shells remain highly inhomogeneous. In 7SN, the ejecta from supernovae separated by short time intervals are well-stirred with each other. The ejecta from later supernovae, separated from the earlier supernovae by the longest time intervals, remain inhomogeneous.

We call the enrichment by the source (a single supernova in 1SN and a cluster of supernovae in 7SN) *monolithic* if the density of isotope A at location \mathbf{x} is proportional to the sum of the isotopic yields of individual bins $Y_{i,A}$ over the bin index. Specifically,

$$\rho_A(\mathbf{x}) = Z(\mathbf{x})\rho(\mathbf{x}) \frac{Y_A}{\sum_A Y_A}, \quad (\text{monolithic}), \quad (3.1)$$

where

$$Y_A \equiv \sum_{i=1}^{N_{bin}} Y_{i,A} \quad (3.2)$$

and $\rho(\mathbf{x})$ and $Z(\mathbf{x})$ are the total mass density and total metallicity from the enrichment event, respectively, such that $\int Z\rho d^3x = \sum_A Y_A$. It is standard to assume (e.g., Ting et al., 2012) that enrichment is indeed monolithic so that each enrichment event \mathcal{E} defines a unique chemical

space vector $\mathbf{Y}^{(\mathcal{E})} \equiv (Y_{A_1}^{(\mathcal{E})}, Y_{A_2}^{(\mathcal{E})}, \dots) \sim \mathbf{Y}^{(\mathcal{C})}$ representative of a class \mathcal{C} of nucleosynthetic sources (e.g., core collapse events with or without r-process).

If star formation takes place at space-time points (\mathbf{x}_k, t_k) , then stellar abundances are given by⁶

$$Z_{k,A} = \frac{1}{\rho(\mathbf{x}_k, t_k)} \sum_{\mathcal{E}} \rho_A^{(\mathcal{E})}(\mathbf{x}_k, t_k), \quad 1 \leq k \leq N_{star} \quad (3.3)$$

The goal of chemical abundance analysis is then to isolate nucleosynthetic source classes by recovering their yield vectors $\mathbf{Y}^{(\mathcal{C})}$ from stellar abundance data $Z_{k,A}$. The dimensionality of the chemical abundance space corresponds to the number of different nucleosynthetic classes.

The metallicities resulting from individual events $Z^{(\mathcal{E})}(\mathbf{x}, t)$ are random variables determined by the hydrodynamics of metal dispersal. They endow stellar metallicities with scatter. If a sufficient number of events contributes and the events are statistically independent, the central limit theorem implies that the scatter is Gaussian, justifying the PCA approach.

It cannot be taken for granted, however, that the source contributions are monolithic (Eqn. 3.1), because nucleosynthetic products are injected into the hydrodynamic environment with different velocities and at different times and are transported differently to their star formation sites. In perfect generality, for each nucleosynthetic event,

$$\begin{aligned} \rho_A(\mathbf{x}) &= \frac{\sum_{i=1}^{N_{bin}} Z_i(\mathbf{x}) \rho(\mathbf{x}) \frac{Y_{i,A}}{\sum_A Y_{i,A}}}{\sum_A Y_A} \\ &= Z(\mathbf{x}) \rho(\mathbf{x}) \frac{\sum_{i=1}^{N_{bin}} w_i(\mathbf{x}) Y_{i,A}}{\sum_A Y_A}, \end{aligned} \quad (3.4)$$

where $Z_i(\mathbf{x})$ is the total metallicity at \mathbf{x} due to enrichment by bin i such that $\int Z_i \rho d^3x = \sum_A Y_{i,A}$, and in the second line, we introduced the weights

$$w_i(\mathbf{x}) = \frac{Z_i(\mathbf{x})}{Z(\mathbf{x})} \frac{\sum_A Y_A}{\sum_A Y_{i,A}} \quad (3.5)$$

for straightforward comparison with the monolithic case (Eq. 3.1).

If source contributions are monolithic then $w_i \equiv 1/N_{bin}$, but in general, the enrichment at a specific location could be biased toward some bins, giving them higher weights. The dimensionality of the chemical abundance space can now be much larger than the number

⁶Here and in what follows, coarse graining of ρ_A on the spatial scales of star-forming clumps is implied.

of nucleosynthetic source classes. The weights encapsulate the biases that hydrodynamics introduces into abundance patterns. If the weights are completely random and possess unknown statistics, this introduces uncontrolled biases frustrating the recovery of nucleosynthetic source classes from stellar abundance data. Here, we make the first step toward characterizing the nature of the biases, aspiring to detect regularities that can be factored into chemical abundance analysis. Figure 3.3 shows bin-specific metallicities Z_i spherically averaged around the center of gravitational collapse. In both simulations, in dense gas $n \gtrsim 1 \text{ cm}^{-3}$, departures from monolithic enrichment are evident. In 1SN, the innermost radial bin, which is expected to carry explosive elements, is deficient by a factor of ~ 3 relative to the other bins, $\langle w_1 \rangle \sim \frac{1}{3} \langle w_2 \rangle$ and $\langle w_2 \rangle \sim \dots \sim \langle w_7 \rangle$, where the averages refer to gas-mass-weighted averages of w_i in the dense gas. In 7SN, ejecta from the first two supernovae are ~ 3 times as abundant as the ejecta from the last two supernovae, $\langle w_1 \rangle \sim \langle w_2 \rangle \sim 3 \langle w_6 \rangle \sim 3 \langle w_7 \rangle$.

We propose the following physical interpretation. In the case of the solitary supernova, the reverse shock raises the inner ejecta shells, which it sweeps later and at lower densities, to a higher entropy than the outer shells, which it sweeps earlier and at higher densities. This can be seen by considering the Sedov-Taylor point explosion, in which the pressure asymptotes to a constant value near the center, but density decreases toward the center as $\rho \propto r^{3/(\gamma-1)}$. Therefore, with $\gamma = 5/3$, the entropy $s = \ln(P/\rho^\gamma) + \text{const}$ rises toward the center of the ejecta as $s \sim -\frac{27}{10} \ln r + \text{const}$. This is significant because as the ejecta become quasi-isobaric inside the remnant, the radiative cooling time is a steeply increasing function of entropy. The outer ejecta shells cool first and are incorporated into the snowplow shell, while the innermost ejecta avoid cooling. As the remnant stalls and collapses, the innermost ejecta, having higher entropy, are outward buoyant and rise to larger radii, thus avoiding collapse and allowing low-entropy outer ejecta mass shells to fall in to enrich the quasi-virialized cloud. In 1SN, the ejecta tracer particle radii containing 25% of the ejecta in bins 1 (the innermost bin) and 2 cross at $\sim 0.2 \text{ Myr}$ after the explosion and then bin 1 interchanges with bins ≥ 3 at $\sim 0.3 \text{ Myr}$.

In the case of clustered supernovae, the situation is similar, but now since the density inside the supernova bubble keeps dropping as the bubble expands, the ejecta from later supernovae are on average raised to higher entropies than those of earlier ones and are less susceptible to cooling. Since the ejecta of the latest supernovae remain hot, they are outward buoyant. Upon the collapse of the bubble, the hot ejecta of the later supernovae interchange with the cooled ejecta of the earlier supernovae. The latter fall in to enrich the

central cloud.

3.4 Confronting the Empirical Record

Our results have important implications for understanding the early stages of cosmic chemical evolution. More precisely, the hydrodynamic biases in the transport of individual elements, introduced by the post-explosion evolution, need to be taken into account when confronting the empirical abundance trends. The ultimate goal here is to achieve a robust mapping from the observed abundance pattern in metal-poor stars or systems thereof to the individual sources of those metals. In the absence of any monolithic mapping between sources and fossil record (see Section 4), the hydrodynamic transport process constitutes the missing link in our current understanding. Simulations along the lines of our exploratory work here promise to bridge this crucial gap. However, we can already now address a long-standing problem in Galactic chemical evolution in a new light. This concerns the prevalence of peculiar abundance ratios in low-metallicity stars and systems.

To briefly summarize the main phenomenology, observations of metal-poor stars in the Galactic halo, assembled over more than two decades, have provided intriguing constraints on the nature of early chemical evolution (reviewed in Beers & Christlieb, 2005; Frebel & Norris, 2013a; Karlsson, Bromm & Bland-Hawthorn, 2013). The current state of the art is defined by a large sample of halo red giant stars, where key lines are sufficiently strong to enable high signal-to-noise spectroscopy (Cayrel et al., 2004; François et al., 2007). The main lessons are two-fold: both α -elements (Mg, Ca, Si, Ti), and iron-peak elements (V to Zn) exhibit extremely small scatter, down to $[\text{Fe}/\text{H}] \sim -3.5$. The neutron-capture elements, comprising elements beyond Zn, on the other hand, exhibit equally small scatter down to $[\text{Fe}/\text{H}] \sim -3$, but show extremely large scatter, up to 5 dex, below this (Qian & Wasserburg, 2002; Truran et al., 2002; Sneden, Cowan & Gallino, 2008). Finally, the lighter elements (C, N, O) again show large abundance variations at $[\text{Fe}/\text{H}] < -4$, and approach well-defined trends for less metal-poor stars.⁷ The most dramatic manifestation of this transition to well-behaved abundance trends, once a threshold metallicity is reached, is provided by the huge scatter in r-process abundances, seen in Galactic halo stars with $[\text{Fe}/\text{H}] \lesssim -3$ (reviewed in Sneden, Cowan & Gallino, 2008). The origin of r-process nucleosynthesis, such as the

⁷The skewing of abundance patterns by post-supernova hydrodynamics may also be the explanation of abundance anomalies (e.g., Feltzing et al., 2009; Cohen et al., 2013; Yong et al., 2013b) found in primitive stellar systems in the local universe.

mass and properties of the supernova progenitor star, is still highly uncertain. There is, however, tentative evidence that the r-process might operate in progenitor stars with a very narrow mass range, possibly close to the lower-mass limit for core-collapse supernovae (e.g., Qian & Wasserburg, 2008).

It has been challenging to explain all of these trends within one comprehensive framework, but our work suggests a promising *Ansatz* to do so. Basically, our results show that early enrichment is differential, non-monolithic in nature. This specifically implies that second-generation star formation does not sample the enrichment from the full IMF, and possibly not even that from a single explosion (see Fig. 3). Our simulations build on earlier analytical work that had postulated a minimum number of supernovae, $N_{SN} \gtrsim 20$, needed to average out any yield inhomogeneity from individual explosion sites (see, e.g., Tsujimoto & Shigeyama, 1998; Tsujimoto, Shigeyama & Yoshii, 1999). This absence of effective source-averaging, then, such that only a small number of explosion sites contribute, is the key requirement to preserve peculiar abundance ratios. Next to the classical r-process elements, a similar explanation may pertain to the strong odd-even pattern that is predicted for pair-instability supernova enrichment, but has not been detected so far (Heger & Woosley, 2002; Karlsson, Johnson & Bromm, 2008). We note that our explanation of the r-process record, understanding huge scatter as a result of sparse IMF-sampling, where only a very narrow progenitor mass range gives rise to the r-process, does not require any stochastic contribution from neutron star mergers, as has recently been suggested (Shen et al., 2015; van de Voort et al., 2015).

Once cosmological structure formation advances to more massive systems, with deeper potential wells to facilitate the near-uniform mixing of the ejecta from a large number of supernovae, convergence towards well-defined, smooth abundance trends will set in. Extragalactic observations targeting systems of greatly different virial mass are in agreement with this overall picture. Specifically, recent medium- and high-resolution spectroscopy of red giant stars in Milky Way dwarf satellites has established that their abundance properties, including the degree of scatter, are indistinguishable from the metal-poor tail of the Galactic halo stars (Frebel et al., 2010; Frebel, Simon & Kirby, 2014). A complementary view into early metal enrichment is provided by the abundances measured in damped Lyman- α (DLA) systems. Here, the evidence points towards extremely low scatter, at least for the prominent α -elements (Cooke et al., 2011; Becker et al., 2012). This may be indicative of the onset of efficient gas-phase mixing in the deep potential wells of the DLA dark matter host halos. An intriguing question for future simulation work is to test whether

the empirical threshold metallicity, roughly measured by $[\text{Fe}/\text{H}]$, for the disappearance of such anomalous abundance signatures can be reproduced.

Of special interest is the observed dichotomy of carbon-enhanced and carbon-normal metal-poor stars (e.g., Beers & Christlieb, 2005; Gilmore et al., 2013). Cooke, Pettini & Jorgenson (2015, hereafter CM14) have recently suggested that the strength of supernova driven outflows may be responsible for this bimodality. These authors invoke two classes of supernovae with greatly different times for recovery from the supernova explosions with different explosion energies. More energetic explosions $E_{\text{SN}} \gg 10^{51}$ erg imply longer recovery times (Jeon et al., 2014). According to CM14, rapid recovery is connected to weak explosions with large carbon overabundances, and slow recovery with strong explosions with normal carbon yields. Our simulation 1SN, where we find the return of supernova ejecta into the halo center deficient in the ejecta originating from the innermost 10% of the ejecta, suggests another mechanism for carbon-enhanced metal poor (CEMP) stars. A core-collapse explosion ejects a normal carbon-to-iron ratio $[\text{C}/\text{Fe}] < 1$, but the iron-bearing ejecta are raised to a higher entropy upon reverse shock traversal than the carbon-bearing ejecta, and subsequently do not cool and settle into the halo center to form second-generation stars.

3.5 Summary and Conclusions

We have carried out two complementary very-high-resolution cosmological simulations of how the metals produced in the first supernova explosions are transported into the cold, dense gas out of which the second-generation of (Population II) stars is formed. The first simulation followed the ejecta from a single explosion, whereas the second traced the metal dispersal from seven sources. We arrived at two main conclusions. The re-condensed Population II star forming material exhibits strong turbulent vorticity, implying a likely fine-grained turbulent mixing of gas down to very small, unresolved, scales. Stellar clusters or groups forming out of this material are thus predicted to be chemically uniform, unless any self-enrichment process may operate during the later stages of stellar evolution. Our results also indicate that the hydrodynamic metal transport proceeds differentially, such that the monolithic mapping of source abundances into the fossil record is broken.

The hydrodynamically biased nature of early metal enrichment, as demonstrated in our pathfinder simulations, has multiple implications, requiring that we rethink a number of

our traditional assumptions and methodologies. On the theory side, a common approach to chemical enrichment is to assume that homogenization of the chemical composition is instantaneous and complete in certain “mixing volumes,” normally centered on nucleosynthetic sources, but that the volumes themselves occur stochastically and intermittently, tracing star formation. This approach provides a rudimentary model of inhomogeneous chemical evolution, but since the choice of mixing volumes is ad hoc, its predictive power is limited. It is standard to motivate the choice of mixing volumes by considering the spatial extent of supernova remnants and galactic superbubbles, assuming that the medium is chemically homogeneous within these structures (Argast et al., 2000; Oey, 2000, 2003; Karlsson, 2005; Karlsson & Gustafsson, 2005; Karlsson, Johnson & Bromm, 2008; Bland-Hawthorn et al., 2010; Corlies et al., 2013). In the absence of monolithic source mapping, it is not obvious how to adjust this technique.

Our results also present a challenge to the standard interpretational framework of near-field cosmology. The hydrodynamic biases need to be quantified as a function of the star forming environment by carrying out a dedicated program of simulations. Once these chemical transport ‘maps’ are in hand, the full power of stellar archaeology can be unleashed. Such a program is very timely, given the advent of large survey projects, including the dedicated efforts connected to Gaia-ESO, which promise a record of early chemical evolution in unprecedented detail.

Chapter Four: Toward *ab initio* extremely metal poor stars¹

Understanding how the first generations of stars ended the cosmic dark ages is a key frontier in modern astrophysics and cosmology (for reviews, see Fan, Carilli & Keating, 2006; Furlanetto, Oh & Briggs, 2006; Morales & Wyithe, 2010; Bromm & Yoshida, 2011; Pritchard & Loeb, 2012; Bromm, 2013). Of particular interest are the initial steps in cosmic chemical evolution starting from an essentially pure hydrogen and helium Universe (Karlsson, Bromm & Bland-Hawthorn, 2013). How did the first stars, the so-called Population III (Pop III), enrich the early Universe with the first heavy elements? Elucidating early star formation and metal enrichment is crucial for connecting the fossil record preserved in the Galactic metal-poor stars and the ancient dwarf galaxies in the Local Group to their formation sites at high redshifts (for review, see Frebel & Norris, 2015, and references therein).

There is an ongoing debate concerning the physics responsible for the transition from the top-heavy initial mass function (IMF) predicted for metal-free Pop III stars (see Stacy, Bromm & Lee, 2016, and references therein) to the low-mass-dominated IMF observed in metal-poor Pop II and chemically mature Pop I stars (Chabrier, 2003). What are the respective roles of metal fine structure line and dust grain cooling channels? The metal line cooling dominates thermal evolution at intermediate densities, too low to facilitate fragmentation of gas into low mass stars. Dust cooling can allow fragmentation into low mass stars, but only if grains are abundant at these low metallicities—a theoretically uncertain proposition. The debate centers on the specific roles of metal line and dust cooling (for review, see, e.g., Milosavljević & Safranek-Shrader, 2016). Does metal line cooling affect the final, high-density outcome of the fragmentation process? If it does, we expect to detect its influence at a minimum ‘critical metallicity’, which for fine structure carbon and oxygen line cooling is $Z_{\text{crit,fs}} = 10^{-3.5} Z_{\odot}$ (Bromm et al., 2001; Bromm & Loeb, 2003b; Santoro & Shull, 2006; Smith et al., 2009). In comparison, the critical metallicity above which dust can explain the formation of the known metal-poor stars is $Z_{\text{crit,dust}} \sim 10^{-6} Z_{\odot}$, assuming a reference fraction of metal mass depleted in dust of $f_{\text{dust}} = 0.22 - 0.24$ (Schneider et al.,

¹This chapter was published as Ritter J. S., Safranek-Shrader C., Milosavljević M., Bromm V., 2016, MNRAS, 463, 3354, under the supervision of Miloš Milosavljević.

2006, 2012, see, also, Omukai, Hosokawa & Yoshida 2010; Ji, Frebel & Bromm 2014).² Observationally, there is a distinct lack of stars at metallicities $Z \lesssim 10^{-5} Z_{\odot}$, but a handful of stars, such as SDSS J102915+172927, with $Z = 10^{-4.35} Z_{\odot}$ (Caffau et al., 2011)³, have now been found that lie well below $Z_{\text{crit,fs}}$.

The character of the very first metal and dust pollution is of course contingent on the physics of the initially metal-free Pop III stars and their explosions. The principal model parameter is the Pop III stellar mass. Much effort is being put into attempts to constrain the statistics of this parameter with first-principles hydrodynamical simulations. Recent high-resolution simulations suggest that metal-free clumps in unpolluted cosmic minihalos fragment down to the protostellar mass scales of $\sim 1 - 10 M_{\odot}$ (Stacy, Greif & Bromm, 2010; Clark et al., 2011a; Greif et al., 2011, 2012). Accretion onto such protostars is eventually limited by radiative feedback (Hosokawa et al., 2011; Stacy, Greif & Bromm, 2012b; Stacy, Bromm & Lee, 2016). The resulting stars should have final masses on the order of a few tens of solar masses. These massive stars rapidly convert hydrogen and helium into heavier elements in just a few million years (Schaerer, 2002) and explode as core-collapse supernovae (Heger & Woosley, 2002).

The precise nucleosynthetic yields in the ejecta of core-collapse supernovae are not known from first principles, primarily because a theoretically uncertain fraction of the supernova yield ends up trapped in the compact remnant (Heger & Woosley, 2010). Three-dimensional simulations of the long-term evolution of core-collapse explosions indicate that the ejecta may be distributed anisotropically. The heavier elements (e.g., the iron group) that fall back onto the remnant in spherically-symmetric models are instead ejected in jets (Wongwathanarat, Müller & Janka, 2015). Intrinsic explosion anisotropy may imply some irreducible scatter in the heavier element abundances in enriched gas, even for similar mass supernova progenitors (Sluder et al., 2016).

These nonlinear effects can be so sensitive to the precise mass (and initial rotation) of the Pop III star that, in view of the theoretically uncertain Pop III IMF and rotational evolution (Stacy, Bromm & Loeb, 2011), it is currently not possible to reliably predict the metal and dust yields of Pop III stars or the corresponding explosion kinetic energies. Instead, attempts are being made to constrain the physics of Pop III star formation and evolution, and their metal enrichment, by surveying for chemically extreme low-mass stars,

²Omukai, Hosokawa & Yoshida (2010) reports a higher critical value $Z_{\text{crit,dust}} \sim 10^{-5} Z_{\odot}$ for $f_{\text{dust}} \sim 0.01$ metal-to-dust depletion fraction.

³For a fiducial solar metallicity of $Z_{\odot} = 0.0153$ (Caffau et al., 2011).

and then analyzing the abundance patterns in the most extreme ones that could have been enriched by *single* Pop III supernovae. For example, the absence of iron in the extremely metal poor Keller et al. (2014) star has been interpreted as evidence for pollution by a single, low-energy (kinetic energy $\sim 10^{51}$ erg), black-hole-producing Pop III supernova, with a stellar progenitor mass of $\sim 60M_{\odot}$ (see, e.g., Ishigaki et al., 2014; Kobayashi et al., 2014; Takahashi, Umeda & Yoshida, 2014; Chen et al., 2016). In contrast, an extremely metal poor star discovered in the Galactic bulge has been claimed to better fit a more energetic $\sim 10^{52}$ erg (‘hypernova’) explosion (Howes et al., 2015). Since dust is required for at least the final stage of gravitational fragmentation into low mass stars, there is a renewed push to study dust formation in Pop III supernovae (e.g., Cherchneff & Dwek, 2010; Chiaki et al., 2014, 2015; Marassi et al., 2014, 2015; Sarangi & Cherchneff, 2015).

To date there has not been a direct numerical hydrodynamical demonstration of the single-supernova-to-low-mass-star pathway. Can extremely metal-poor, low-mass stars really form in the aftermath of single Pop III supernovae? It is easy to see how the Universe may fail to realize this pathway: the recovery time for re-condensation of gas in the wake of supernovae may be so long that the typical metal-enriched stars are always polluted by multiple Pop III explosions occurring in neighboring halos that ultimately merge with each other (for inter-halo enrichment, see Smith et al., 2015b). The enrichment by multiple Pop III supernovae could also be the predominant scenario if metals are so efficiently ejected from the host halos that a single halo must proceed through a sequence of Pop III-type explosions. At the other end of the range of possibilities, the typical single Pop III could disperse its metals so compactly, with minimum dilution, as to immediately produce stars much more metal rich than the observed extremely metal poor stars. Thanks to its complexity, the recycling of Pop III ejecta into the first metal-enriched stars remains an active research area (e.g., Whalen et al., 2008a; Ritter et al., 2012, 2015; Cooke & Madau, 2014; Jeon et al., 2014; Sluder et al., 2016).

Here, we attempt such a demonstration of the path toward star formation enriched by a single, low-energy Pop III supernova. We present an *ab initio* cosmological hydrodynamical simulation involving a single Pop III supernova with a low explosion energy of 10^{51} erg, proceeding until a metal-enriched pre-stellar core has formed in the cosmological box and the conditions imply imminent fragmentation into low-mass stars. The simulation is a test of the single-supernova enrichment hypothesis for stars like that of Keller et al. (2014). It also helps us understand precisely *how* a smattering of Pop III ejecta gets combined with a much larger mass of metal-free gas, something that must happen if the system

is to produce an extremely metal poor pre-stellar clump. The simulation enables us to ask, on what initial orbits in the host dark matter halo do the first metal-enriched stars form? The orbital extent could be related to the half-light radii of the ultra faint dwarf (UFD) galaxies. The simulation substantially improves upon the idealized precursor simulations we reported in Ritter et al. (2012) and Sluder et al. (2016). It is the logical next step toward providing an end-to-end proof-of-concept for extremely metal poor star formation in the first metal-enriched cosmic objects.

This chapter is organized as follows. In Section 4.1 we describe our numerical methodology and emphasize the novel elements introduced in this work. In Section 4.2 we provide a descriptive account of the progression from a Pop III supernova to a metal-enriched pre-stellar clump. We also offer our interpretation of how the clump acquired its extremely low metallicity. In Section 4.3 we analyze our results and discuss the implications for interpreting extremely metal poor star discoveries and for explaining the kinematic structure of UFDs. Finally, in Section 4.4 we summarize our main conclusions.

4.1 Numerical methodology

The initial setup of the simulation was the same as in Ritter et al. (2012, 2015). We ran the adaptive mesh refinement (AMR) hydrodynamics code FLASH (Fryxell et al., 2000) with the multigrid Poisson solver of Ricker (2008) and dark matter particle smoothing and time-integration as in Safranek-Shrader et al. (2012) and Ritter et al. (2012). The 1 Mpc comoving cosmological box was initialized at redshift $z = 145$ with nested Gaussian density fluctuations generated with the package GRAFIC2 (Bertschinger, 2001) using the *Wilkinson Microwave Anisotropy Probe 7-year* cosmological parameters (Komatsu et al., 2011). The dark matter particle mass in the highest refined patch, where the gas would first collapse to high densities, was $M_{\text{DM}} = 230 M_{\odot}$, and the effective grid resolution (relative to the whole box at initialization) was 512^3 .

During the first, metal-free phase of the simulation, we tracked the formation of the principal coolant, the H_2 molecule, by integrating the standard ionic and molecular non-equilibrium chemical network (see, e.g., Safranek-Shrader, Bromm & Milosavljević, 2010). At low densities and temperatures, we computed the cooling rate following the recommendation of Glover & Abel (2008). The metal-free phase lasted until a dark matter halo with a mass $\sim 10^6 M_{\odot}$ and radius ~ 175 pc virialized at redshift $z = 19.5$ and the H_2 -cooled,

metal-free gas in the halo had collapsed to density $n_{\text{H}} > 10^3 \text{ cm}^{-3}$. We interpreted this as heralding the imminent formation of the very first, metal-free star. We replaced $60 M_{\odot}$ of gas around the density maximum with an ‘active’ (gravitating) Pop III star particle. This replacement capped the gas density around the maximum, where the star particle was inserted, at a ceiling computed consistent with mass conservation.

We ray-traced ionizing radiation from the star particle to compute the dynamical expansion of the HII region over the star’s lifetime of 3.5 Myr. The ionization state and temperature along each separate ray in the HII region interior were evaluated by interpolating from values pre-computed with the code CLOUDY (Ferland et al., 2013) for a stellar surface blackbody spectrum with an effective temperature of $T_{\text{eff}} = 10^{4.94} \text{ K}$ (Schaerer, 2002). We tabulated the pre-computed data as a function of the photoionization parameter $\xi = F/n$, where F is the local, optical-depth-attenuated flux (see Ritter et al., 2012, 2015). For the ray-tracing calculation, we carried out finite volume mapping of the Cartesian AMR mesh onto a spherical mesh defined by the HEALPIX scheme (Górski et al., 2005) partitioning the angular space into 3000 equal solid angle conical pixels and 100 logarithmically spaced radial bins. The stellar source emitted $Q = 4.795 \times 10^{49}$ ionizing photons per second, the expected stellar lifetime-average ionizing photon emission rate for a $60 M_{\odot}$ star (Schaerer, 2002). The local ionizing flux in bin b at distance r from the source was $F_b = (Q - \sum_{i \leq b} V_i \alpha(T_i) n_i^2) / 4\pi r^2$, where $\alpha(T_i)$ is the temperature-dependent recombination rate and the sum is over all bins i between bin b and the ionizing source. For each grid cell c that maps to conical radial bin b we calculated the photo-ionization parameter $\xi_c = F_b/n_c$ and then linearly interpolated the tabulated solutions to update the temperature and ionization state in the cell.

When the star reached the end of its life we zoomed the mesh refinement to high resolution, from $\Delta x = 0.7 \text{ pc}$ during the stellar lifetime to a minimum cell width of $\Delta x_{\text{min}} = 0.02 \text{ pc}$, and inserted a supernova blast wave carrying 10^{51} erg of kinetic energy. The high spatial resolution was necessary to properly capture the reverse shock and avoid the notorious overcooling in under-resolved simulations (see, e.g., the analysis in Agertz et al., 2013). Extrapolating from the model computations of Heger & Woosley (2002), we assumed that a $35 M_{\odot}$ compact remnant was left behind and $25 M_{\odot}$ of ejecta was launched outward in spherically symmetric fashion. For this simulation we assumed that metals in the ejecta accounted for 10% (or $6 M_{\odot}$) of the initial progenitor mass, which is 24% of the ejecta mass ($Z_{\text{SN}} = 12 Z_{\odot}$). The supernova remnant was inserted in the free-expansion phase by overwriting grid cells with a constant density, temperature, and metallicity within

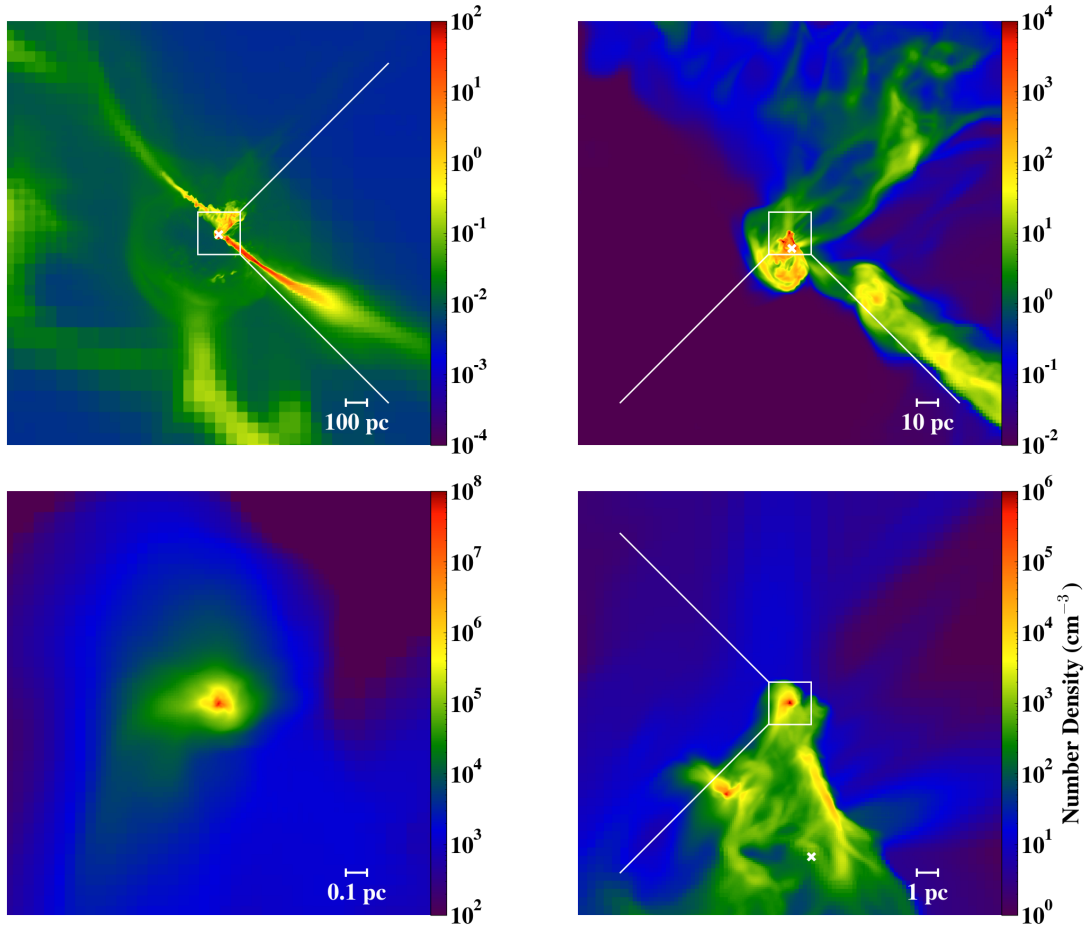


Figure 4.1: Number density projections (density-weighted, color scale showing $m_{\text{H}}^{-1} \int \rho^2 dz / \int \rho dz$) centered on the densest gas cell at the end of the simulation, 13.7 Myr after the explosion. The top-left panel shows the cosmic web filaments feeding into the halo center. The supernova ejecta bubble extends beyond the virial radius $r_{\text{vir}} = 175$ pc. The top-right panel shows that the dense neutral clouds that have survived photoionization are streaming into the halo center marked with a white “×”; the tip of a cosmic web filament is still a few dozen parsecs away. The bottom-right shows dense, self-gravitating clumps at the apocenter of an elliptical gas flow pattern. Each clump contains a few hundred solar masses of gas. The clumps loiter at density $n_{\text{H}} \sim 10^4 \text{ cm}^{-3}$ for several million years and then enter runaway collapse. The bottom-left panel shows the first runaway clump in which the collapse facilitated by metal line cooling rapidly increased the density above $n_{\text{H}} > 10^8 \text{ cm}^{-3}$.

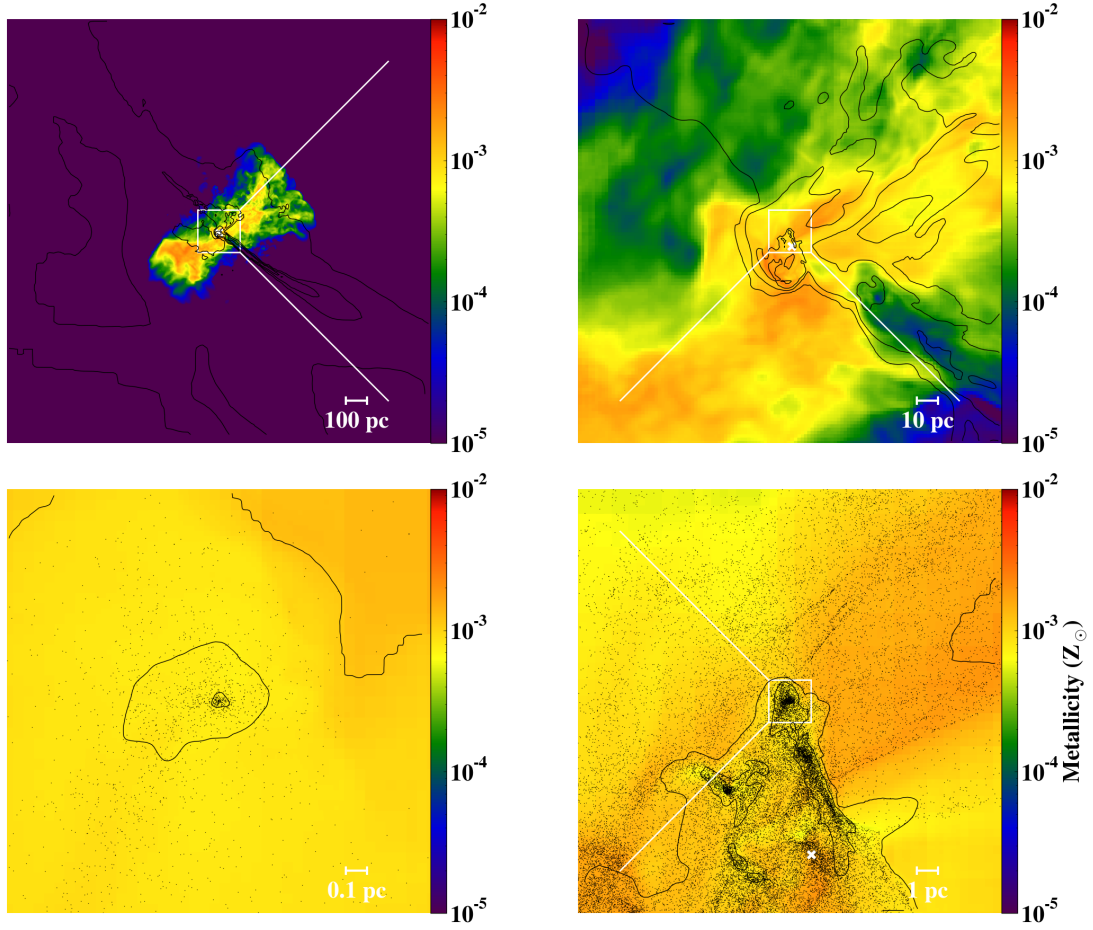


Figure 4.2: The same as Figure 4.1, but now showing metallicity projection (density-weighted, color showing $Z_{\odot}^{-1} \int Z_{\text{scal}} \rho dz / \int \rho dz$). Here we overplot density contours to provide context for the clumps and filament locations. In the bottom panels we also overplot metal tracer particles.

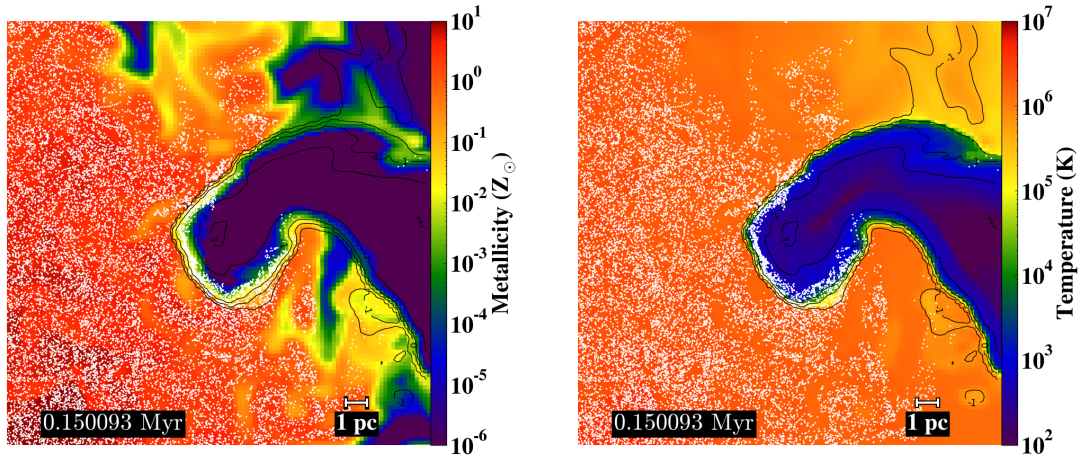


Figure 4.3: A slice through the cold cloud that would ultimately collapse and fragment into metal-enriched pre-stellar clumps showing passive scalar metallicity (left panel) and temperature (right panel) with gas density contours overplotted. Also overplotted are Lagrangian passive ejecta tracer particles (white dots) in a 1 pc thick slab containing the slice. Note the superficial enrichment of the cloud as well as evidence of numerical passive scalar diffusion where the scalar metallicity is $> 10^{-6} Z_{\odot}$ and yet no particles are present.

a radius of $R_{\text{SN}} = 0.6$ pc from the star particle. The velocity of ejecta was linear in radius $v(r) = v_{\text{max}} r/R_{\text{SN}}$ and $v_{\text{max}} = 2600 \text{ km s}^{-1}$. Ten million massless Lagrangian passive tracer particles were uniformly distributed in the ejecta to redundantly track their transport. The advantage of Lagrangian tracers is that they are not subject to the same numerical diffusion in moving compositional discontinuities that affects the transport of the passively advected scalar metallicity variable.

After supernova insertion, we evaluated the cooling rate and ionization state of gas by interpolating from a new set of CLOUDY tables, now as a function of density, temperature, and metallicity, but with no radiation field. The tables were pre-computed for a purely atomic gas containing C and O in addition to the primordial species with relative abundance $[\text{O}/\text{C}] = -0.4$. This value was chosen to be consistent with the abundances reported for carbon-enhanced metal-poor (CEMP) stars such as the star of Keller et al. (2014).⁴ Since H_2 cooling may still dominate at intermediate densities ($n_{\text{H}} \sim 100 \text{ cm}^{-3}$) and low metallicities ($Z \lesssim 10^{-2} Z_{\odot}$) (Glover & Clark, 2014; Safranek-Shrader, Milosavljević & Bromm, 2014b), we included additional cooling due to H_2 following Glover &

⁴For the Keller et al. (2014) star, Bessell et al. (2015) report a measurement $[\text{O}/\text{C}] \approx 0$. We were not aware of this more oxygen rich measurement when designing our simulation.

Abel (2008) (assuming 3:1 ortho-to-para ratio). To avoid the costly integration of the H_2 rate equation, in the final stage of the simulation we fixed the molecular abundance to $n_{\text{H}_2} = 10^{-2} n_{\text{H}}$, a level consistent with detailed calculations of the Myr-time-scale H_2 abundance in recombining metal-poor flash-ionized regions (e.g., Shapiro & Kang, 1987; Kang & Shapiro, 1992; Nagakura & Omukai, 2005; Johnson & Bromm, 2006; Yoshida et al., 2007). The thermodynamic update of specific internal energy e was operator-split from the hydrodynamic update and was sub-cycled on sub-steps of a tenth of the equilibrium cooling timescale $t_{\text{eq}} = \min(\rho e / \Lambda_{\text{H}_2} n_{\text{H}} n_{\text{H}_2}, \rho e / \Lambda_{\text{Z}} n_{\text{H}} n_{\text{Z}})$.

We followed the blast wave for 13.7 Myr, at all times maintaining the volume affected by the blast wave at a maximum spatial resolution. The adaptive refinement level was set such that the diameter of the blast wave was always resolved by at least 128 grid cells and the entire region affected by the blast wave was fully contained within the highest-resolved AMR blocks. During the final phase, when gaseous gravitational collapse resumed in the dark matter halo, we further refined the grid around the densest gas clumps, this time ensuring that the gas Jeans length was always resolved by at least 32 cells.⁵ To reduce the computational cost, during the final phase we degraded the mesh resolution in cells far from the halo center where the loss of resolution could have no impact on the dynamics in the self-gravitating clumps of interest.

4.2 Results

Photoelectric heating from photoionization, which raised the gas temperature in the immediate vicinity of the Pop III star particle to $\sim 6 \times 10^4$ K, suddenly overpressured the ionized gas. This drove a relatively dense shell ($n_{\text{H}} \sim 100 \text{ cm}^{-3}$) to distances $\sim 40\text{--}50$ pc. The shell expanded isotropically except for in a few special directions in which there was the most pronounced inflow from the cosmic web. There, embedded within the shell, remained denser ($n_{\text{H}} \sim 10^3 \text{ cm}^{-3}$) *neutral* clumps—surviving fragments of the Pop III star’s birth cloud. The failure to photoionize some of the densest metal-free clouds outside the ionizing sources’ host halos was already seen in our previous published simulations (Ritter et al., 2012, 2015; Sluder et al., 2016); it had first been reported in the context of cosmic minihalos

⁵The requirement that the thermal Jeans length be resolved by a minimum number of mesh elements is derived heuristically, not from *ab initio* numerical analysis. The most careful analyses advise that the Jeans length should be resolved by at least 64 cells, more than we require (e.g., Latif et al., 2013; Meece, Smith & O’Shea, 2014).

by Abel, Wise & Bryan (2007). The failure to completely photoionize the densest clouds is also expected by scaling the most sophisticated analytical models of photoevaporating clouds (Bertoldi & McKee, 1990) to our metal-free, H_2 -cooled clouds. While the ionizing source was present, we did not compute H_2 cooling in the neutral clouds because molecules should have been wiped out by the strong local Lyman-Werner band H_2 -dissociating flux.

The 3.5 Myr-old HII region defined the hydrodynamic environment into which the supernova ejecta expanded upon insertion. The reverse shock in the ejecta separated from the contact discontinuity at ~ 2 kyr after insertion and reached the innermost ejecta after ~ 20 kyr. The forward shock became radiative and formed a snowplow shell at ~ 150 kyr. The blast wave partially ablated, but did not significantly disrupt the densest, persistently-neutral clouds at distances ~ 50 pc from the explosion. The cloud fragments are visible in projection in the top-right panel of Figure 4.1. By the end of the simulation, the snowplow shell, also visible in the panel, has expanded to ~ 0.5 kpc, over twice the virial radius of the halo. In the companion Figure 4.2, we show the corresponding distribution of metals (further discussed below).

Of particular interest is the interaction of the metal-bearing ejecta with the dense clouds, since, as we shall see, star formation can resume precisely when one such dense cloud falls toward the halo center. At the end of the radiative phase the largest cloud had a central density $> 10^3 \text{ cm}^{-3}$ and diameter ~ 2 pc (see Figure 4.3). By the time the supernova blast wave was passing the clouds, a fraction of the ejecta had already condensed in the blast wave's dense snowplow shell. When the shell collided with the neutral clouds, the latter were temporarily shock-heated to $\approx 10^4$ K but cooling by H_2 then quickly brought the temperature back down to ~ 100 K. In this blast wave-cloud collision, a tiny fraction of the ejecta was deposited in a thin layer at the cloud boundary. We detect this superficial deposition of metals on the surface of the metal-free cloud both in the passive scalar metallicity and the passive Lagrangian tracers. Figure 4.3 shows a slice through the cloud with the metallicity and temperature given in color scale and density contours as solid black lines. The Lagrangian particles tracing ejecta in a thin slab containing the slice are shown. Note the tracer particle concentration at the interface of the cold, dense cloud and hot, low density supernova remnant interior.

We are confident that the superficial metal deposition is a qualitatively correct prediction of the simulation, but some caveats are in order. The boundary layer where the ejecta 'sticking' to the cloud takes place is not adequately resolved: the forward shock in the cloud, the reverse shock in the blast wave, and the contact discontinuity that separates

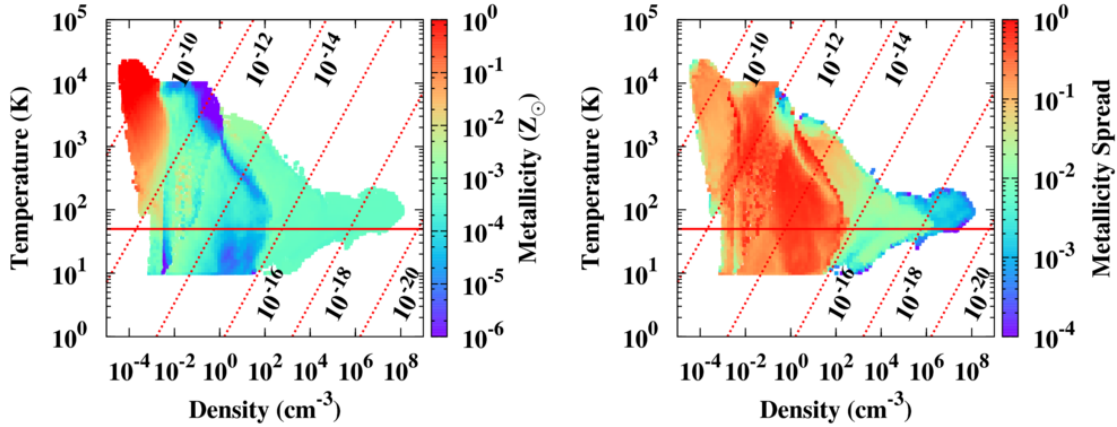


Figure 4.4: Density-temperature phase diagrams for gas within 1 kpc of the minihalo at the end of the simulation, 13.7 Myr after the explosion. The color scale shows the mass-weighted average metallicity (left panel) and the relative log-metallicity dispersion (right panel). Dispersions near unity reflect unmixed, chemically heterogeneous medium whereas lower values indicate homogenization. The densest gas with metallicity $\bar{Z}_{\text{scal}} \approx 10^{-3.3} Z_{\odot}$ has very low dispersion. We also show the lines of constant entropy (dotted; see Equation 4.3 and Figure 4.5). The solid line is the cosmic microwave background temperature $T_{\text{CMB}} = 53 \text{ K}$ at redshift $z = 18.5$.

them are partially blended together. This exacerbates the possibility of artificial passive scalar metallicity and internal energy diffusion across the blended discontinuity. We cannot claim to resolve the correct physical hydrodynamics of the blast wave-ejecta interface. For example, we do not resolve the Kelvin-Helmholtz instability that may develop there. Consequently, we cannot be confident in the numerical convergence of the total metal mass that has been deposited on the metal-free cloud. We describe how we attempt to exploit our dual ejecta tracking approach to constrain our prediction of the metallicity to a range of plausible values.

The metals deposited on the cloud surface did not initially mix with the cloud’s metal-free interior because the interior was not turbulent. Turbulent transport is a necessary (though perhaps not a sufficient) condition for compositional mixing to be possible (see, e.g., Pan, Scannapieco & Scalo, 2012, and references therein). Our resolution was not sufficient to reproduce the turbulent cascade within the cloud. Even if we had been able to simulate at the required resolution, we expect that such turbulence would have been very weak because there would not have been an agent to drive it after the blast wave has passed.

Cloud infall in the simulation can be described as follows. The superficially-enriched cloud fell close to the halo center after $\sim 6\text{--}7$ Myr. The infall tidally stretched the cloud into a narrow stream. As the stream fluid flowed across the grid, artificial numerical diffusion in the propagating compositional discontinuity at the stream surface (e.g., Ritter et al., 2012) mixed the metals at the surface with the hydrogen and helium in the interior. By the time the head of the stream made its closest approach to the halo center, the stream gas was homogenized at a low metallicity $Z_{\text{scal}} \approx 10^{-3.3} Z_{\odot}$, if measured from the passive scalar, and a factor of 3 lower, $Z_{\text{part}} \approx 10^{-3.8} Z_{\odot}$ if measured from the passive Lagrangian tracers. We expect that the true stream metallicity, if corrected for the varied numerical artifacts that likely affect the two values, is bracketed by the measured values.

The stream was on a non-radial orbit about the center of the minihalo dark matter potential. After it made its closest passage by the halo center, the approximately isothermal tidal compression raised the density to $\sim 10^4 \text{ cm}^{-3}$. In a pattern familiar from the simulations of clouds and stars disrupted by massive black holes in galactic nuclei (e.g., Burkert et al., 2012; Guillochon & Ramirez-Ruiz, 2013; Coughlin et al., 2016), after the pericenter passage the tidal stream is on an elliptical orbit and on a collision course with its own tail that has not yet reached the pericenter. The diameter of the elliptical orbit (major axis) is ≈ 10 pc. Interestingly, runaway gravitational collapse in the tidally-compressed stream gas takes place as the gas motion stalls at the apocenter of the ellipse. That a pair of dense clumps have broken from the head of the stream can be seen in the bottom-right panel of Figure 4.1. The peak density in the clumps loitered at $\lesssim 10^5 \text{ cm}^{-3}$ for ≈ 6 Myr. After the loitering period, as the density increased and temperature dropped, atomic fine-structure line cooling enabled gravitational instability and runaway collapse of the densest clump to density $> 10^8 \text{ cm}^{-3}$. This can be seen in the bottom-left of Figure 4.1 recorded at redshift $z = 18.5$, only 13.7 Myr after the supernova explosion.

The top two panels of Figure 4.2 show that the distribution of metals is not homogenous throughout the volume affected by the supernova blast wave. The most metal-rich gas is the low-density reverse-shocked interior of the ejecta. However the densest clumps in the bottom panels of Figure 4.2, which is where gravitational instability sets in, are quite homogenous, something that could in part be a numerical, finite-resolution artifact of the numerical diffusion of the passive scalar metallicity.

4.3 Analysis and discussion

4.3.1 Metal enrichment

In Figure 4.4 we show density-temperature phase diagrams for gas within a large 1 kpc sphere around the halo center. In the left panel we color the bins with the metallicity in solar units (Z_{\odot}). The warm gas at temperature $\sim 10^4$ K is the diffuse ($n_{\text{H}} \sim 10^{-4}$ – 10^{-3} cm^{-3}) and very metal rich (super-solar) bubble left behind by the supernova. The unpolluted gas ($Z_{\text{scal}} \leq 10^{-6} Z_{\odot}$) also at temperature $\sim 10^4$ K and at density $n_{\text{H}} \lesssim 1$ cm^{-3} is the photoheated intergalactic medium (IGM). The narrow strip of low metallicity medium that extends to temperature ~ 100 K and density $n_{\text{H}} \sim 100$ cm^{-3} is the cosmic web filament. At densities higher than $n_{\text{H}} \sim 100$ cm^{-3} we find the metal-enriched cloud and collapsed clump with uniform metallicity $Z_{\text{scal}} \approx 10^{-3.3} Z_{\odot}$.

The right panel of Figure 4.4 is the same plot but now colored to show the metallicity spread. We define the spread as the mass-weighted standard deviation of $\log Z_{\text{scal}}$ in units of the mass-weighted average value of $\log Z_{\text{scal}}$. The low density gas ($n_{\text{H}} < 100$ cm^{-3}) has a large metallicity scatter and is composed of unmixed pockets of metal-rich ejecta and pristine metal-free gas. The spread in the enriched cloud, with density $n_{\text{H}} > 100$ cm^{-3} , is small in comparison. The spread is almost negligible in the collapsed clump that has density $n_{\text{H}} > 10^4$ cm^{-3} . The decrease in metallicity spread in the collapsed clump relative to the uncollapsed clumps is a consequence of physical, but also numerical effects. Regardless of the numerical artifacts, self-gravitating gaseous collapse *is* expected to chemically homogenize the gas (see, e.g., Bland-Hawthorn et al., 2010; Feng & Krumholz, 2014). Taken at face value, the simulation leads us to predict that the stars that would form in the gas clump should have a common metallicity and equal fractional abundances, though, as we showed in Sluder et al. (2016), the abundances may not reflect the monolithic, explosion-averaged abundances of the supernova ejecta.

We present a simple model for how an initially metal-free cloud acquires a net metallicity through blasting by supernova ejecta. The cloud’s cross section can be approximated with a disk of cross-sectional area πr_{cloud}^2 . If the cloud is at a distance d_{cloud} from the explosion, the surface area of the blast wave when it reaches the cloud is $4\pi d_{\text{cloud}}^2$. The mass of metals ejected is the total supernova fractional mass yield, Z_{SN} , times the total ejecta mass, M_{SN} . Some fraction f_{eff} of the metals ejected in the cloud’s direction are deposited on the

cloud's surface. The net metallicity of the cloud can be estimated as

$$Z_{\text{cloud}} = f_{\text{eff}} \frac{M_{\text{SN}} Z_{\text{SN}}}{M_{\text{cloud}}} \frac{r_{\text{cloud}}^2}{4d_{\text{cloud}}^2}. \quad (4.1)$$

Relating the cloud's radius to its mass M_{cloud} and density n_{cloud} , we get

$$Z_{\text{cloud}} = f_{\text{eff}} \frac{M_{\text{SN}} Z_{\text{SN}}}{4M_{\text{cloud}} d_{\text{cloud}}^2} \left(\frac{3M_{\text{cloud}}}{4\pi m_{\text{H}} n_{\text{cloud}}} \right)^{2/3}. \quad (4.2)$$

For a cloud with mass $M_{\text{cloud}} = 1000 M_{\odot}$ and average density, $n_{\text{cloud}} = 100 \text{ cm}^{-3}$, we get an approximate cloud size $r_{\text{cloud}} \approx 5 \text{ pc}$. If we choose 10% for the capture efficiency, $f_{\text{eff}} = 0.1$, and substitute the distance to the cloud, $d_{\text{cloud}} = 50 \text{ pc}$, we obtain $Z_{\text{cloud}} \approx 10^{-4} Z_{\odot}$. This back-of-the-envelope calculation demonstrates that cloud surface enrichment by supernova blasting can be one of the enrichment mechanisms responsible for extremely metal poor star formation.

4.3.2 Cooling thresholds

In Figure 4.5 we plot metallicity and entropy for gas within the halo and nearby IGM. We parametrize the entropy using the argument, up to a constant factor, of the entropy logarithm,

$$S = \frac{k_{\text{B}} T}{n^{2/3}} \quad (\text{erg cm}^2). \quad (4.3)$$

The high-entropy, metal-rich tail in the upper right of the plot is the unmixed, reverse-shocked supernova ejecta. The lack of gas at high metallicities and low entropies on the lower right reflects geometric dilution in the dispersal of supernova ejecta. It may also have to do with a resolution-limited maximum density that metal-enriched gas gets compressed to in the thin snowplow shell.

The self-gravitating, collapsing clump appears as the low-entropy peninsula in the lower middle of the plot. The peninsula is narrow around $Z_{\text{scal}} \sim 10^{-3.3} Z_{\odot}$ (or 3 times lower, $Z_{\text{part}} \sim 10^{-3.8} Z_{\odot}$, if measuring metallicity with Lagrangian tracer particles) because the collapsing gas is chemically homogeneous. Outside of the peninsula, the plot exhibits an entropy floor at $S \sim 10^{-16} - 10^{-15} \text{ erg cm}^2$. Metal-free gas has been lumped into the lowest metallicity bin at $Z_{\text{scal}} = 10^{-6} Z_{\odot}$. The low-entropy (i.e., cold and dense) metal-enriched gas clump loitered at the entropy floor for several million years before dropping further in entropy, i.e., entering runaway gravitational collapse facilitated by cooling. It is not surprising that the entropy drop and the accompanying gravitational collapse happened in the

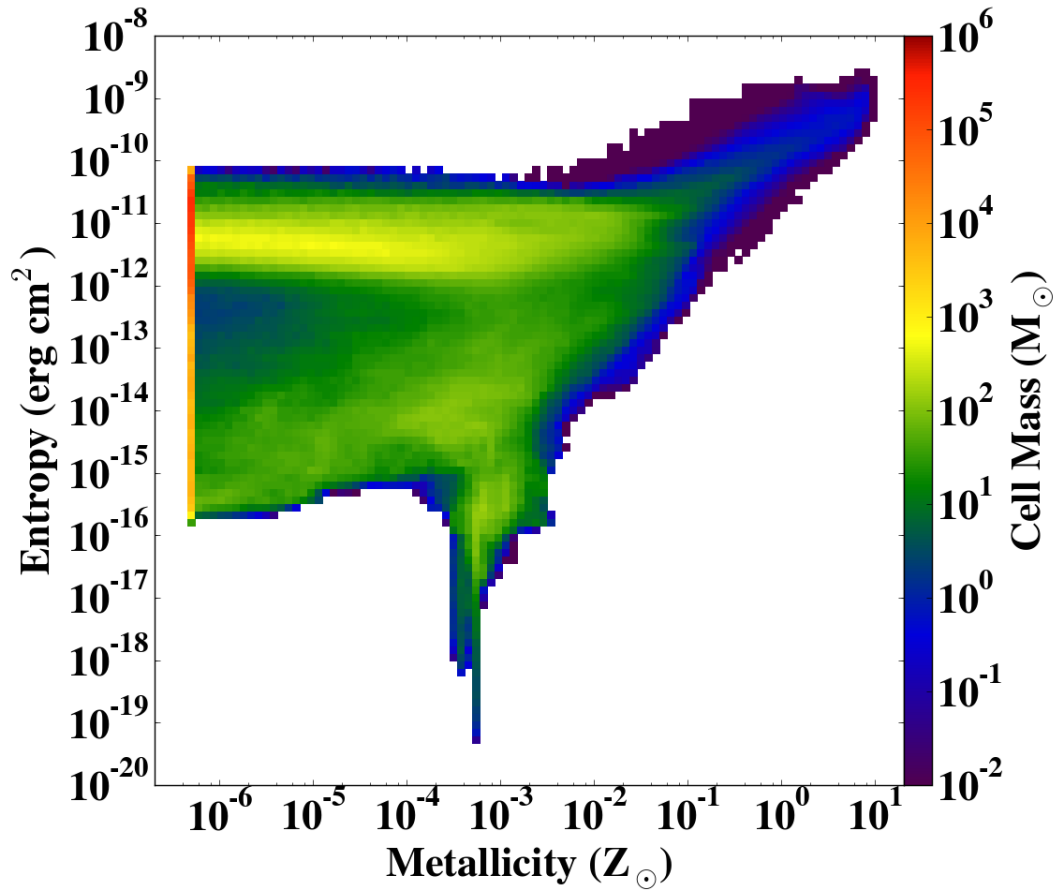


Figure 4.5: Metallicity-entropy phase diagram for gas within 1 kpc of the minihalo at the end of the simulation, 13.7 Myr after the explosion. Entropy here is as defined in Equation 4.3. Very low metallicity gas $Z_{\text{scal}} \leq 10^{-6} Z_{\odot}$ was placed in the leftmost column. The color scale is the total gas mass contained in each two-parameter bin. The unmixed, diffuse, shocked ejecta, some of which escaped the halo, are on the upper-right. The shock-heated dense clouds that were blasted with metals have cooled and homogenized near metallicity $\sim 10^{-3.3} Z_{\odot}$ and then undergo gravitational collapse to form the low-entropy peninsula in the bottom-middle.

most metal rich gas ($Z_{\text{scal}} \sim 10^{-3} Z_{\odot}$) lying on the entropy floor, because it is in that gas that the metallic fine structure line cooling is the strongest and the net cooling time due to H_2 and metals is the shortest.

Consider a gravitationally-bound, metal-enriched gas clump with temperature $\sim 100\text{K}$ collapsing isothermally at constant metallicity and H_2 abundance. The H_2 as well as C and O fine structure line cooling times are $t_{\text{cool},i} = \frac{3}{2}k_B T / \Lambda_i n_i$, where $i = (\text{H}_2, \text{Z})$ and the free fall time is $t_{\text{ff}} = (G\rho)^{-1/2}$. Each cooling process has a characteristic critical level-thermalization density n_{crit} above which the volumetric cooling rate scales no longer as $\propto n_{\text{H}}^2$, but as $\propto n_{\text{H}}$, and the cooling time saturates toward higher densities. At temperatures $\sim 100\text{K}$, the critical density for H_2 is $n_{\text{crit},\text{H}_2} \sim 100\text{ cm}^{-3}$, whereas for C and O is substantially higher, $n_{\text{crit},\text{Z}} \sim 10^6\text{ cm}^{-3}$. Just above the H_2 critical density molecular cooling is inefficient, and the metal cooling, with its time scale on the order of $\sim 1\text{--}100\text{ Myr}$, is still subdominant and comparable in magnitude to molecular cooling. For the specific conditions in the simulation, the three time scales ($t_{\text{cool},\text{H}_2}$, $t_{\text{cool},\text{Z}}$, t_{ff}) are roughly equal at density $n_{\text{H}} \sim 10^4\text{ cm}^{-3}$. This explains why the densest gas in the simulation loitered at $\sim 10^4\text{ cm}^{-3}$ for $\approx 6\text{ Myr}$ before resuming collapse.

When the cooling time in a Jeans-unstable clump becomes shorter than the free fall time, gravitational contraction can occur on a dynamical time scale. Shock compression in the gravitational infall may further shorten the cooling time and amplify short-wavelength density perturbations. The perturbations may be necessary for gravitational fragmentation into low mass protostellar cores (at densities still higher than attained in the present simulation). We observe a clear loitering phase at $n_{\text{H}} \sim 10^3\text{--}10^4\text{ cm}^{-3}$ where the drop of the H_2 cooling time under compression has saturated at a few million years and rises relative to the free fall time. With increasing metallicity, the metallic fine structure line cooling, with its substantially higher critical density, picks up cooling closer to where the H_2 cooling saturates; this reduces the loitering duration compared to metal-free conditions.

4.3.3 Gravitational instability

Consider a cold, dense gas clump at the threshold of gravitational instability. The thermal Jeans mass is

$$M_{\text{J}} \sim \frac{c_s^3}{\sqrt{G^3 \rho}}, \quad (4.4)$$

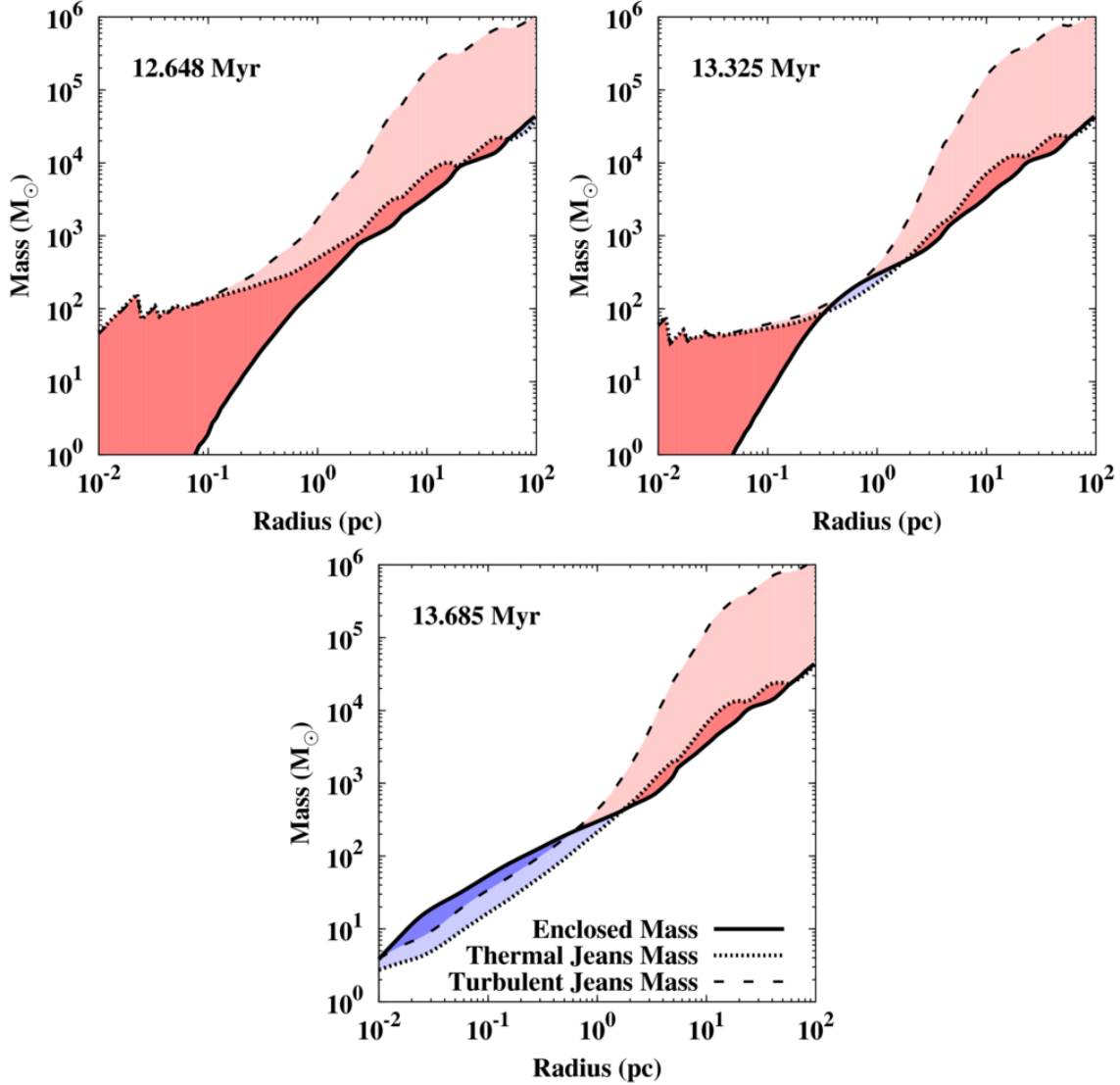


Figure 4.6: Mass profile plots of the enclosed mass as well as the thermal (Eq. 4.4) and turbulent (Eq. 4.5) Jeans masses, all calculated using averages within a sphere centered on the densest cell. We shade the region red, light blue, or dark blue, depending on whether neither or only the thermal criterion, or in turn both criteria are satisfied. The left panel at 12.6 Myr is before the onset of collapse, when the gas density loitered at $n_{\text{H}} \sim 10^4 \text{ cm}^{-3}$ and the enclosed mass was well below the Jeans mass (minimum cell size $\Delta x = 0.02 \text{ pc}$). The middle panel at 13.3 Myr is on the cusp of runaway gravitational collapse when the enclosed mass has exceeded the thermal Jeans mass on radial scales of $\sim 1 \text{ pc}$ ($\Delta x = 0.01 \text{ pc}$). The panel on the right at 13.7 Myr is when the gas has entered runaway collapse and the enclosed mass has exceeded the thermal and turbulent Jeans masses on all scales shown between 0.01 and 1 pc ($\Delta x = 4 \times 10^{-4} \text{ pc}$).

where c_s is the isothermal sound speed. The turbulent Jeans mass can be obtained by replacing the thermal sound speed with an effective velocity dispersion v_{eff} that combines in quadrature the isothermal sound speed and the turbulent velocity dispersion

$$M_{\text{J,turb}} \sim \frac{v_{\text{eff}}^3}{\sqrt{G^3 \rho}}. \quad (4.5)$$

where

$$v_{\text{eff}}^2 = c_s^2 + v_{\text{turb}}^2 \quad (4.6)$$

and v_{turb} is the mass-weighted standard deviation of the velocity component along any fixed axis.

Gas clumps collapsing under self-gravity should satisfy the turbulent Jeans criterion $M_{\text{enclosed}} > M_{\text{J,turb}}$. Figure 4.6 shows the spherical enclosed mass and the thermal and turbulent Jeans masses as a function of radius. In the left panel which shows the gas clump during the loitering phase, before gravitational instability has set in, we notice that neither criterion is met. In the middle panel, 675 kyr later, the mass enclosed within radius $r \sim 1$ pc has marginally exceeded the thermal Jeans mass. The gas does not immediately become gravitationally unstable after crossing this threshold, however, because of the additional turbulent velocity dispersion with Mach numbers just above unity. In fact, we see in the right panel that it takes an additional 350 kyr before both Jeans criteria are satisfied and the collapse can proceed to smaller scales, down to the minimum cell size ($\Delta x = 4 \times 10^{-4}$ pc).

It is interesting that second generation stars will form in a kinematic state different from that of the first metal-free star. Pop III stars form very close to dark matter potential minima because dark matter gravity drives gas compression down to very small scales $\lesssim 1$ pc (e.g., Bromm, Coppi & Larson, 2002). Here, however, the metal-enriched pre-stellar clump poised to form Pop II stars can go into runaway gravitational collapse on an orbit that resides farther from the dark matter potential minimum (see the bottom-right panel of Figure 4.1). This is a consequence of the removal of gas from the halo center by HII region heating and supernova ram pressure, as well as the rapid cooling in the clouds that fall toward the center. Since the cooling is rapid enough for the clouds to lose thermal energy before their kinetic energy can be dissipated, the new stars will be placed on large elliptical orbits, in this case ~ 10 pc, in agreement with the half-light radii of the very faintest UFDs (e.g., Bechtol et al., 2015; Drlica-Wagner et al., 2015; Koposov et al., 2015).

4.3.4 The relation to extremely metal-poor stars

The carbon-enhanced metal-poor stars, or CEMP stars in the nomenclature of Beers & Christlieb (2005), are identified by having carbon-iron abundances $[C/Fe] > 0.7$. They become increasingly common and more carbon-rich for iron abundances decreasing below $[Fe/H] < -1$. The unenhanced, carbon-normal metal-poor stars have iron abundances that reach as low as $[Fe/H] \sim -5$ (Caffau et al., 2011; Norris et al., 2013). The most extreme examples of carbon-rich stars, with $[C/Fe] > 3$, are also the most extreme iron-poor stars with $[Fe/H] < -5$ (Christlieb et al., 2002; Frebel et al., 2005; Keller et al., 2014). Some carbon-rich iron-poor stars in the range $-3 < [Fe/H] < -1$ also have enhancements of the more rare s- and r-process neutron capture elements (Snedden et al., 1996; Cayrel et al., 2001; Frebel, Johnson & Bromm, 2007), while below $[Fe/H] < -3$, the carbon-rich stars show few signs of neutron-capture enhancement (Aoki et al., 2010). The high degree of chemical variability in the most iron-poor stars tells us that the relative contributions from different classes of nucleosynthetic sources had not yet been homogenized when the stars formed. There is a growing class of chemically primitive stars with $[Fe/H] < -5$ in which we clearly see the fossil imprint of individual nucleosynthetic sources, possibly even a single progenitor supernovae (Christlieb et al., 2002; Frebel et al., 2005; Keller et al., 2014). If the first stars predominantly exploded as core-collapse supernovae, each enriching gas with large amounts of α -elements but relatively little iron, could they explain the universal carbon enhancement seen at $[Fe/H] < -5$ (Norris et al., 2013)?

The stars which could form from the dense, metal-enriched gas clump in our simulation would have a metallicity in the range $(10^{-3.3} - 10^{-3.8}) Z_{\odot}$, consistent with the canonical critical metallicity $Z_{\text{crit,fs}} = 10^{-3.5} Z_{\odot}$ for low-mass star formation in the absence of dust. In Figure 4.7 we plot the carbon-to-iron ratio for known iron-poor stars with $[Fe/H] < -2$ (Yong et al., 2013a; Norris et al., 2013). The black points are carbon-normal stars with $[C/Fe] < 0.7$. The red points are carbon-rich stars with $[C/Fe] > 0.7$, but those that show no sign of neutron-capture enrichment (i.e., CEMP-no). The blue points are carbon-rich stars that do show signs of additional s- and/or r-process enrichment, using the criteria of Beers & Christlieb (2005) for CEMP-r, CEMP-s, and CEMP-r,s stars. The most iron-poor star currently known SMSS J031300.36-670839.3 (Keller et al. 2014; unfilled red point), is also the most carbon-rich with an iron abundance upper limit of $[Fe/H] < -7.1$ and a carbon-to-iron ratio of at least $[C/Fe] > 4.5$. The most metal-poor star currently known, SDSS J102915+172927 (Caffau et al. 2011; unfilled black point), is the most iron-poor

of the carbon-normal stars with $[\text{Fe}/\text{H}] = -5$, an upper-limit $[\text{C}/\text{Fe}] < 0.7$, and metallicity $Z = 10^{-4.35} Z_{\odot}$. The shaded region with carbon abundance thickness $-3.8 < [\text{C}/\text{H}] < -3.3$ represents the abundance space locus where the stars formed from our simulated gas clump would be found. The extent of the carbon-iron ratio in the shaded region, $1 < [\text{C}/\text{Fe}] < 4$, models uncertainty in both the unknown supernova yield and the potential hydrodynamical enrichment bias that could make the carbon-to-iron ratio in the captured ejecta differ from that of the bulk supernova ejecta (see Sluder et al., 2016). The large scatter among the stars in this part of abundance space reflects these theoretical uncertainties and implies a significant degree of stochasticity in the earliest enrichment (Webster, Frebel & Bland-Hawthorn, 2016).

4.4 Summary

We conclude by briefly reviewing our main results. This work demonstrates that extremely metal poor ($Z \sim 10^{-4} - 10^{-3} Z_{\odot}$) stars can form in cosmic minihalos enriched by single, low-energy core collapse supernovae from Pop III star progenitors. Incomplete photoionization of the Pop III star's host halo and marginally effective carbon and oxygen fine structure line cooling allow extremely metal poor stars to form only ~ 10 Myr after the Pop III supernova explosion.

The time scale for recycling ejecta from the first supernovae into second-generation stars depends critically on the presence of neutral gas clouds that can entrain ejecta from the passing blast wave. The compression and deposition of metals onto the cloud enhances cooling and ultimately leads to gravitational collapse to form new metal-poor stars on shorter timescales, and at higher metallicities, than through the fallback of enriched ISM and IGM returning into the dark matter halo center. While this simulation did not have sufficient resolution to properly track a time-dependent ionization front eating into a photoevaporating cloud, analytical considerations give us reason to believe that gas with properties similar to that of the birth cloud can survive inside the HII region long enough to outlive a Pop III star (Bertoldi, 1989; Bertoldi & McKee, 1990).

The survival of a neutral gas cloud in an HII region is characterized by δ , the initial width of the ionized cloud layer relative to the cloud radius, which scales with the ratio of the photoionization parameter ξ to the neutral hydrogen column density $N_{\text{H}} \sim r_{\text{cloud}} n_{\text{H}}$ (Bertoldi, 1989). In terms of the initial cloud properties and source flux, this dimensionless

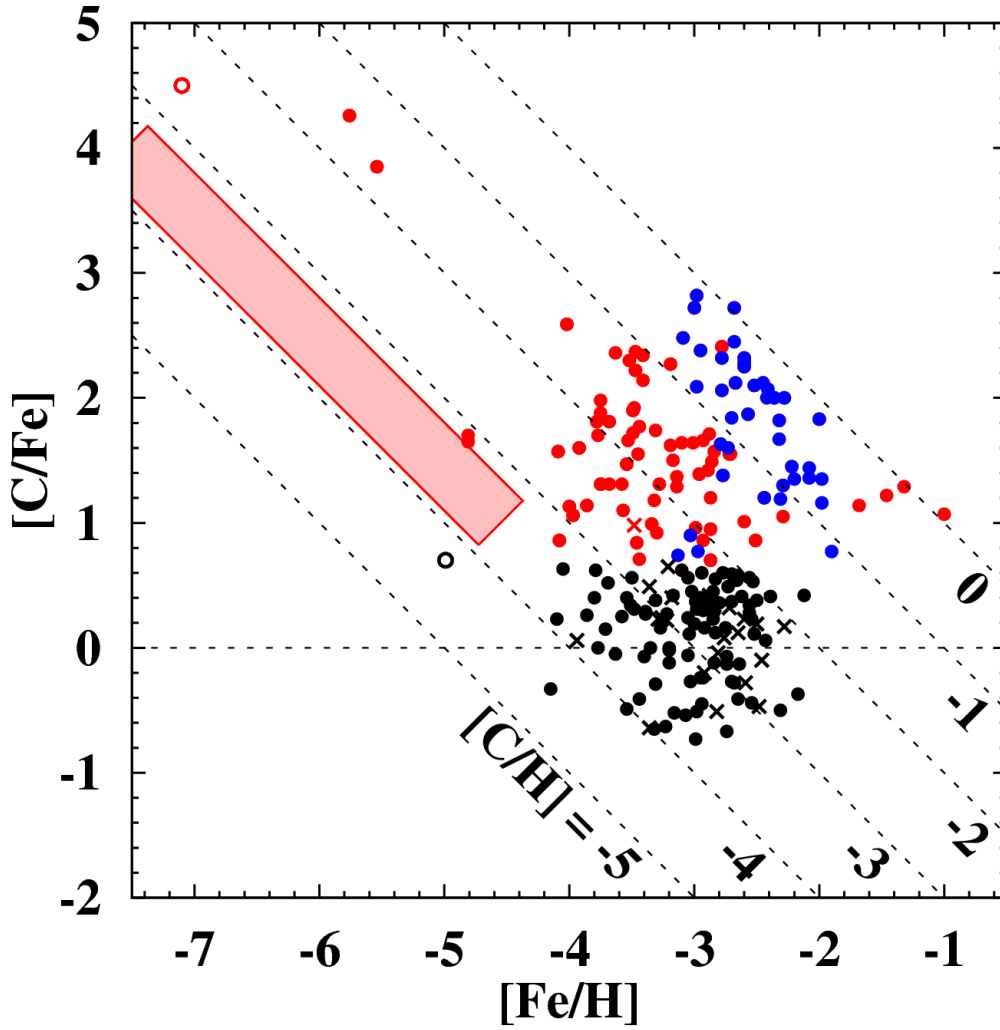


Figure 4.7: Chemical abundance log-ratios $[\text{Fe}/\text{H}]$ and $[\text{C}/\text{Fe}]$ in the known metal-poor stars compiled from Caffau et al. (2011), Yong et al. (2013a), Norris et al. (2013), Keller et al. (2014), and Howes et al. (2015). The stars are colored depending on whether they are normal (black) or carbon-rich without (red) or with neutron capture enhancement (blue). Metal-poor stars from the Galactic bulge are identified using crosses, while all other stars are identified using circles. The carbon-rich, iron-poor star SMSS J031300.36-670839.3 (Keller et al., 2014) is an open red circle. The carbon-normal, iron-poor star SDSS J102915+172927 (Caffau et al., 2011) is an open black circle. The diagonal dashed lines trace constant $[\text{C}/\text{H}]$, which, assuming $[\text{C}/\text{O}] \approx 0$, is approximately equal to the metallicity. The shaded region $-3.8 < [\text{C}/\text{H}] < -3.3$ represents the stars that could have formed in our simulated gas clump assuming a range of carbon enhancements $1 < [\text{C}/\text{Fe}] < 4$.

factor becomes

$$\delta = 5.23 \times 10^{-2} \left(\frac{S_{49}}{n_3^2 r_{\text{pc}} R_{\text{pc}}^2} \right), \quad (4.7)$$

where $S_{49} = Q/10^{49}$ photons per second, $n_3 = n_{\text{H}}/10^3 \text{ cm}^{-3}$, r_{pc} is the cloud radius in parsecs, and R_{pc} is the distance from the cloud to the ionizing source in parsecs (see Eq. 2.8 of Bertoldi, 1989). Clouds with $\delta > 1$ are quickly vaporized, whereas clouds with $\delta < 1$ are evaporated more slowly and survive for some time. For reference cloud density 10^3 cm^{-3} and radius 1 pc as well as initial distance 1 pc, $\delta = 0.25$ and we expect the cloud to evaporate slowly (in our case $S_{49} = 4.795$). For a cloud that remains at a fixed distance from the star, the evaporation time can be derived from Eqs. 3.27 and 4.10a of Bertoldi & McKee (1990)

$$t_{\text{evap}} \approx 7.43 \times 10^7 \left(\frac{R_{\text{pc}}^2 n_3^2 r_{\text{pc}}^6}{S_{49} T^3} \right)^{1/5} \text{ years}. \quad (4.8)$$

Given the initial cloud parameters above and temperature $T = 200 \text{ K}$, the evaporation time $t_{\text{evap}} = 2.26 \text{ Myr}$ is only about 2/3 of the lifetime of a $60 M_{\odot}$ Pop III star. However these authors note, and we also observe in our simulation, that the ionized gas pressure force can push the cloud out by several tens of parsecs. Displacement of the cloud from the star decreases the incident flux with the square of the increasing distance. If the cloud is pushed away to only $R_{\text{pc}} = 10 \text{ pc}$ it would have an evaporation time $t_{\text{evap}} = 5.68 \text{ Myr}$, several million years longer than the host star's lifetime. This model suggests that surviving neutral clouds are generic in HII regions of single $\lesssim 60 M_{\odot}$ Pop III stars in minihalos. If present, these clouds can become the birth sites for the first metal-poor stars.

The enrichment mechanism we identify here differs from the well explored scenario involving ultra-energetic (e.g., pair instability) Pop III supernovae (Wise & Abel, 2008a; Greif et al., 2010). Since pair instability supernovae (PISNe) synthesize large ($\sim 50 M_{\odot}$) metal masses and inject them with large ($\sim 10\text{--}100 \times 10^{51} \text{ erg}$) initial kinetic energies, the formation of very metal poor PISN-enriched stars would require metal dilution, through hypothesized pervasive hydrodynamic mixing, over a large cosmic volume. Even then, the abundances of PISN-enriched stars would differ from those in the extremely metal poor stars observed to date (e.g., Frebel & Norris, 2013b; Yong et al., 2013a).⁶

In contrast with the massive progenitor, ultra-energetic explosion Pop III enrichment scenario, we find that the first metal-enriched gravitationally collapsing pre-stellar clump

⁶Tentative PISN enrichment pattern evidence has been found only in one less-than-extremely metal poor ($[\text{Fe}/\text{H}] \approx -2.5$) star (Aoki et al., 2014).

acquires its extremely low metallicity through superficial deposition by a transient supernova blast wave. The blast wave deposits a small mass of metal-rich supernova ejecta on the surface of the clump's progenitor cloud. Correcting for numerical artifacts, we expect that chemical homogenization in the pre-stellar clump does not occur before the clump has entered runaway gravitational collapse when turbulence, if present, can facilitate compositional mixing.

We find that cooling by carbon and oxygen fine structure line emission is an effective accelerator of the formation and collapse of the metal-enriched pre-stellar clump. We also find that the clump enters collapse on an elliptical orbit around the dark matter halo gravitational center. This implies that extremely metal poor stars can be born with a significant initial radial velocity dispersion. If the halo survives as a dwarf galaxy, stellar dynamical evolution could isotropize the velocity dispersion tensor on Gyr time scales. The radial orbital extent may be preserved and would be reflected in the half-light radii of, e.g., the UFD satellite galaxies, local systems within observational reach of stellar archaeological studies.

The confluence of ongoing large stellar archaeological surveys such as Gaia and SkyMapper with high-resolution cosmological simulations of chemically primitive star formation environments is opening up a powerful window into the nature of the first stars and galaxies. In particular, we can now begin to understand the multiplicity of the initial chemical enrichment process, single vs. multiple supernova pathways, and formulate robust empirical near-field cosmological tests of our emerging theoretical framework.

Chapter Five: Simulating galactic outflows one supernova at a time

Galactic outflows are a vital component of galaxy evolution that act to regulate star formation and chemical enrichment (Dekel & Silk, 1986). It has long been theorized that the combined energy and momentum input from supernovae (SNe) could be responsible for driving these outflows (Chevalier & Clegg, 1985; McCray & Kafatos, 1987). Galactic winds driven by SNe may play a significant role, particularly for low-mass galaxies, in explaining the stellar mass function (Dekel & Silk, 1986; Mashchenko, Wadsley & Couchman, 2008; Peebles & Shankar, 2011), the mass-metallicity relationship (Tremonti et al., 2004; Erb, 2008; Finlator & Davé, 2008), and metal enrichment of the CGM (Madau, Ferrara & Rees, 2001; Scannapieco, Ferrara & Madau, 2002; Oppenheimer & Davé, 2006). Winds play an important role in the balance of cosmological gas accretion with the ejection of gas from a galaxy, and by transferring high-entropy, metal-rich gas from the central disk to the outer halo. Photoheating could explain the suppression of star formation in the very smallest galaxies, however it is insufficient to explain the suppression of more massive halos $M \gtrsim 10^9 M_{\odot}$ (Efsthathiou, 1992; Okamoto, Gao & Theuns, 2008). Supernova feedback is invoked to explain the observed lack of low mass galaxies compared to the number expected from Λ CDM (Rees & Ostriker, 1977; White & Rees, 1978; White & Frenk, 1991). Momentum injection by SNe may be the most important source of feedback in the self-regulation of galactic star formation rates (Kim, Kim & Ostriker, 2011; Ostriker & Shetty, 2011).

Observations at low redshift (Heckman, Armus & Miley, 1990; Heckman et al., 2000) and high redshift (Pettini et al., 2001) confirm the ubiquitous presence of outflows around star forming galaxies, while metal-enriched gas has been found in the IGM between galaxies (Cowie et al., 1995; Schaye et al., 2003; Aguirre et al., 2004). The outflow in M82 is the most well-studied galactic wind, beginning with the discovery of emission from filamentary structures extending several kpc, in the optical (Lynds & Sandage, 1963), as well as the UV (Hoopes et al., 2005) and IR (Contursi et al., 2013; Beirão et al., 2015). Emission line ratios from the $T \sim 10^4$ K filaments are consistent with both photo-heating by radiation and shock-heating by the hot wind (Heckman, Armus & Miley, 1990), with constant

outflow velocities of 600 km/s beyond 600 pc (Shopbell & Bland-Hawthorn, 1998). The warm optical filaments are co-spatial with soft X-ray emission located interior to the filaments (Lehnert, Heckman & Weaver, 1999), which could be indicating the fast moving wind is interacting with and shocking the slower moving filamentary gas. Molecular gas emission (Veilleux, Rupke & Swaters, 2009; Beirão et al., 2015; Leroy et al., 2015), atomic HI 21 cm line emission (Leroy et al., 2015), and metal fine-structure lines (Contursi et al., 2013) have been observed in the outflow with speeds ~ 100 km/s. Velocities have been inferred for a hollow, bi-conical outflow from the double-peaked line profiles (Heckman, Armus & Miley, 1990; Shopbell & Bland-Hawthorn, 1998). The measured warm ionized gas outflow rate in M82 within ~ 1 kpc of the starburst is $0.2 - 0.3 M_{\odot} \text{ yr}^{-1}$ (Heckman, Armus & Miley, 1990; Shopbell & Bland-Hawthorn, 1998). The highest measured mass outflow rates in M82 are of warm neutral and cold gas (10 and $30 M_{\odot} \text{ yr}^{-1}$ respectively Contursi et al., 2013; Leroy et al., 2015). These properties lead to analytical estimates for the mass-loaded outflow rate of hot gas from 2 to $3 M_{\odot} \text{ yr}^{-1}$ (Strickland & Heckman, 2009).

Outflows around other galaxies have been observed to have broadened optical (Heckman et al., 2000; Rupke, Veilleux & Sanders, 2005; Martin, 2005) and UV (Grimes et al., 2009) absorption features. Wind velocities in mature starburst galaxies are typically 100 to 1000 km/s (Chisholm et al., 2015; Heckman et al., 2015; Heckman & Borthakur, 2016) with multiphase cool, warm and hot gas tracing the outflows. The outflows around starburst dwarf galaxies are usually not as fast, with speeds of 10 to 100 km/s (Marlowe et al., 1995; Martin, 1998). Outflows at high redshift have been studied using interstellar absorption lines (Steidel et al., 2010; Martin et al., 2012). For a broad sample of starburst galaxies (Heckman & Borthakur, 2016), the maximum wind velocity has been observed to scale most strongly with the star formation rate surface density ($M_{\odot} \text{ yr}^{-1} \text{ pc}^{-2}$).

The classical analytical solution for a hot bubble driven by continuous energy injection was given by McCray & Kafatos (1987), with analogous solutions for stellar wind-blown bubbles (Avedisova, 1972; Castor, McCray & Weaver, 1975; Weaver et al., 1977). Early numerical simulations of SN-driven winds sought to reproduce the global properties of observed outflows, such as the wind in M82, by aggregating the effects of many SNe into an unresolved region where mass and energy are injected at a constant rate (Scannapieco, Thacker & Davis, 2001; Cooper et al., 2008; Sarkar et al., 2015; Schneider & Robertson, 2018). These low- and medium-resolution simulations assume that the properties in the injection region had already been established by earlier processes within the idealized interstellar medium (ISM) of a galactic disk. They depend on a continuous star formation

relation (e.g. Kennicutt, 1998) to replenish outflowing mass and energy in the injection region at a constant rate. More recent moderate-to-high resolution outflow simulations that explore the effects of individual SNe, such as Creasey, Theuns & Bower (2013); Scannapieco (2017); Kim, Ostriker & Raileanu (2017), initialize their remnants in an advanced stage where one must make assumptions about the thermalization efficiency and density structure that quickly break down when the remnants begin to interact with the surrounding medium.

The assumptions used in semi-analytic hot wind models generally do not scale down to the very first galaxies, which were more compact, extremely metal poor, and likely did not form stars as efficiently (Filho et al., 2016). Numerical models only briefly speculate about the role of winds in low mass galaxies (Scannapieco, Thacker & Davis, 2001). High-resolution 1D blast wave simulations indicate that radiative cooling typically removes about 90% of the initial SN energy (Thornton et al., 1998). Most wind models assume a fixed value for this thermalization efficiency that likely does not remain constant when remnants overlap to form a superbubble (SB), therefore methods that aggregate SN energy may not reproduce the correct rate of heat deposition. The interstellar medium (ISM) within galactic disks often have a complex, multi-phase structure (Elmegreen, Kim & Staveley-Smith, 2001). Supersonic turbulence has been observed within galactic disks (Dopita et al., 1997). The initial state of the ISM around the source of an outflow when it is first launched will have a significant impact on the properties of the outflow when it reaches steady state equilibrium (Cooper et al., 2008). The inadequate assumptions of previous numerical models, in the context of the very first galaxies, require one to simulate as much as possible from first principles the construction of the galactic disk, and the deposition of mass and energy, in order to avoid degeneracy among the model parameters.

Here we lay out a numerical framework for simulating the formation of a SN-driven outflow from the first galaxy, one SN at a time. Rather than construct a galaxy model using idealized analytical arguments, we instead start with the output of a realistic, 3D cosmological hydrodynamics simulation of the formation of a $10^9 M_{\odot}$ galaxy (Pawlik, Milosavljević & Bromm, 2013a). Embedded within the host dark matter potential is a $10^7 M_{\odot}$ gaseous spiral disk. On top of that, we implement a simple radiative transfer scheme to photoionize the gaseous disk and create an HII region with realistic multiphase structure. One of the key improvements required is to resolve the individual SN remnant radii when they are inserted in the free expansion phase, where each remnant's properties are still well-described by simple analytical arguments and before interaction with the surrounding medium intro-

duces non-linear thermalization and cooling effects. Simultaneously we must resolve the large-scale expansion of the many overlapped SN remnants that merged into a single larger SB. The long-term evolution of the SB is followed for several million years as it expands and eventually breaks out of the galactic disk. The conditions within the bubble just after breakout can give us key insights into the properties of the outflow that eventually develops.

This chapter is organized as follows: in section 5.1 we present a model for SN-driven outflows in the first galaxies, in section 5.2 we detail the configuration of our numerical simulation, in section 5.3 we present the preliminary results of our simulation, and in section 5.4 we discuss the potential for a hot wind to develop from repeated SNe in the first galaxy.

5.1 The First Galaxies

Under the prevailing cosmological model for cold dark matter (Λ CDM), the first stars likely formed in minihalos ($\sim 10^6 M_{\odot}$) with a top-heavy initial mass function (IMF) characteristic of metal-free stars (Bromm, Coppi & Larson, 2002). The massive Population III (PopIII) stars formed in relative isolation and died as SNe only a few million years later. A typical core-collapse SN (10^{51} erg) can obliterate a minihalo, spreading ejecta rich in α -elements into the intergalactic medium (IGM Ritter et al., 2016). Pollution of the pristine primordial gas with metals from the first stars drastically altered the nature of star formation. The Population II (PopII) stars formed from gas that had been metal-enriched up to at least a critical threshold metallicity $\sim 10^{-5}$ – $10^{-3.5} Z_{\odot}$ (Bromm et al., 2001; Bromm & Loeb, 2003b; Santoro & Shull, 2006; Smith et al., 2009). While scenarios exist for the prompt formation of second generation stars only a few tens of millions of years after the first stars (Ritter et al., 2012; Smith et al., 2015b), the major paradigm shift in the mode of star formation occurs a few hundred million years later when polluted gas from the IGM is pulled back into the growing dark matter gravitational potential. External background radiation sources compete with enhanced cooling afforded by metal enrichment until sufficient density where the gas streaming into the center of the dark matter potential becomes Jeans unstable and rapidly collapses to higher density. Thermal instability fragments the gas even further, leading to the formation of a larger population of lower mass stars than in the PopIII IMF. The first galaxies were formed when a large number of low mass stars were born with lifetimes much longer than the dynamical time of their host dark matter

halo.

5.1.1 Modeling the First Galaxy

The smallest dwarf galaxies that we observe around the Milky Way have stellar velocity dispersions fit by dark matter halos with masses 10^8 – $10^9 M_\odot$ (Walker, Mateo & Olszewski, 2008). Because structure in a Λ CDM cosmology grows hierarchically from small to large, the galaxies that formed first in a particular region of the universe are likely the largest galaxies in that region at redshift 0, and these satellite galaxies likely do not directly represent the very first galaxies in the universe. The mass-metallicity relationship among the dwarf spheroidals shows a trend of increasing (sub-solar) metallicity with increasing stellar and dynamical mass (Kirby et al., 2013), implying that metal-enrichment is driven by continued star formation during cosmological structure growth. The dwarf spheroidals have not yet merged into the Milky Way at redshift 0 and one might assume that they formed in much the same way as the first galaxies, but at a later redshift and in a lower density region than the Milky Way. They may in fact represent a class of the first galaxies which formed only a few generations of metal-poor stars before exhausting their limited gas supply through a combination of star formation and outflows.

An HI atomic cooling halo with mass $10^9 M_\odot$ is thought to be one of the first cosmological structures massive enough to host a large population of stars. The dynamical mass-scale closely resembles that of dwarf spheroidals. If the gas in such a halo had been polluted at least up to the critical metallicity by a previous generation of PopIII stars, then we might expect some of those stars to have small masses and to be long-lived. At large radii the dark matter and gas density follow a profile similar to an isothermal sphere with $\rho \propto r^{-2}$. At small radii, much less than the virial radius $R_{\text{virial}} \sim 3 \text{ kpc}$, a significant fraction of the total gas mass settles into a thin disk. The vertical scale height of the disk is $H = c_s^2/g$, where $c_s^2 = k_B T / \mu m_H$ is the square of the isothermal sound speed. The disk surface gravity $g = G \Sigma_{\text{gas}}$ depends on Newton’s constant times the gas surface density $\Sigma_{\text{gas}} = M / \pi R^2$, assuming cylindrical symmetry for a disk with mass M_{disk} and radius R_{disk} . The vertical scale height of the model disk is then

$$\begin{aligned}
 H &= \left(\frac{k_B T}{\mu m_H} \right) \left(\frac{\pi R_{\text{disk}}^2}{G M_{\text{disk}}} \right) \\
 &= 60 \text{ pc} \left(\frac{T}{10^4 \text{ K}} \right) \left(\frac{R_{\text{disk}}}{100 \text{ pc}} \right)^2 \left(\frac{M_{\text{disk}}}{10^7 M_\odot} \right)^{-1}. \quad (5.1)
 \end{aligned}$$

5.1.2 Stars in the First Galaxy

Radiatively cooled gas accumulates in the galactic disk, but it is the cloud near the center of the disk whose density first grew large enough to become thermally unstable and fragmented to form stars. A fraction $\sim 10\%$ of the collapsed gas with density $n \gtrsim 10^3 \text{ cm}^{-3}$ goes on to form a nuclear cluster of stars. The massive stars ($M \gtrsim 8 M_\odot$) that are destined to explode as SNe also produce the majority of hydrogen-ionizing UV photons. The maximum ionizing photon production rate varies widely with the chosen IMF slope and upper mass limit (Sternberg, Hoffmann & Pauldrach, 2003). Here we have assumed a Salpeter (1955) slope with masses in the range $1\text{--}100 M_\odot$. A star cluster with mass $10^5 M_\odot$ that formed instantaneously will emit hydrogen-ionizing Lyman Continuum (LyC) photons at a roughly constant rate $Q_{\text{LyC}} \sim 10^{52} \text{ s}^{-1}$, while a cluster continuously forming stars at a rate $1 M_\odot \text{ yr}^{-1}$ slowly ramps up the ionizing photon production rate as the population grows, plateauing after a few million years with a rate $\sim 10^{53} \text{ s}^{-1}$ (Sternberg, Hoffmann & Pauldrach, 2003).

The photoionized bubble around an ionizing point source is bounded by its Strömgen radius R_S . An instantaneously formed $10^5 M_\odot$ cluster could ionize a sphere with Strömgen radius $\sim 1 \text{ kpc}$, comparable to the virial radius, if the average density enclosed within the disk's radius is $\sim 1 \text{ cm}^{-3}$. If we assume spherical symmetry then the number of ionizing photons produced per second is equal to the total recombination rate within the volume of the Strömgen sphere,

$$Q_{\text{LyC}} = \alpha_B n_H^2 \frac{4\pi}{3} R_S^3 \quad (5.2)$$

where the case B hydrogen recombination coefficient α_B times the density of hydrogen nuclei squared n_H^2 equals the volumetric cooling rate of an optically thin, ionized gas. A typical value for α_B in gas with temperature 10^4 K is $\sim 10^{-13} \text{ erg cm}^3$. This balance equation can be rearranged to solve for the Strömgen radius

$$R_S = \left(\frac{3Q_{\text{LyC}}}{4\pi\alpha_B n_H^2} \right)^{\frac{1}{3}} \quad (5.3)$$

which scales as $n^{-2/3}$. Dense gas could potentially bottle up the ionizing radiation, however if even a tenth of the ionizing photons are able to leak out then the Strömgen radius only drops to 0.5 kpc , still large enough to photoionize a small galactic disk.

Photoionized gas is heated and the central pressure gradient drives gas away from the source. The central density is determined by the ratio of pre- and post-heating temperature $\epsilon = T_i/T_{\text{HII}}$ and decreases proportional to t^{-2} with a self-similar profile (Shu et al., 2002). A

thick shell builds up around the high pressure region and expands with constant velocity also determined by the ϵ factor. The density within the HII region is relatively uniform on scales smaller than the shell radius. Density inhomogeneity within the disk is wiped out over the lifetime of the most massive stars (~ 3 Myr) as the shell expands to a few 100 pc, comparable to the size of the disk itself. The remaining dense clouds are carried in the shell and deposited in a toroidal ring near the edge of the disk where the vertical scale height has been increased by a factor ϵ^{-1} . The HII region of a modest nuclear star cluster embedded within the disk of the first galaxy is expected to homogenize the ISM, lowering the uniform density while extending the vertical height of the disk, in stark contrast to the clumpy or exponentially stratified disks that have been considered in outflow simulations modeling more massive galaxies.

5.1.3 Supernovae in the First Galaxy

In this section we summarize the evolutionary phases of a SN remnant based on Draine (2011, chapter 39). We then extend that model to include multiple SN remnants overlapping and look at whether their combined effort would allow the resulting SB to break out of the photoionized disk and into the outer halo. The SN rate for an instantaneously formed star cluster is relatively constant from ~ 3 Myr to ~ 40 Myr, during the range of lifetimes for massive stars $8\text{--}100M_{\odot}$ (Leitherer et al., 1999). The average time between SNe for a star cluster of mass M_* with a single power-law IMF ($\alpha = 2.3$ between $1\text{--}100M_{\odot}$) is

$$\Delta t_{\text{sn}} \approx 66 \text{ kyr} \left(\frac{M_*}{10^5 M_{\odot}} \right)^{-1} \quad (5.4)$$

if we assume all stars with masses greater than $8M_{\odot}$ explode as SNe. Using this IMF 38% of the cluster mass is contained in stars massive enough to go SN, with average SN progenitor mass $20M_{\odot}$, or about 2 SNe per $100M_{\odot}$.

5.1.3.1 Free Expansion of Ejecta

A model SN remnant first begins as a metal-rich sphere with uniform density ejecta ρ_{sn} . In order to ensure that the remnant undergoes proper phase changes after initialization we must choose an initial ejecta density that is much greater than the ambient density,

$\rho_{\text{sn}} = 10\rho_{\text{amb}}$, which also dictates the initial radius of the remnant

$$\begin{aligned} R_{\text{sn}} &= \left(\frac{3}{4\pi} \frac{M_{\text{sn}}}{\rho_{\text{sn}}} \right)^{1/3} \\ &\approx 0.73 \text{ pc} \left(\frac{M_{\text{sn}}}{1 M_{\odot}} \right)^{1/3} \left(\frac{n_{\text{amb}}}{1 \text{ cm}^{-3}} \right)^{-1/3} \end{aligned} \quad (5.5)$$

for a fixed ejecta mass M_{sn} and ambient number density $n_{\text{amb}} \sim \rho_{\text{amb}}/m_{\text{H}}$. For convenience we introduce the following unit scaling variables

$$\begin{aligned} E_{51} &= \frac{E_{\text{sn}}}{10^{51} \text{ erg}} & M_0 &= \frac{M_{\text{sn}}}{1 M_{\odot}} \\ n_0 &= \frac{n_{\text{amb}}}{1 \text{ cm}^{-3}} & \Delta t_3 &= \frac{\Delta t_{\text{sn}}}{10^3 \text{ yr}} \end{aligned} .$$

In this "free expansion" phase the energy released by the SN explosion is contained primarily in the kinetic energy of the ejecta. The velocity profile $v(r) = (r/R_{\text{sn}})v_{\text{max}}$ increases linearly from the center at $r = 0$ to the outer edge of the remnant at R_{sn} . By volume integrating the kinetic energy density of ejecta $(1/2)\rho v^2$ and setting it equal to the total SN energy

$$E_{\text{sn}} = \int_0^{R_{\text{sn}}} \frac{1}{2} \rho_{\text{sn}} v_{\text{sn}}^2 \left(\frac{r}{R_{\text{sn}}} \right)^2 4\pi r^2 dr \quad (5.6)$$

we can solve for the maximum velocity at the outer edge

$$\begin{aligned} v_{\text{max}} &= \sqrt{\frac{10}{3} \left(\frac{E_{\text{sn}}}{M_{\text{sn}}} \right)} \\ &\approx 13000 \text{ km/s} \left(\frac{E_{51}}{M_0} \right)^{1/2} \end{aligned} \quad (5.7)$$

and the mass-averaged velocity

$$\begin{aligned} v_{\text{sn}} &= \sqrt{\frac{2E_{\text{sn}}}{M_{\text{sn}}}} \\ &= 10000 \text{ km/s} \left(\frac{E_{51}}{M_0} \right)^{1/2} \end{aligned} . \quad (5.8)$$

The initial momentum $M_{\text{sn}}v_{\text{sn}}$ of the SN remnant is

$$\begin{aligned} p_{\text{sn}} &= \sqrt{2E_{\text{sn}}M_{\text{sn}}} \\ &= 10000 M_{\odot} \text{ km/s} (E_{51}M_0)^{1/2} \end{aligned} . \quad (5.9)$$

5.1.3.2 Sedov-Taylor blast wave

The radius of freely expanding SN ejecta grows with approximately constant velocity until it has swept up a volume of ambient gas with a mass equivalent to the initial ejecta mass. This happens when the SN remnant has expanded to a radius

$$R_{\text{st}} = \left(\frac{3M_{\text{sn}}}{4\pi\rho_{\text{amb}}} \right)^{1/3} \approx 2.1 \text{ pc} \left(\frac{M_0}{n_0} \right)^{1/3} \quad (5.10)$$

after a time

$$t_{\text{st}} = \frac{R_{\text{st}}}{v_{\text{sn}}} \approx 210 \text{ yr} M_0^{5/6} E_{51}^{-1/2} n_0^{-1/3} \quad (5.11)$$

The average density of ejecta bounded by the swept up gas at this radius falls below the initial ambient density. The pressure in the shocked ambient gas grows higher than the internal pressure of the blast wave, driving a reverse shock back into the interior and super-heating the ejecta to extremely high temperatures 10^8 – 10^9 K. If we assume that the injected momentum is conserved then the average shell velocity drops by half when an equivalent mass has been swept up. Energy conservation tells us that about half of the initial kinetic energy is available to be converted into thermal energy of the low density ejecta upstream of the shock front. The change in gravitational potential energy of the expanding remnant and radiative losses from heated gas in the low density interior are negligible compared to the initial kinetic energy.

The time dependent evolution of the hot ejecta can be modeled as a point explosion if we neglect the ambient pressure and radiative losses. The expansion of the SN remnant in this stage must conserve the initial explosion energy. The shock radius is proportional to powers of the thermal energy, ambient density, and time

$$R_{\text{shock}} = A E^{1/5} \rho^{-1/5} t^{2/5} \quad (5.12)$$

with exponents determined by dimensional analysis of mass, length, and time units (Draine, 2011, their equations 39.5-7). The self-similar numerical solution, with $A = 1.15167$, was originally developed independently by Taylor (1950) and Sedov (1959) for a finite energy

explosion. This energy-conserving stage of SN remnant evolution is known as the Sedov-Taylor (ST) phase. Using appropriate astrophysical units, and scaling the time as $t_3 = t/10^3$ yr, the time-dependent evolution of the shock radius is

$$R_{\text{shock}} \approx 5 \text{ pc} \left(\frac{E_{51}}{n_0} \right)^{1/5} t_3^{2/5} . \quad (5.13)$$

If we take the derivative of R_{shock} with respect to time we obtain the shock velocity

$$\begin{aligned} v_{\text{shock}} &= \frac{d}{dt} R_{\text{shock}} \\ &\approx 2100 \text{ km/s} \left(\frac{E_{51}}{n_0} \right)^{1/5} t_3^{-3/5} . \end{aligned} \quad (5.14)$$

Using equation 5.13 we can calculate the swept up mass $M_{\text{shock}} = (4\pi/3)\rho_{\text{amb}}R_{\text{shock}}^3$, and by multiplying with equation 5.14 we can estimate the momentum of gas that has been swept up by the blast wave

$$\begin{aligned} p_{\text{shock}} &= \frac{4\pi}{3} R_{\text{shock}}^3 \rho_{\text{amb}} v_{\text{shock}} \\ &\approx 32500 M_{\odot} \text{ km/s} E_{51}^{4/5} n_0^{1/5} t_3^{3/5} \end{aligned} \quad (5.15)$$

The ST solution neglects the mass of ejecta and swept up material that are present prior to the phase transition. Nonetheless, if the environment is sufficiently uniform far from the injection site, the physical hydrodynamic solution evolves towards the numerical ST solution (Draine, 2011).

5.1.3.3 Snowplow Shell

So far we have neglected radiative cooling in the hot ejecta. The interior of the bubble is very hot but has such low density that it does not cool efficiently since the cooling rate scales as $\Lambda \propto n^2$. The turbulent internal pressure of the bubble forces most of the ejecta mass to pile up on the inner edge of the swept up gas, just behind the forward shock. Eventually the deposited layer of hot ejecta becomes dense enough that radiative cooling is no longer negligible. When the total energy lost to radiative cooling becomes significant compared to the original explosion energy, the thermal pressure of the cooled ejecta layer just behind the shock drops. The forward shock expansion stalls and the shocked ejecta layer is compressed into a thin shell of cold dense gas. By volume integrating the cooling

function using the density and temperature profiles from the numerical Sedov-Taylor solution, Draine (2011) calculates a thin shell formation time that is equal to the characteristic radiative cooling time

$$t_{\text{rad}} = \frac{1}{3} \frac{E_{\text{sn}}}{\dot{E}} \approx 50 \text{ kyr} E_{51}^{0.22} n_0^{-0.55} . \quad (5.16)$$

The radius, velocity, and momentum of the thin shell are estimated from the ST solution at $t = t_{\text{rad}}$

$$R_{\text{rad}} = R_{\text{shock}}(t_{\text{rad}}) \approx 26 \text{ pc} E_{51}^{0.29} n_0^{-0.42} \quad (5.17)$$

$$v_{\text{rad}} = v_{\text{shock}}(t_{\text{rad}}) \approx 200 \text{ km/s} E_{51}^{0.07} n_0^{0.13} \quad (5.18)$$

$$p_{\text{rad}} = \frac{4\pi}{3} \rho_{\text{amb}} R_{\text{rad}}^3 v_{\text{rad}} \approx 3.4 \times 10^5 M_{\odot} \text{ km/s} E_{51}^{0.93} n_0^{-0.13} . \quad (5.19)$$

Although the forward shock briefly stalls when the thin shell loses thermal pressure, the bubble continues to expand adiabatically due to the thermal pressure exerted on the thin shell by the hot, low density interior where cooling remains negligible. The SN remnant leaves the Sedov-Taylor phase and enters the snowplow phase, so named because the thin shell continues to sweep up the ambient medium like a snowplow. Because radiative cooling is unimportant, the hot interior of the pressure-driven snowplow (PDS) can only cool adiabatically with expansion such that PV^{γ} remains constant. The internal pressure of the PDS bubble scales with the snowplow radius $P_{\text{pds}} \propto R_{\text{pds}}^{-3\gamma}$. If we assume $\gamma = 5/3$, then

$$P_{\text{pds}} = P_{\text{rad}} \left(\frac{R_{\text{rad}}}{R_{\text{pds}}} \right)^5 \quad (5.20)$$

where P_{rad} is the remaining pressure in the hot bubble interior after the thin shell cools at t_{rad} . The internal pressure exerts a force on the thin shell

$$\frac{d}{dt} (M_{\text{shock}} v_{\text{shock}}) \approx 4\pi P_{\text{pds}} R_{\text{pds}}^2 \approx 4\pi P_{\text{rad}} R_{\text{rad}}^5 R_{\text{pds}}^{-3} \quad (5.21)$$

that drives the snowplow expansion. The left hand side of equation 5.21 has units of mass, which scales $\propto R_{\text{pds}}^3$, times acceleration, which scales as R_{pds}/t^2 . If we assume that the snowplow radius evolves as some power of time $R_{\text{pds}} \propto t^\eta$, then by dimensional analysis of time on the left and right-hand sides of equation 5.21 ($4\eta - 2 = -3\eta$) we require $\eta = 2/7$ (see Draine, 2011, chapter 39.1.3). For $t > t_{\text{rad}}$, the PDS radius evolves as

$$\begin{aligned} R_{\text{pds}} &= R_{\text{rad}} \left(\frac{t}{t_{\text{rad}}} \right)^{2/7} \\ &\approx 16 \text{ pc } E_{51}^{0.23} n_0^{-0.26} t_4^{2/7} \end{aligned} \quad (5.22)$$

and PDS velocity as

$$\begin{aligned} v_{\text{pds}} &= \frac{d}{dt} R_{\text{pds}} \\ &\approx 450 \text{ km/s } E_{51}^{0.23} n_0^{-0.26} t_4^{-5/7} \end{aligned} \quad (5.23)$$

using the time scaling factor $t_4 = t/10^4$ yr. Note that the shock stalls at t_{rad} and the velocity immediately afterwards $v_{\text{pds}}(t_{\text{rad}})$ is less than v_{rad} by 30%.

5.1.3.4 Overlapping Supernova Remnants

If the delay time between SNe in a compact star cluster is short compared to the time at which radiative losses become important for a single SN, i.e. $\Delta t_{\text{sn}} \ll t_{\text{rad}}$, subsequent SNe that occur within the bubble will inject energy into it faster than can be radiated away and the pre-existing ST phase of the first SN is extended. In this limit the mechanical luminosity is approximated as $L_{\text{sn}} = E_{\text{sn}}/\Delta t_{\text{sn}}$. We replace the finite explosion energy E_{sn} with the time-dependent total energy of the SB $L_{\text{sn}}t = E_{\text{sn}}(t/\Delta t_{\text{sn}})$ in equations 5.13 and 5.14 in order to obtain the solution for a bubble with constant energy injection (Kim, Ostriker & Raileanu, 2017). The energy-conserving phase of a continuously powered hot bubble evolves much like the ST phase of a single SN with numerical coefficient $A = 0.88$ (Weaver et al., 1977), until radiative losses cause the swept up ISM to collapse into a thin shell at a much later time

$$t_{\text{rad,cont}} \approx 150 \text{ kyr} \left(\frac{E_{51}}{\Delta t_3} \right)^{0.28} n_0^{-0.71} . \quad (5.24)$$

The radius and velocity of the forward shock during the energy-conserving phase, assuming continuous energy injection, are

$$R_{\text{shock,cont}} \approx 16 \text{ pc} \left(\frac{E_{51}}{n_0 \Delta t_3} \right)^{1/5} t_4^{3/5} \quad (5.25)$$

$$v_{\text{shock,cont}} \approx 952 \text{ km/s} \left(\frac{E_{51}}{n_0 \Delta t_3} \right)^{1/5} t_4^{-2/5} . \quad (5.26)$$

We obtain an estimate for the radius and velocity of the continuously powered shock when radiative losses become significant by evaluating equations 5.25 and 5.26 at $t_{\text{rad,cont}}$

$$R_{\text{rad,cont}} \approx 82 \text{ pc} \left(\frac{E_{51}}{\Delta t_3} \right)^{0.37} n_0^{-0.62} \quad (5.27)$$

$$v_{\text{rad,cont}} \approx 322 \text{ km/s} \left(\frac{E_{51}}{\Delta t_3} \right)^{0.09} n_0^{0.08} . \quad (5.28)$$

As in the case of a single SN at t_{rad} , the forward shock stalls temporarily at $t_{\text{rad,cont}}$ while the contact discontinuity separating the hot bubble and the cold swept up gas catches up and collapses it into a thin shell. For a single SN the finite pressure remaining in the hot bubble interior decreases as it pushes out on the snowplow shell and the time-dependence of the shock radius changes from $\propto t^{2/5}$ (equation 5.13) to $\propto t^{2/7}$ (equation 5.22). By contrast, the internal energy of the continuously powered hot bubble keeps increasing through time and the shock continues to expand with the same parameter dependence as in the energy-conserving phase, but with a decreased numerical coefficient $A = 0.76$ that accounts for the momentary stall (Weaver et al., 1977). The continuous snowplow has radius and velocity

$$R_{\text{pds,cont}} \approx 56 \text{ pc} \left(\frac{E_{51}}{n_0 \Delta t_3} \right)^{1/5} t_5^{3/5} \quad (5.29)$$

$$v_{\text{pds,cont}} \approx 327 \text{ km/s} \left(\frac{E_{51}}{n_0 \Delta t_3} \right)^{1/5} t_5^{-2/5} \quad (5.30)$$

where we have again increased the unit scaling factor for time $t_5 = t/10^5 \text{ yr}$ to reflect the typical scale for $t_{\text{rad,cont}}$. Just as in the case for a single SN, the continuous energy injection shock stalls at $t_{\text{rad,cont}}$, but the velocity immediately afterwards $v_{\text{pds,cont}}(t_{\text{rad,cont}})$ is less than $v_{\text{rad,cont}}$ by only about 15%.

If Δt_{sn} is greater than t_{rad} , however, the first SN remnant evolves as it would in isolation and a thin dense shell is formed when it becomes a standard pressure-driven snowplow. The next SN that explodes within the SB freely expands into the back of the existing snowplow

and a reverse shock immediately rebounds back into and reheats the interior. The thin shell quickly radiates away thermal energy from the new material condensed onto it, bypassing the ST phase and reinvigorating the snowplow. At later times $t \gtrsim 2\Delta t_{\text{sn}}$, the combined shock quickly evolves towards the continuously powered PDS solution.

5.1.3.5 Superbubble Breakout

By inverting equation 5.29 and solving for t we can estimate the time it takes for the continuous PDS to reach the edge of the disk at scale height H

$$t_{\text{pds}}(H) \approx 265 \text{ kyr} \left(\frac{n_0 \Delta t_3 H_2^5}{E_{51}} \right)^{1/3} \quad (5.31)$$

with $H_2 = H/100 \text{ pc}$. During that time, the number of SNe to occur is approximately

$$N_{\text{sn}} \approx \frac{t_{\text{pds}}(H)}{\Delta t_{\text{sn}}} \approx 265 \left(\frac{n_0 H_2^5}{E_{51} \Delta t_3^2} \right)^{1/3} . \quad (5.32)$$

The velocity of the continuous PDS shell when it breaks out through the edge of the disk is

$$v_{\text{pds,cont}}(t_{\text{pds}}(H)) = 222 \text{ km/s} \left(\frac{E_{51}}{n_0 \Delta t_3 H_2^2} \right)^{1/3} . \quad (5.33)$$

In very active starburst galaxies where Δt_{sn} is sufficiently small, the shock can breach the face of the disk before the thin shell radiates away most of the energy. If we set $R_{\text{rad,cont}} = H$ in equation 5.27 and solve for Δt_{sn} , we obtain the maximum SN interval which is consistent with this hot breakout condition

$$\Delta t_{\text{sn,hot}} < 592 \text{ yr} E_{51} n_0^{-1.7} H_2^{-2.7} . \quad (5.34)$$

The SB within the disk region remains perpetually in the energy-conserving ST phase until after it breaks out and the continuous energy injection limit is a good approximation at all times because $\Delta t_{\text{sn,hot}} < t_{\text{rad}}$. This condition requires low ambient density and a high frequency of SNe (Kim, Ostriker & Raileanu, 2017).

For a more modest starburst with less frequent SNe, or in a higher density background, the SB will transition into the snowplow phase before it breaks out of the disk. The momentum-conserving snowplow shell gradually slows down as it sweeps up mass. The snowplow must break out of the disk before its velocity fades away into the background

turbulent velocity dispersion σ . If we set the snowplow expansion velocity, equation 5.30, equal to σ we can estimate the time when this occurs

$$t_{\text{fade}} \approx 1.9 \text{ Myr} \left(\frac{E_{51}}{n_0 \Delta t_3 \sigma_2^5} \right)^{1/2} . \quad (5.35)$$

where we have scaled the background velocity $\sigma_2 = \sigma/100 \text{ km/s}$. The upper limit for the SN interval in this cold breakout condition is found by setting the continuous PDS breakout velocity, equation 5.33, equal to σ and solving for Δt_{sn}

$$\Delta t_{\text{sn,cold}} < 10.9 \text{ kyr} \left(\frac{E_{51}}{n_0 H_2^2 \sigma_2^3} \right) . \quad (5.36)$$

The conditions of the ISM near the galactic center change drastically after multiple SN explosions have swept up the surrounding gas and removed it from the galactic disk. Here we assume that clustered SNe have swept up the gas within a sphere of radius H equal to the disk scale height. The background density decreases rapidly as $\rho_{\text{amb}} \propto r^{-2}$ outside of the disk. After the SB reaches the vertical edge of the disk, the shock accelerates through the density gradient away from the plane of the disk. By this time we can no longer assume spherical symmetry and the accelerated shell is eventually disrupted and fragmented by hydrodynamical instabilities (e.g. Vishniac, 1994). The cold, dense cloud fragments from the snowplow shell are located at the head of a tenuous hot bubble that leaks out into the halo through gaps between the fragments. The cavity carved out of the disk by the fragmented shell has a very low ambient density so that young SN remnants remain in the free expansion phase much longer and a large fraction of the bubble volume is reheated when they transition to the ST phase. These conditions reproduce the basic assumptions for the two phase medium used in analytical wind models.

5.1.4 Hot Winds in the First Galaxy

Analytical models (e.g. Chevalier & Clegg, 1985) provide self-similar solutions for an adiabatic, galactic-scale wind powered by a central hot bubble. The models assume mass and thermal energy, e.g. from SNe or stellar winds, are continuously injected within an unresolved volume of radius R_{inj} around a star cluster at the center of a gaseous galactic disk. Mass is added uniformly over the volume $r < R_{\text{inj}}$ with a total rate $\dot{M}_{\text{inj}} = M_{\text{sn}}/\Delta t_{\text{sn}}$. Likewise, energy is added uniformly over the same volume with rate $\dot{E}_{\text{inj}} = E_{\text{sn}}/\Delta t_{\text{sn}}$. The steady-state solution for $r > R_{\text{inj}}$ depends on the boundary conditions at R_{inj} , corresponding

to the uniform density and temperature of the bubble. If we assume that the turbulent velocity inside the bubble is similar to the sound speed, and that the gas cools adiabatically as it expands outside the bubble, then the outflow becomes supersonic after crossing the sonic point at R_{inj} . The conditions downstream in the supersonic outflow are dynamically decoupled from the subsonic interior. It is generally assumed that the gas around the injection region was modified during an earlier epoch which created a distinct two phase medium with cold dense gas embedded in the tenuous hot wind.

Heckman & Thompson (2017) summarize classical analytical hot wind models in their review. The outflows are parameterized using α , the energy-loading or thermalization parameter, and β , the mass-loading parameter. The energy-loading parameter is defined in terms of the internal energy of the wind $\dot{E}_{\text{wind}} = \alpha E_{\text{sn}} / \Delta t_{\text{sn}}$ and has typical values $\alpha \lesssim 0.1$. The mass-loading parameter is defined in terms of the ratio of the mass outflow rate to the star formation rate (SFR), or $\dot{M}_{\text{wind}} = \beta \dot{M}_{\star}$. These parameters assume that mass is injected proportionally to the local SFR \dot{M}_{\star} ($M_{\odot} \text{ yr}^{-1}$), which can be estimated with a Kennicutt-Schmidt law, e.g. $\Sigma_{\text{SFR}} \propto \Sigma_{\text{gas}}^{1.4}$ ($M_{\odot} \text{ pc}^{-2} \text{ yr}^{-1}$). We can expect about 1–2 SN per $100 M_{\odot}$ of stars formed with a power-law IMF (e.g. Salpeter, 1955). A mass-loading parameter of $\beta = 0.25$ is expected solely due to the continuous ejection of SNe and stellar winds (Leitherer et al., 1999), with higher values due to swept up gas entrained in the wind. Values of $\beta > 1$ imply that more mass is being driven out of the galaxy than is forming new stars. Limits on α and β in starburst galaxies have been inferred from X-ray observations (Strickland & Heckman, 2009; Zhang et al., 2014). Using these parameters, the asymptotic velocity of the hot wind is

$$v_{\text{hot}} = \left(\frac{2\dot{E}_{\text{wind}}}{\dot{M}_{\text{wind}}} \right)^{1/2} \approx 1000 \text{ km/s} \left(\frac{\alpha}{\beta} \right)^{1/2}. \quad (5.37)$$

Bernoulli's equation

$$B = \frac{1}{2}v^2 + \frac{3}{2}c_s^2 \quad (5.38)$$

can be evaluated at the sonic point using the homogeneous conditions of the interior and remains constant at $r = \infty$, giving the hot wind temperature

$$T_{\text{hot}} \propto \frac{m_{\text{H}} v_{\text{hot}}^2}{k_{\text{B}}} \approx 2 \times 10^7 \text{ K} \left(\frac{\alpha}{\beta} \right) . \quad (5.39)$$

5.2 Numerical Methods

The goal of our numerical simulation is to replicate the physical impact of sustained radiative and SN feedback by a stellar cluster on a realistic host galaxy in the early universe. Simulating *ab initio* galaxy formation is beyond the scope of this study, thus we chose to instantiate our host galaxy by mapping the output from the cosmological smoothed particle hydrodynamics (SPH) simulation of Pawlik, Milosavljević & Bromm (2013b). An instantaneous starburst is assumed to have formed a stellar cluster at the center of the host galaxy at the beginning of our simulation. We immediately begin radiative feedback by modeling the cluster as a point source. Supernova feedback is delayed for a few million years until the death of the most massive star. Our desire was to model the direct injection of momentum by SNe using blast waves initiated in the free expansion phase with pure kinetic energy, thereby avoiding the common problems faced when modeling SNe with pure thermal energy. The kinetic energy approach requires much more fine-grained control of the spatial resolution, both for maintaining the quasi-spherical shape of blast wave, as well as for capturing small-scale hydrodynamic features within the expanding shocks.

To achieve these goals we must simultaneously resolve a high dynamic range in length scales, whether inserting a spherical blast wave with radius ~ 1 pc, or following a galactic wind launched into the IGM over 3 kpc away from the stellar cluster. We chose to use a Cartesian grid-based adaptive mesh refinement (AMR) code in order to maintain dynamic control over the spatial scales being resolved, as well as to limit unwanted diffusivity in shock contact discontinuities. Using AMR we can zoom in to an arbitrary point and resolve small-scale hydrodynamic features as fine as $\Delta x \sim 0.01$ pc within the individual SN blast waves. We can then dynamically lower the refinement around SN remnants as they expand, ensuring that the diameter of individual remnants are resolved by at least 128 cells, decreasing the resolution by a factor of 2 when their diameter exceeds 256 cells. The remnants will overlap with one another to form a SB that climbs up the gravitational potential

well and out of the host galaxy. The volume swept up by the combined SB is maintained at a minimum resolution of $\Delta x \sim 11$ pc, extending past the virial radius into the IGM as the outflow escapes the galaxy. All numerical quantities mentioned in this work are in physical units, unless otherwise noted as comoving.

5.2.1 FLASH Configuration

We used the FLASH hydrodynamics code (Fryxell et al., 2000) with the PARAMESH parallel AMR grid scheme (MacNeice & Center., 1999) operating in 3D. The AMR grid was organized into cube-shaped blocks, each containing $8^3 = 64$ cube-shaped cells. Dark matter particles were advanced in time using the leapfrog cosmology method for active particles with cosmological parameters from (Planck Collaboration et al., 2016, table 4). The combined self-gravity of gas and dark matter was calculated using the multi-grid approach of Ricker (2008) with periodic boundaries. Force-softening of gravity acting on dark matter particles in highly refined regions is achieved by calculating the force using the potential mapped onto parent AMR blocks at lower resolution, where cell sizes are large enough to match the softening length (Safranek-Shrader, Milosavljević & Bromm, 2014a).

Scalar quantities were advected on the AMR grid using the directionally split Piecewise Parabolic Method (PPM) of Colella & Woodward (1984). The primordial chemical species (H, H⁺, e⁻, He, He⁺, He⁺⁺) were individually stored on the grid as mass scalars using a total helium abundance of 0.08. All chemical species with mass greater than helium were aggregated into a single metallicity mass scalar Z , which assumed fixed carbon and oxygen enhanced abundance ratios ($[C/H] = -3.61$ and $[O/H] = -3.3$). The Consistent Multi-fluid Advection method (Plewa & Müller, 1999) was used to modify PPM for multiple species advection.

We enabled the hybrid Riemann solver for PPM which uses the method of Colella & Glaz (1985) by default and switches to the HLLC method (Einfeldt, 1988) to prevent numerical instabilities when strong shocks are detected. The *eintSwitch* parameter was set to 10^{-4} which allowed the internal energy to be calculated by subtracting the kinetic energy from the total energy in cases where the kinetic energy dominates, such as in a SN shock. The internal energy is stored as a scalar and advected directly on the grid, rather than calculated by subtraction, whenever it is greater than *eintSwitch* times the kinetic energy such as in photoheated gas.

5.2.2 Initial Conditions

The host galaxy in our simulation was constructed by extracting SPH dark matter and gas particles from within a 1 Mpc^3 (comoving) box centered on the most massive halo in the final output of Pawlik, Milosavljević & Bromm (2013b, NOFB simulation). Dark matter particles were loaded directly into the simulation as active particles. Gas particles were mapped onto the AMR grid with a parallel algorithm employing the same kernel used by the GADGET-2 SPH code (Springel, 2005).

5.2.2.1 Resolving SPH Particles in AMR

The grid hierarchy was initialized by adaptively refining around overdensities in the mapped gas distribution. We identified an overdensity in any cell at refinement level ℓ that had a comoving mass density $\tilde{\rho}$ greater than a maximum threshold density

$$\tilde{\rho}_{\text{max}} = 3\tilde{\rho}_b 2^{3(\ell-\ell_0)(1+\phi)} \quad (5.40)$$

where $\ell_0 = -3.95$ is the initial refinement level offset, $\phi = -0.3$ is the Lagrangian refinement factor, and $\tilde{\rho}_b = 3H(z)^2\Omega_b/8\pi G$ is the mean comoving baryonic density of the universe (Safranek-Shrader et al., 2012). The grid cell spacing Δx for any given refinement level ℓ is

$$\Delta x = 2^{-(\ell+2)} \frac{1 \text{ Mpc}}{1+z} \quad (5.41)$$

in physical units.

The particle mapping and refinement procedures were iterated several times in order to ensure that the densest particles with the shortest smoothing lengths were sufficiently resolved. An initial mapping was performed on the coarse grid which was then iteratively refined until no more blocks contained overdensities. We then remapped the gas onto the more highly refined grid and repeated the refinement procedure. This cycle lasted for 10 rounds before the final mapping was made on the fully resolved grid that contained no overdensities. The gas particles were removed from the simulation after the final round of mapping.

5.2.2.2 The Simulated Galaxy

Our simulation begins at redshift $z = 10$ inside a $10^9 M_\odot$ dark matter atomic cooling halo with virial radius 3 kpc . There was $10^8 M_\odot$ of gas within the virial radius with a surface

density $\Sigma_{\text{gal}} = 3.5 M_{\odot} \text{pc}^{-2}$. Almost half of that gas was contained in a thin disk at the center of the host galaxy with a surface density $\Sigma_{\text{disk}} = 255 M_{\odot} \text{pc}^{-2}$. The galactic disk had spiral arms that reached as far out as 250 pc. The spiral arms converged into a bar with diameter 10 pc at the center of the disk. The source SPH simulation also contained a spheroidal bulge component from star particles concentrated at the center of the disk. These were mapped as gas particles in our simulation using an assumed temperature of 10^4K . The maximum gas density within the inner $\sim 30 \text{pc}$ was capped at 10^3cm^{-3} after the final mapping to account for the mass attributed to a newly formed star cluster, as well as to ensure that the surrounding gas could be fully ionized by Lyman continuum radiation.

5.2.3 Stellar Feedback

Within the central gas disk we modeled the emission of hydrogen-ionizing Lyman continuum (LyC) photons by a $10^5 M_{\odot}$ stellar cluster. Basic properties for the metal-poor PopII cluster were calculated using a STARBURST99 model (Leitherer et al., 1999) with metallicity $Z_{\text{PopII}} = 0.05 Z_{\odot}$, assuming the canonical value of $Z_{\odot} = 0.02$. The model's IMF used a single exponent power-law with $\alpha = 2.3$ between 1 and $100 M_{\odot}$. The emission of ionizing photons by the cluster of massive O and B type stars proceeded at an approximately constant rate for several million years, until the most massive stars began to explode as SNe. We used a constant value of $Q_{\text{LyC}} = 10^{51}$ photons per second from a point source at the center of the cluster.

5.2.3.1 The Strömgren Sphere

Initially the Strömgren radius just barely reached the edge of the bar with density 10^3cm^{-3} at the center of the gaseous disk and this approximation was only valid within $R_S \approx 5 \text{pc}$. Intense heating near the point source lowered the density over time as we show in section 5.3.1. Once the Strömgren radius breached the face of the disk, the low density gas in the host galaxy halo was quickly ionized. The spherically-averaged Strömgren radius grew to $R_S \approx 20 \text{pc}$ after only a few hundred thousand years when the density near the point source drops to $\sim 10^2 \text{cm}^{-3}$, large enough to encompass the additional bulge of mass from the SPH star particles that were mapped on top of the gaseous bar. After a few million years the average density in the disk dropped to $\sim 10 \text{cm}^{-3}$ and the Strömgren radius was $R_S \sim 100 \text{pc}$, large enough to ionize the entire disk and the rest of the host galaxy halo.

5.2.3.2 The Ionization Parameter

In the absence of shock heating, the equilibrium temperature of a gas cloud due to photo-ionization alone can be parameterized using the ionization parameter U , which encodes the incident spectral flux and cloud density into a single homologous relationship for the temperature and ionization state of a cloud. The ionization parameter is the dimensionless ratio of the number of ionizing photons to the number of hydrogen nuclei. It can be written in terms of the flux of ionizing photons passing through the cloud's surface, the hydrogen number density at the surface, and the speed of light c (Osterbrock & Ferland, 2006).

$$U = \frac{F_{\text{LyC}}}{n_{\text{H}}c} \quad (5.42)$$

To save computational cost we modeled the LyC flux incident upon a cell located at a distance r from the point source as

$$F_{\text{LyC}} = \frac{Q_{\text{LyC}}}{4\pi r^2} \quad (5.43)$$

which assumes no attenuation of Q_{LyC} by intermediate dense clouds. This is a poor assumption at the beginning of our simulation when the ionizing photons are bottled up near the source, however once the Strömngren radius breaks out of the core of the gas disk, the exterior is optically thin and the assumption becomes valid. For each cell in our simulation with number density n_{cell} at a distance r_{cell} from the stellar cluster, we calculate the modified ionization parameter

$$\xi_{\text{cell}} = \frac{Q_{\text{LyC}}}{4\pi r_{\text{cell}}^2 n_{\text{cell}}} \quad (5.44)$$

with the speed of light constant c factored out.

5.2.3.3 Photo-ionization Heating

The equilibrium temperature and ionization state were tabulated as a function of the modified ionization parameter ξ_{cell} and the absolute metallicity Z_{cell} using the CLOUDY radiative transfer modeling code (Ferland et al., 2013). The input spectrum was loaded directly into CLOUDY from the STARBURST99 model. The radiative model used the same fixed elemental abundance ratios used in FLASH (e.g. $[\text{C}/\text{H}] = -3.61$ and $[\text{O}/\text{H}] = -3.3$), using the mass fraction Z_{cell} to scale metallicity. The tabulated data was linearly interpolated between log-spaced grid points for the particular input values ξ_{cell} and Z_{cell} . The current temperature and ionization state in the cell was replaced with the interpolated equilibrium temperature and ionization state, and the equation of state was recomputed.

5.2.4 Supernova Feedback

After photo-heating for 3.25 Myr, the lifetime of a $\sim 100M_{\odot}$ star, we zoom in to high resolution and insert the first SN remnant in the free expansion phase. The cadence of SN progenitor masses was selected from our STARBURST99 model. The SN rate (yr^{-1}) was integrated with respect to time. We recorded the cumulative time and number of SNe along with the typical progenitor masses in each time interval. The number of SNe, as functions of time and of mass, were interpolated and the axes inverted to get the time and the mass as a function of the number of SNe. We then recorded the delay time and progenitor mass from the interpolated functions for each of the first 100 whole-numbered SNe.

5.2.4.1 Supernova Remnant Model

The delay time between each SN was consistently between 60 kyr and 70 kyr. We chose to use a constant delay time equal to the average $\Delta t_{\text{sn}} = 66$ kyr. The SN remnant masses, calculated by subtracting the compact remnant mass (Fryer et al., 2012) from the progenitor mass, vary gradually from $100M_{\odot}$ down to about $33M_{\odot}$ then increase suddenly for progenitors with masses less than $33M_{\odot}$. A fixed SN remnant mass $M_{\text{sn}} = 12M_{\odot}$ was chosen as the average of the first 100 SN remnant masses. Each SN remnant is imparted with the canonical value $E_{\text{sn}} = 10^{51}$ erg of kinetic energy, implying a mechanical luminosity of $E_{\text{sn}}/\Delta t_{\text{sn}} = 5 \times 10^{38} \text{ erg s}^{-1}$. Direct comparison with analytical models was made simpler by choosing constant values for M_{sn} , E_{sn} , and Δt_{sn} .

One of the primary goals of this simulation is to model the direct injection of momentum into the surrounding gas by zooming in to insert SN remnants in the free expansion phase with pure kinetic energy. The initial radius for each SN remnant

$$R_{\text{sn}} = \frac{1}{10} \left(\frac{3M_{\text{sn}}}{4\pi\rho_{\text{amb}}} \right)^{\frac{1}{3}} \quad (5.45)$$

is chosen to be a tenth of the radius at which the swept up mass equals the ejected mass in order to ensure that the remnants are initialized before they transition into the Sedov-Taylor phase. This naturally sets the initial density of the remnant to ten times the local ambient density. The SN remnant radius was $R_{\text{sn}} \approx 1$ pc when the ambient number density was $\sim \rho_{\text{amb}}/m_{\text{H}} \approx 10 \text{ cm}^{-3}$.

Each remnant is instantiated with a linear velocity profile

$$v(r) = \frac{r}{R_{\text{sn}}} v_{\text{max}} \quad (5.46)$$

increasing from 0 at the center to v_{\max} at R_{sn} . Our choice to use a constant M_{sn} and E_{sn} for all SNe also implies a constant $v_{\max} = 3727 \text{ km/s}$ and $v_{\text{sn}} = 2887 \text{ km/s}$, about 1% of the speed of light. The total momentum injected by each SN was $p_{\text{sn}} = 3.5 \times 10^4 M_{\odot} \text{ km/s}$ and the momentum injection rate was $p_{\text{sn}}/\Delta t_{\text{sn}} = 0.5 M_{\odot} \text{ km/s yr}^{-1}$. The flow of ejecta is followed using 10^6 passive Lagrangian tracer particles per SN remnant. The particles are evenly distributed in the initially spherical ejecta, with particle density proportional to the gas density.

5.2.4.2 Dynamic Resolution Control

The insertion of a new SN was triggered after the delay time Δt_{sn} had passed since the most recent SN. For each new SN, a set of 3 random numbers (r , θ , and ϕ) were generated between $[0..1)$ and used to compute a set of random Cartesian coordinates within 10 pc of the center of the star cluster. The grid resolution was increased within a radius $3R_{\text{sn}}$ around the random coordinates so that the diameter of the SN remnant was resolved by a minimum of 128 cells. The grid refinement level l_{sn} required to achieve this grid resolution is

$$l_{\text{sn}} = \text{floor} \left(1 - \log_2 \tilde{R}_{\text{sn}} \right) + 4 \quad (5.47)$$

where $\tilde{R}_{\text{sn}} = R_{\text{sn}}(1+z)/1 \text{ Mpc}$ is the SN radius in units of comoving Mpc and the factor of 4 gives us $2^4 = 16$ blocks across the diameter (16 blocks \times 8 cells per block = 128 cells across). The first SN was refined at level $l_{\text{sn}} = 22$ with grid resolution $\Delta x = 0.005 \text{ pc}$.

Each time a remnant doubled in radius we degraded the grid resolution by a factor of 2 by stepping down the grid refinement level. We located the most distant tracer particle belonging to each SN remnant in order to determine the approximate current size of the remnant \mathcal{R}_{sn} . The grid refinement level desired for any particular SN remnant was the initial level minus the current step $l_{\text{sn}} - f_{\text{sn}}$, with the current step f_{sn} given by

$$f_{\text{sn}} = \text{floor} \left(1 + \log_2 \frac{\mathcal{R}_{\text{sn}}}{2R_{\text{sn}}} \right) . \quad (5.48)$$

After a step down in refinement, the refined region surrounding the remnant at new level $l_{\text{sn}} - f_{\text{sn}}$ is increased to $3 \times 2^{f_{\text{sn}}} R_{\text{sn}}$, or approximately $3\mathcal{R}_{\text{sn}}$. This ensures that the remnant can double in size from its current radius \mathcal{R}_{sn} to $2\mathcal{R}_{\text{sn}}$ at a constant grid resolution, with a buffer region out to $3\mathcal{R}_{\text{sn}}$ ensuring that the shocked ambient medium ahead of the shocked ejecta is also kept at the same resolution. The current grid refinement level for any particular block of 8^3 cells is chosen to be the maximum of the refinement level for any SN remnant i

within $3\mathcal{R}_i$ of any corner of the block. This ensures that overlapped remnants are resolved at the higher refinement level of the smallest remnant.

5.2.4.3 Cooling in Shock Heated Gas

Shock heated gas surrounding a SN remnant can reach temperatures in excess of 10^7 K. We allowed hot gas to cool radiatively in cells where the gas temperature was greater than the photo-ionization equilibrium temperature (see section 5.2.3.3). The volumetric cooling rate Λn_{H}^2 ($\text{erg s}^{-1} \text{ cm}^{-3}$) is computed by linearly interpolating Λ from a table of pre-computed values as a function of density, temperature, and metallicity (n_{H} , T , and Z), again using the CLOUDY code. The internal energy update was sub-cycled within a single time step by subtracting a fraction of the energy and recomputing the cooling rate and timescale. The cooling sub-cycle time step t_{sub} was taken to be one tenth of the cooling timescale

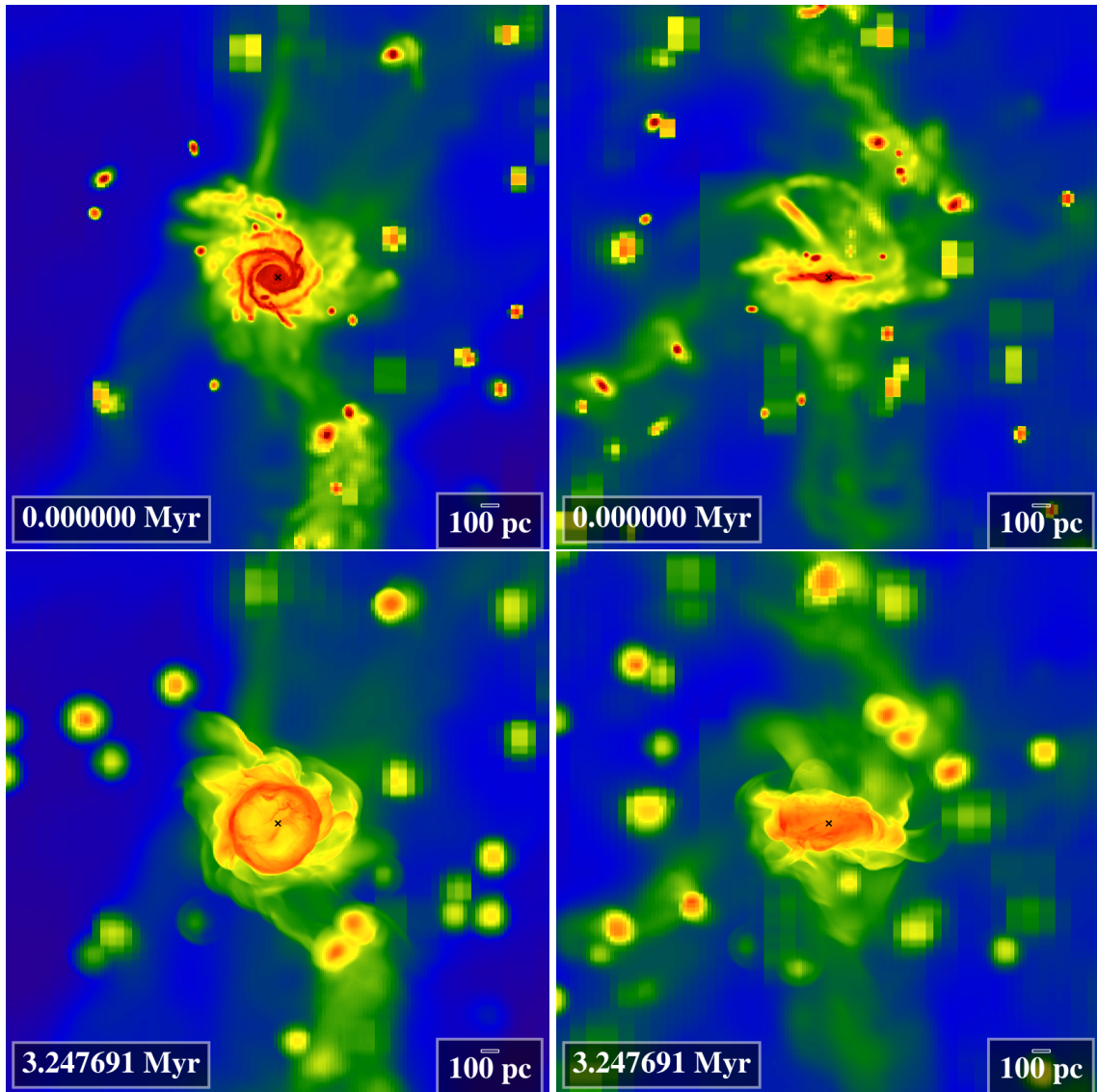
$$t_{\text{cool}} = \left| \frac{\rho E_{\text{int}}}{\Lambda n_{\text{H}}^2} \right| \quad (5.49)$$

where E_{int} is the internal energy density (per unit mass). The amount cooled per sub-cycle, $\Lambda n_{\text{H}}^2 t_{\text{sub}} / \rho$, is subtracted from the internal energy density and the new temperature was recomputed. Cooling for a single time step was finished if the cell temperature had cooled to the minimum photo-ionization equilibrium temperature, or if the sum of time spent sub-cycling equaled the full hydrodynamic time step.

5.3 Results

5.3.1 HII Region

For the first 3.25 Myr of our simulation, prior to the first SN, the only source of energy input was stellar radiation from the star cluster situated at the center of our host galaxy. Intense photo-heating caused a high pressure champagne flow that completely disrupted the gas disk in which the star cluster was embedded. The central gas bulge and spiral arms, seen in the upper left-hand side of figure 5.1a, were pushed outwards into a ring with diameter 500pc, roughly the same size as the initial disk.



(a) Face-on view

(b) Edge-on view

Figure 5.1: Face-on (*left column*) and edge-on (*right column*) projections of the density-weighted average number density (cm^{-3}) of the host galaxy disk before photoionization (*top row*), and after 3.25 Myr (*bottom row*). The black 'x' denotes the gravitational galactic center and location of the radiative point source. The virial radius at $R_{\text{virial}} = 3 \text{ kpc}$ is beyond the edge of these images. After photoionization, the thin host disk has been disrupted and the satellite halos are puffed up.

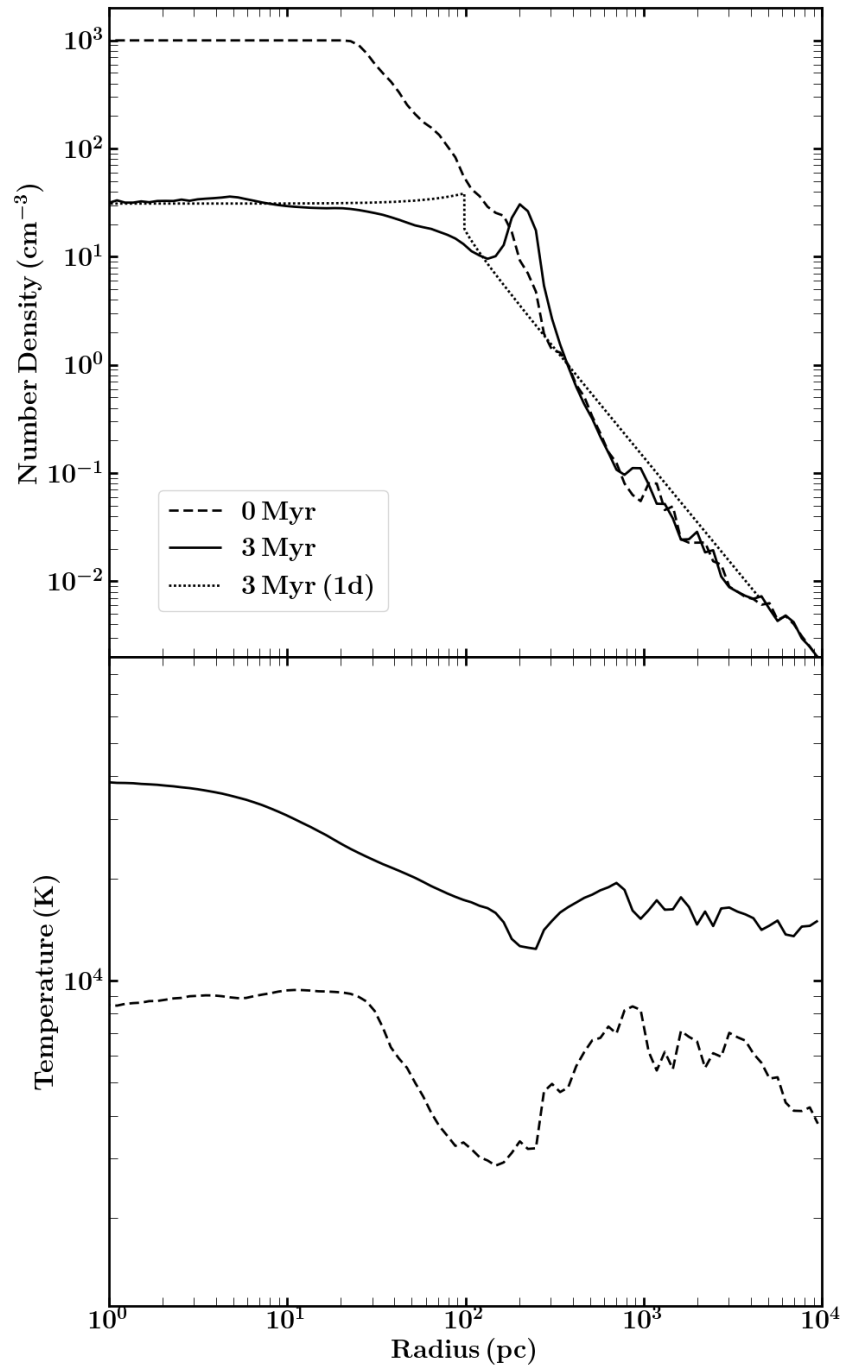


Figure 5.2: Radial profiles of the volume averaged density (top) and the mass averaged temperature (bottom) for photo-heated gas prior to the first SN explosion. Radial profiles are shown for $t = 0$ and 3 Myr after the initial starburst. The dotted line shows the 1d solution (Shu et al. 2002).

5.3.1.1 Disk Scale Height

The disk in our simulation was quite thin initially, as seen in the upper right-hand side of figure 5.1b, before it expanded under the influence of photo-heating. As a model, the disk can be thought of as roughly cylindrical with scale length L (radius) and scale height H (thickness). Roughly $4 \times 10^7 M_{\odot}$, or just under half of the total gas mass of the galaxy was contained within a distance 250 pc from the center of the disk in our simulation. Using this mass and radius in our model, the scale height for initial temperature $T_i = 9000$ K is 67 pc and the scale height after photo-heating to the central temperature $T_{\text{HII}} = 40000$ K is 300 pc. Careful inspection of line plots through the face of the disk confirm that the pressure scale height was initially 65 pc. This is in very good agreement with the model which is to be expected for a pressure supported disk. The disk expanded to 185 pc after photo-heating, quite a bit less than the model predicts. The model assumes a constant temperature however the temperature in the HII region decreases with distance from 40000 K near the point source to 20000 K just inside the thick shell at ~ 100 pc (figure 5.2, bottom panel). Using a temperature closer to the mass-averaged temperature within the disk, $T_{\text{HII}} = 25000$ K, we calculate a scale height $H = 188$ pc which agrees with the actual scale height of the disk in our simulation.

5.3.1.2 Self-similar Evolution of the Photoionized Shell

In the top panel of figure 5.2 we show the volume averaged density profiles within the HII region, prior to the first SN explosion. The flat inner core at the beginning of our simulation (dotted) is 10^3 cm^{-3} , falling off approximately as $\propto r^{-2}$ at larger radii. The solid line shows the photo-heated gas after 3 Myr when the flat inner core was reduced to 30 cm^{-3} and bounded by a thick shell at 250 pc. The dotted line corresponds to the self-similar 1D numerical solution for a singular isothermal sphere with density $\propto r^{-2}$ (Wang et al., 2012). By interpolating the parameters from Table 1 in Shu et al. (2002) for $\epsilon = T_i/T_{\text{HII}} = 9000/25000 = 0.36$, we get the input parameters $\alpha_0 = 0.389$ and $x_s = 2.237$. The central density floor in our simulation matches well with the 1D solution while the thick shell has evolved much further away from the point source. Since the gas in our simulation was initially collapsed into a thin disk, the spherically-averaged density profile within the radius of the disk is 2–3 times greater than the isothermal sphere and significantly steeper than $\propto r^{-2}$ outside the disk. The compacted density profile in our 3D simulation allowed the thick shell to advanced further in the 1D isothermal case.

5.3.2 Superbubble Expansion

The first SN remnant bubble did not grow large enough to encompass the entire star cluster radius before the second SN exploded on the opposite side, ~ 15 pc away. Shells from the first two SNe collided with one another, with the second shell overpowering the weakened, older shell. The mostly spherical bubbles merged into an elongated superbubble and preserved the asymmetry from the initial spatial offset. All subsequent SNe exploded within the interior of the combined SB where the density dropped as low as 10^{-4} cm^{-3} . At this density the radius to sweep up an equivalent mass is ~ 100 pc, roughly equal to the vertical scale height. New SNe crashed into the back of the SB shell while still in the free expansion phase and a reverse shock immediately propagated back through the freely expanding ejecta, heating it to extreme temperatures 10^8 – 10^9 K. The ejecta collided inelastically and condensed into the shell wall in unmixed layers similar to Ritter et al. (2015). The condensed layers quickly cooled to $\sim 10^4$ K. The lowest momentum ejecta that never reached the shell wall constituted the low density, hot interior of the bubble. The high pressure in the interior exerted a force on and contributed additional momentum to the shell as in the continuous PDS model.

In figure 5.3 we plot the radius of the SB over time using the maximum distance from the origin of any SN to its most distant tracer particle. The first SN initially evolves as a single SN, where at very early time $t < t_{\text{rad}}$ the expansion is reasonably fit by the analytical ST solution (*dashed line*, equation 5.13), scaled to the density of the central gas cloud $n_{\text{amb}} \sim 30$. The simulated remnant becomes radiative at about 2 kyr due to interaction with the non-uniform background medium, quite a bit earlier than the time predicted by the analytical solution at 7.7 kyr, however by the time of the second explosion at $t = \Delta t_{\text{sn}} = 66$ kyr the simulated snowplow had caught up with the analytical snowplow solution (equation 5.22). Because the second SN occurred outside of the expanded remnant from the first SN, it wasn't until the third SN at $t = 2\Delta t_{\text{sn}}$ that we see the now-merged SB reinvigorated. All SNe exploded within the bubble at later times $t > 2\Delta t_{\text{sn}}$ and the simulated evolution matches the analytical solution for the continuous PDS (*dotted line*, equation 5.29), where we have lowered the fixed model density to $n_{\text{amb}} = 10 \text{ cm}^{-3}$ to account for the decreasing ambient density gradient outside the central cloud.

The phase plot of gas radial velocity as a function of distance from the center of the SB at $t = 1.9$ Myr is shown in figure 5.4, with the color scale showing mass-averaged temperature in each bin. Prominent in the region between 25 and 90 pc is the asymmetric snowplow

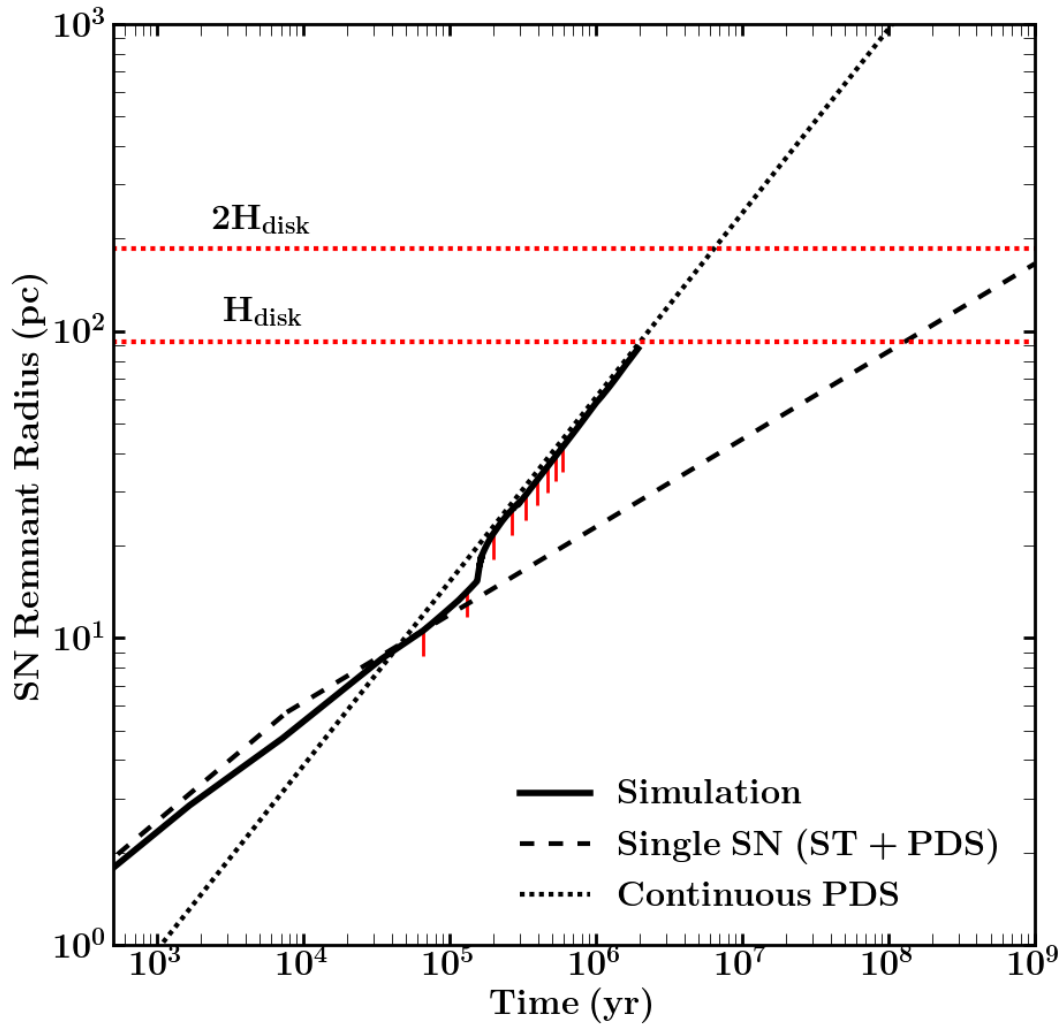


Figure 5.3: Maximum radius of the SB as a function of time (solid black), defined by the maximum distance from any SN explosion origin to its farthest tracer particle. The black dashed line shows the ST and PDS phase evolution for a single SN with fixed ambient density $n_{\text{amb}} \sim 30 \text{ cm}^{-3}$. The black dotted line shows the evolution of a continuous PDS with $\Delta t_{\text{sn}} = 66 \text{ kyr}$, where the ambient density $n_{\text{amb}} \sim 10 \text{ cm}^{-3}$ has been reduced to account for the decreasing density gradient outside the vicinity of the central gas cloud. Horizontal red dotted lines mark the scale height H and $2H$. The red vertical ticks indicate the temporal position of SNe numbers 2 through 10.

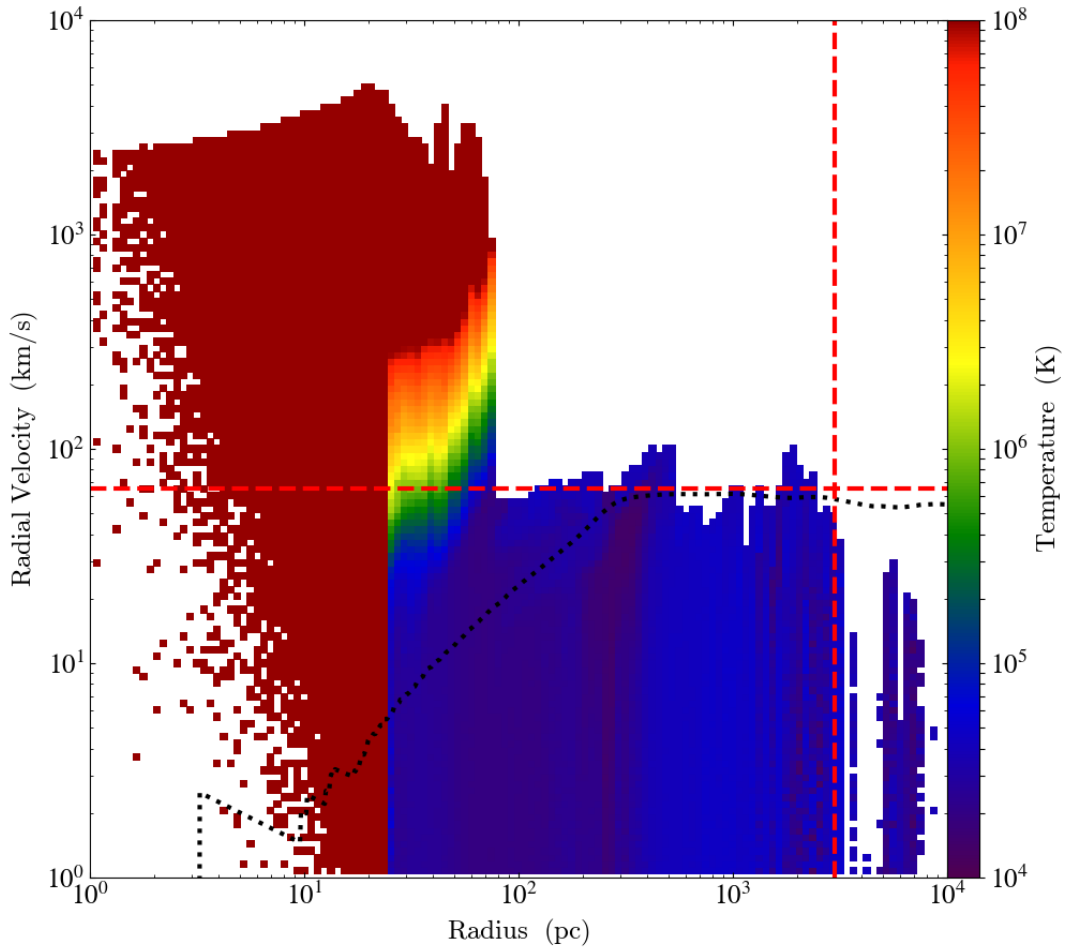


Figure 5.4: Phase plot of the radius vs radial velocity at $t = 1.9\text{ Myr}$ after the first SN, with the mass-averaged temperature in color. The black dotted line approximates the local escape velocity $v_{\text{escape}} \sim \sqrt{2GM(r)/r}$. The red dashed lines represent the galaxy escape velocity (horizontal) and the virial radius of the galaxy (vertical). Note the temperature gradient between 25 and 90 pc that highlights the asymmetrical snowplow shell, and the presence of fast-moving hot gas behind it.

shell, highlighted by the temperature gradient that follows the transition from the hot tenuous interior into the cold swept up gas. The shell wall in the direction of the plane of the galactic disk has only reached about 25 pc, while the vertical extent perpendicular to the plane of the disk extends up to 90 pc where the shell has maximum thickness ~ 15 pc. The black dotted line traces the local escape velocity $v_{\text{escape}} \sim \sqrt{2GM(r)/r}$ as a function of radius. The horizontal red dashed line indicates the global escape velocity of the entire galaxy $v_{\text{escape}} \sim 65$ km/s. The cold shell has slowed below the global escape velocity, however the hot gas with $T \gtrsim 10^7$ K has sufficient radial velocity to escape once the shell breaks out of the galactic disk. The vertical red dashed line delineates the virial radius of the galaxy at $R_{\text{virial}} \sim 3$ kpc.

5.4 Discussion

5.4.1 Snowplow Breakout

Using the parameters from our simulation we expect the snowplow shell to reach the vertical scale height at $t_{\text{pds}}(H) \approx 1.935$ Myr (equation 5.31) after which time about $N_{\text{sn}} \approx 30$ SNe (equation 5.32) have exploded within the bubble. The hot tenuous interior remains contained within the inner wall of the snowplow shell, about ~ 10 pc behind the outer shell wall, and will reach the scale height roughly 1 Myr after the leading edge. By the time it reaches the edge of the galactic disk, the shell's expansion velocity has slowed to $v_{\text{pds,cont}}(t_{\text{pds}}(H)) \approx 27$ km/s (equation 5.33). This is still well above the ~ 10 km/s sound speed in the $\sim 10^4$ K photoionized ISM. From figure 5.3 we see that the expansion of the bubble is steadily progressing past H , towards $2H$ by which time it is expected to fragment and allow the hot interior to leak through. Figure 5.4 shows that the cold gas ($T \sim 10^4$ K) in the swept up shell does not have sufficient velocity to escape the halo (horizontal red dashed line) and will eventually stall somewhere in the halo near $2H$ when it slows to the local dynamical velocity (black dotted line).

The snowplow shell will continue past the edge of the photoheated disk, roughly 2 Myr after the first SN explosion, after having swept up a significant fraction of the mass contained within the scale height of the disk $M_{\text{shell}} = \rho_{\text{amb}}(4/3)\pi H^3 \sim 10^6 M_{\odot}$. The shell becomes sensitive to hydrodynamical instabilities (e.g. Vishniac, 1994) which can fragment it into cold clouds that preserve the snowplow density $\sim 10^2 \text{ cm}^{-3}$. Figure 5.4 indicates that the cold shell has insufficient radial velocity to escape the galaxy under its own momentum.

We therefore expect the cloud fragments to be deposited in the outer halo after breakout. Gaps between the cloud fragments could allow the hot interior to leak through, creating a galactic "chimney" that funnels hot gas with temperature $T_{\text{wind}} > 10^7$ K around the clouds and orthogonally out of the disk.

The shell fragments are heated and disrupted by the fast-moving hot wind on a shock-crossing time $t \sim r_{\text{cloud}}/v_{\text{wind}}$ (Klein, McKee & Colella, 1994; Poludnenko, Frank & Blackman, 2002). If the cooling time of the fragment $t \sim T/\dot{T}$ is shorter than the shock-crossing time, however, they will be condensed and shielded from disruption (Melioli, de Gouveia dal Pino & Raga, 2005). Numerical simulations indicate that a hot diffuse wind is unable to efficiently lift cold dense clouds out of the ISM unless the clouds are able to maintain integrity through some other mechanism, e.g. magnetic fields (McCourt et al., 2015). High-density clouds that interact with the wind tend to be shredded and mass-loaded into the wind rather than accelerated out of the disk whole (Cooper et al., 2009; Scannapieco & Brüggén, 2015; Brüggén & Scannapieco, 2016; Schneider & Robertson, 2017; Zhang et al., 2017). Kim, Ostriker & Raileanu (2017) indicate that the wind may not be significantly mass-loaded by the break up of the shell into cloud fragments until they reach a distance $2H$, or twice the scale height, which would take $t_{\text{pds}}(2H) \approx 6$ Myr in our simulation. The cold, shredded clouds are one possible explanation for the observations of filamentary structures embedded in the winds of starburst galaxies like M82 (Cooper et al., 2008).

5.4.2 Towards Simulating Galactic Outflows One Supernova at a Time

Although we assumed the $10^5 M_{\odot}$ star cluster in our simulation formed instantaneously, we may calculate the equivalent SFR \dot{M}_{*} ($M_{\odot} \text{yr}^{-1}$) for the purposes of comparing with models of mass-loading in galactic winds. If we integrate our power-law IMF $\propto M^{-\alpha} dM$ with exponent $\alpha = 2.3$ between 1 and $100 M_{\odot}$, we get an average of 1 SN per $50 M_{\odot}$ of stars formed. This gives us an estimate of the continuous SFR that has an equivalent SN rate

$$\begin{aligned} \dot{M}_{*} &= \frac{50 M_{\odot}}{\Delta t_{\text{sn}}} \\ &\approx 0.00076 M_{\odot} \text{yr}^{-1} \end{aligned} \tag{5.50}$$

We can estimate the lower limit for the mass-loading parameter due to SN ejecta alone

$$\begin{aligned}
\beta_{\text{sn}} &= \frac{\dot{M}_{\text{wind}}}{\dot{M}_{*}} \\
&= \frac{M_{\text{sn}}}{50 M_{\odot}} \\
&= 0.24
\end{aligned}
\tag{5.51}$$

which gives the expected value (Leitherer et al., 1999).

A warm phase can be created by the mixture of gas from cold clouds ablated by a hot metal-enriched wind (Cooper et al., 2009), otherwise warm gas may precipitate directly from the hot metal-enriched wind if it is especially mass-loaded and can cool effectively (Thompson et al., 2016). Kim, Ostriker & Raileanu (2017) suggest that a heavily mass-loaded wind with $\beta > 1$ is only possible if the conditions exist for the SB to break out of the disk prior to a shell forming, the hot breakout condition (equation 5.34), with an upper-limit $\beta \lesssim 10$ for SN-driven winds with extremely small Δt_{sn} . Their models with $\Delta t_{\text{sn}} = 100 \text{ kyr}$ marginally do not satisfy the hot breakout condition, and are likely the most representative of self-regulated galactic disks with moderate mass-loading $\beta \sim 1$. Unless the SFR is significantly above the time-averaged rate, the first SNe will generally undergo shell formation while still within the disk. Outflow simulations of galaxies with more modest Δt_{sn} require discrete SN energy input at high resolution to accurately reproduce the initial velocities of shocked gas (Dalla Vecchia & Schaye, 2008), and thus the momentum injected into the swept up snowplow shell before it breaks out of the galactic disk. Under the cold breakout condition (equation 5.36), a weak wind with small mass loading factors $\beta \lesssim 1$ could still be produced. The temporally and spatially averaged SFR is generally insufficient to drive a highly mass-loaded hot wind (Martizzi et al., 2016; Li, Bryan & Ostriker, 2017; Kim, Ostriker & Raileanu, 2017). Based on these conclusions, we expect a weak wind with $\beta \lesssim 1$ to develop in our simulation as it is continued.

The process of cloud shredding is likely to leave warm metal-enriched gas clumps embedded in the outflow. The hot chimney carved out of the galactic disk by the breakout of the snowplow shell not only provides a channel for the hot wind to leak through, but also allows resonant Ly α photons to escape from the central star cluster (Dijkstra & Kramer, 2012; Behrens, Dijkstra & Niemeyer, 2014). UV-illuminated metal-enriched gas clumps embedded in the outflows are one possible source for velocity-shifted metal-line emission routinely observed around star-forming galaxies. Outflow velocities can be measured from

the Doppler shift of strong line emission by gas clumps embedded in the outflow. In high-redshift galaxies $z \gtrsim 3$, outflow velocities are measured from the offset of OIII emitting gas clumps relative to the systemic redshift of the central Ly α emitting source (McLinden et al., 2011, 2014). OIII emission is also an effective tracer of star formation at high redshift where the H α line is no longer amenable to ground-based observations (Suzuki et al., 2016).

The simulation presented here is a first step toward generating a galactic outflow using SN remnants inserted at high-resolution into the realistically formed ISM of a small galaxy built from cosmological initial conditions. The conclusions that we can draw from the continuation of this simulation are key to understanding the clumpiness of the cold gas embedded in the hot outflows of small galaxies at high redshift. Maintaining this high resolution as the shell expands into the galactic halo will allow us to estimate the degree of coarse-grained mixing between the hot wind and shredded clouds, giving insight into the temperature, density, and metallicity in the mass-loaded outflow. This information may become especially pertinent to help guide observational interpretations from future missions such as James Webb Space Telescope that will look even further back in cosmic time and unlock the era of the first galaxies.

5.5 Summary

In this chapter we laid out the framework for simulating a galactic outflow by inserting individually resolved SN remnants, one at a time, with initial conditions dictated as much as possible by first principles. We started by extracting a $10^9 M_\odot$ dark matter halo with an embedded gaseous galactic disk from a larger cosmological hydrodynamical simulation, ensuring that our host galaxy had a realistic, non-uniform initial density structure. An instantaneously formed $10^5 M_\odot$ star cluster was inserted at the center of the galactic disk and the photoionization of the disk by stellar radiation was simulated in order to create a warm ionized phase and reproduce realistic conditions in the ISM of a small starburst galaxy. With the stage set, the mass and energy from a continuous succession of discrete SNe was injected, one SN at a time, by zooming in to ultra-high-resolution and inserting the remnants in the free expansion phase. We avoided making assumptions about the thermalization efficiency and density structure of each remnant by initializing them at a scale where their properties were still well-described by simple analytical arguments, before in-

teractions with the surrounding medium cause those arguments to break down. Using an adaptive mesh, we simultaneously resolved the individual remnants when they were inserted along with the prior SNe which had already merged into a much larger bubble. The evolution of a snowplow shell swept up by hot ejecta from the combined SNe was followed for 1.65 Myr until it had reached a distance of 80 pc, poised to break out of the galactic disk. The conditions within the snowplow shell and hot bubble just after breakout provide key insights into the thermodynamic and spectroscopic properties of the outflow that eventually develops.

Acknowledgements

The FLASH software used in this work was in part developed by the DOE NNSA-ASC OASCR Flash Center at the University of Chicago. The images in this publication were created using the YT visualization package (Turk et al., 2011) and the MATPLOTLIB plotting library (Hunter, 2007).

Chapter Six: Conclusion

The results from a cosmological hydrodynamical simulation designed to investigate the evolution of a cosmic minihalo in the aftermath of the formation of its first Pop III star are reported in chapter 2 (Ritter et al., 2012). Specifically, we tested the assumption that the first stars had more moderate masses ($\lesssim 100M_{\odot}$) and exploded as typical Type II-like core collapse SNe (10^{51} erg). Individual moderate-mass stars may only partially photoionize their host minihalo, such that the densest gas flowing from the filaments of the cosmic web may remain neutral. The neutral filaments could survive the passing SN shock intact provided the damage inflicted by SNe with moderate-mass progenitors is significantly less than that caused by ultra-energetic SNe, like the pair-instability SNe that are produced by stars with extreme masses $\gtrsim 140M_{\odot}$. The minihalo can resume accretion of the dense gas filaments back into the center only ~ 1 Myr after the explosion, with ejecta infall reaching a steady state after 5 Myr. Cosmic accretion into the center of the minihalo can fully recover after only ~ 20 Myr when the gas accretion rate reaches $\sim 0.002M_{\odot}\text{ yr}^{-1}$ and the average metallicity of the accreting matter is in the range $0.001\text{--}0.01Z_{\odot}$, sufficient to ensure that new stars forming in the central core will have even lower characteristic masses. Matching these high-redshift simulations with their possible local relics, such as the ultra-faint dwarf galaxies (e.g., Bovill & Ricotti, 2009; Salvadori & Ferrara, 2009; Tumlinson, 2010) and metal-poor globular clusters (e.g., Brodie & Strader, 2006), will provide intriguing insights into the nature of those ancient fossil stellar systems.

In chapter 3, we compared two complementary very-high-resolution cosmological simulations of how the metals produced in the first SN explosions are transported into the cold, dense gas out of which the second-generation of stars is formed. The first simulated the interaction of a single SN remnant with its host minihalo, tracking the ejecta with individually tagged passive tracer particles separated into equal mass radial bins (Sluder et al., 2016). The second simulated 7 discrete SN remnants exploding in the same minihalo, also tracking the ejecta from each SN with individually tagged tracer particles (Ritter et al., 2015). A common approach used in semi-analytical chemical enrichment models is to assume that SNe uniformly enrich a spherical volume centered on the explosion. This assumption depends on either the complete homogenization of ejecta within the remnant, or complete mixing promptly after interacting with the surrounding medium, neither of which are ex-

pected to occur in nature. In both simulations the ejecta and swept up material remain largely unmixed until after recondensing into the gravitational center where turbulence decreases the vortical timescale. These simulations highlight the inherently anisotropic hydrodynamic transport of ejecta by SNe interacting with a non-uniform medium. In particular, it was found that low-momentum ejecta from the inner region of a single remnant is preferentially mixed with the recondensing gas while the ejecta from outer layers is more likely to be ejected from the minihalo. When we consider the temporal displacement of 7 discrete SN explosions spread out over 4.5 Myr, the ejecta-enriched cloud that recondensed after 200 Myr was preferentially enriched by the earliest SNe. Hydrodynamical bias in the transport of metals by SNe requires that we rethink a number of the traditional assumptions and methodologies used in chemical enrichment models, and presents a challenge to the interpretations of near-field cosmology.

Chapter 4 demonstrates one possible pathway for the formation of extremely metal poor ($Z \sim 10^{-4}$ – $10^{-3} Z_{\odot}$) stars in cosmic minihalos enriched by single, low-energy core collapse supernovae, only ~ 10 Myr after the initial explosion. The short timescale of this pathway depends on the survival of a neutral gas cloud in the partially ionized HII region of the first star that can capture ejecta from the passing blast wave. The deposition of metals onto the surface of the cloud compresses it and enhances cooling that ultimately leads to gravitational collapse, allowing new metal-poor stars to form on shorter timescales, and at higher metallicities, than through the fallback of enriched ISM and IGM returning into the dark matter halo center. Simple analytical arguments suggest that surviving neutral clouds are generic in the HII regions of isolated moderate-mass stars in minihalos. This mechanism differs from other scenarios involving ultra-energetic SNe (Wise & Abel, 2008a; Greif et al., 2010), whose high-mass progenitors were bright enough to completely ionize the nearby ISM and ejected large metal masses ($\sim 50 M_{\odot}$) with 10–100 times more energy than typical low-energy core collapse SNe. The formation of very metal-poor stars enriched by these explosions requires dilution of the metal ejecta with a large volume of unenriched gas, over a much longer timescale, which allows for further enrichment by additional sources. The collapsing metal-enriched gas cloud in this simulation acquired its extremely low metallicity through superficial deposition by the passing blast wave. Enhanced cooling due to carbon and oxygen fine structure line emission effectively accelerates the collapse of the metal-enriched pre-stellar clump. If we assume the cloud was enriched by ejecta with the expected yields of Type II-like core collapse SNe, the range of possible metallicities and elemental abundances in the resulting stellar population match well with

the metallicities and abundances of the most extreme metal-poor stars known. We can now begin to understand the degeneracies in the initial chemical enrichment process and the pathways through which metal-enriched stars form.

The framework is laid out in chapter 5 for simulating a galactic outflow powered by a succession of discrete SN remnants, inserted one at a time in a realistically formed $10^9 M_{\odot}$ dark matter halo. The radiative feedback of a $10^5 M_{\odot}$ star cluster was simulated in the gaseous galactic disk at the center, creating the warm ionized ISM of a small starburst galaxy. SN remnants were inserted one at a time by zooming in to ultra-high-resolution and inserting them in the free expansion phase, before interactions with the surrounding medium cause the true evolution to significantly deviate from the analytical solution. We simultaneously resolved the individual remnants when they were inserted and the much larger superbubble formed from the merged remnants of prior SNe. This simulation indicates that it was possible for hot metal-enriched outflows, like the ones commonly observed in the outer halos of starburst galaxies, to develop in low mass galaxies with more modest star formation rates.

Bibliography

- Abel T., Bryan G. L., Norman M. L., 2000, *ApJ*, 540, 39
- Abel T., Bryan G. L., Norman M. L., 2002, *Science*, 295, 93
- Abel T., Wise J. H., Bryan G. L., 2007, *ApJ*, 659, L87
- Agertz O., Kravtsov A. V., Leitner S. N., Gnedin N. Y., 2013, *ApJ*, 770, 25
- Aguirre A., Schaye J., Kim T.-S., Theuns T., Rauch M., Sargent W. L. W., 2004, *ApJ*, 602, 38
- Alvarez M. A., Bromm V., Shapiro P. R., 2006, *ApJ*, 639, 621
- Alvarez M. A., Wise J. H., Abel T., 2009, *ApJ*, 701, L133
- Aoki W., Beers T. C., Honda S., Carollo D., 2010, *ApJ*, 723, L201
- Aoki W., Tominaga N., Beers T. C., Honda S., Lee Y. S., 2014, *Science*, 345, 912
- Argast D., Samland M., Gerhard O. E., Thielemann F.-K., 2000, *A&A*, 356, 873
- Arnett W. D., Meakin C., 2011, *ApJ*, 733, 78
- Audouze J., Silk J., 1995, *ApJ*, 451, L49
- Avedisova V. S., 1972, *Soviet Ast.*, 15, 708
- Bader G., Deuffhard P., 1983, *Numerische Mathematik*, 41, 373
- Barkana R., Loeb A., 1999, *ApJ*, 523, 54
- Bechtol K. et al., 2015, *ApJ*, 807, 50
- Becker G. D., Sargent W. L. W., Rauch M., Carswell R. F., 2012, *ApJ*, 744, 91
- Beers T. C., Christlieb N., 2005, *ARA&A*, 43, 531
- Behrens C., Dijkstra M., Niemeyer J. C., 2014, *A&A*, 563, A77

Beirão P. et al., 2015, MNRAS, 451, 2640

Bertoldi F., 1989, ApJ, 346, 735

Bertoldi F., McKee C. F., 1990, ApJ, 354, 529

Bertschinger E., 2001, ApJS, 137, 1

Bessell M. S. et al., 2015, ApJ, 806, L16

Bland-Hawthorn J., Karlsson T., Sharma S., Krumholz M., Silk J., 2010, ApJ, 721, 582

Bland-Hawthorn J., Sutherland R., Karlsson T., 2011, in EAS Publications Series, Vol. 48, EAS Publications Series, Koleva M., Prugniel P., Vauglin I., eds., pp. 397–404

Boley A. C., Lake G., Read J., Teyssier R., 2009, ApJ, 706, L192

Bovill M. S., Ricotti M., 2009, ApJ, 693, 1859

Bovill M. S., Ricotti M., 2011, ApJ, 741, 18

Brodie J. P., Strader J., 2006, ARA&A, 44, 193

Bromm V., 2013, Rep. on Prog. in Phys., 76, 112901

Bromm V., Clarke C. J., 2002, ApJ, 566, L1

Bromm V., Coppi P. S., Larson R. B., 1999, ApJ, 527, L5

Bromm V., Coppi P. S., Larson R. B., 2002, ApJ, 564, 23

Bromm V., Ferrara A., Coppi P. S., Larson R. B., 2001, MNRAS, 328, 969

Bromm V., Loeb A., 2003a, ApJ, 596, 34

Bromm V., Loeb A., 2003b, Nature, 425, 812

Bromm V., Yoshida N., 2011, ARA&A, 49, 373

Bromm V., Yoshida N., Hernquist L., 2003, ApJ, 596, L135

Brown T. M. et al., 2012, ApJ, 753, L21

Brüggen M., Scannapieco E., 2016, ApJ, 822, 31

Burkert A., Schartmann M., Alig C., Gillessen S., Genzel R., Fritz T., Eisenhauer F., 2012, ApJ, 750, 58

Busha M. T., Alvarez M. A., Wechsler R. H., Abel T., Strigari L. E., 2010, ApJ, 710, 408

Caffau E. et al., 2011, Nature, 477, 67

Castor J., McCray R., Weaver R., 1975, ApJ, 200, L107

Cayrel R. et al., 2004, A&A, 416, 1117

Cayrel R. et al., 2001, Nature, 409, 691

Chabrier G., 2003, PASP, 115, 763

Chatzopoulos E., Wheeler J. C., 2012, ApJ, 748, 42

Chen K.-J., Heger A., Whalen D. J., Moriya T. J., Bromm V., Woosley S., Almgren A., 2016, ArXiv e-prints

Cherchneff I., Dwek E., 2009, ApJ, 703, 642

Cherchneff I., Dwek E., 2010, ApJ, 713, 1

Chevalier R. A., Clegg A. W., 1985, Nature, 317, 44

Chiaki G., Marassi S., Nozawa T., Yoshida N., Schneider R., Omukai K., Limongi M., Chieffi A., 2015, MNRAS, 446, 2659

Chiaki G., Schneider R., Nozawa T., Omukai K., Limongi M., Yoshida N., Chieffi A., 2014, MNRAS, 439, 3121

Chiaki G., Yoshida N., Kitayama T., 2013, ApJ, 762, 50

Chisholm J., Tremonti C. A., Leitherer C., Chen Y., Wofford A., Lundgren B., 2015, ApJ, 811, 149

Christlieb N. et al., 2002, Nature, 419, 904

Clark P. C., Glover S. C. O., Klessen R. S., Bromm V., 2011a, ApJ, 727, 110

Clark P. C., Glover S. C. O., Klessen R. S., Bromm V., 2011b, ApJ, 727, 110

Clark P. C., Glover S. C. O., Smith R. J., Greif T. H., Klessen R. S., Bromm V., 2011c, *Science*, 331, 1040

Cohen J. G., Christlieb N., Thompson I., McWilliam A., Shectman S., Reimers D., Wisotzki L., Kirby E., 2013, *ApJ*, 778, 56

Colella P., Glaz H., 1985, 59, 264

Colella P., Woodward P. R., 1984, *Journal of Computational Physics*, 54, 174

Contursi A. et al., 2013, *A&A*, 549, A118

Cooke R., Pettini M., Steidel C. C., Rudie G. C., Nissen P. E., 2011, *MNRAS*, 417, 1534

Cooke R. J., Madau P., 2014, *ApJ*, 791, 116

Cooke R. J., Pettini M., Jorgenson R. A., 2015, *ApJ*, 800, 12

Cooper J. L., Bicknell G. V., Sutherland R. S., Bland-Hawthorn J., 2008, *ApJ*, 674, 157

Cooper J. L., Bicknell G. V., Sutherland R. S., Bland-Hawthorn J., 2009, *ApJ*, 703, 330

Corlies L., Johnston K. V., Tumlinson J., Bryan G., 2013, *ApJ*, 773, 105

Couch S. M., Chatzopoulos E., Arnett W. D., Timmes F. X., 2015, *ArXiv e-prints*

Coughlin E. R., Nixon C., Begelman M. C., Armitage P. J., 2016, *MNRAS*, 459, 3089

Cowie L. L., McKee C. F., 1977, *ApJ*, 211, 135

Cowie L. L., Songaila A., Kim T.-S., Hu E. M., 1995, *AJ*, 109, 1522

Creasey P., Theuns T., Bower R. G., 2013, *MNRAS*, 429, 1922

Dalla Vecchia C., Schaye J., 2008, *MNRAS*, 387, 1431

De Silva G. M. et al., 2015, *MNRAS*, 449, 2604

Dekel A., Silk J., 1986, *ApJ*, 303, 39

Dijkstra M., Kramer R., 2012, *MNRAS*, 424, 1672

Dopita M. A., Koratkar A. P., Allen M. G., Tsvetanov Z. I., Ford H. C., Bicknell G. V., Sutherland R. S., 1997, *ApJ*, 490, 202

Draine B. T., 2011, *Physics of the Interstellar and Intergalactic Medium*

Drlica-Wagner A. et al., 2015, *ApJ*, 813, 109

Efstathiou G., 1992, *MNRAS*, 256, 43P

Einfeldt B., 1988, 25, 294

Ellinger C. I., Young P. A., Fryer C. L., Rockefeller G., 2012, *ApJ*, 755, 160

Elmegreen B. G., Kim S., Staveley-Smith L., 2001, *ApJ*, 548, 749

Erb D. K., 2008, *ApJ*, 674, 151

Fan X., Carilli C. L., Keating B., 2006, *ARA&A*, 44, 415

Feltzing S., Eriksson K., Kleyna J., Wilkinson M. I., 2009, *A&A*, 508, L1

Feng Y., Krumholz M. R., 2014, *Nature*, 513, 523

Ferland G. J., Korista K. T., Verner D. A., Ferguson J. W., Kingdon J. B., Verner E. M., 1998, *PASP*, 110, 761

Ferland G. J. et al., 2013, *Rev. Mexicana Astron. Astrofis.*, 49, 137

Filho M. E., Sánchez Almeida J., Amorín R., Muñoz-Tuñón C., Elmegreen B. G., Elmegreen D. M., 2016, *ApJ*, 820, 109

Finlator K., Davé R., 2008, *MNRAS*, 385, 2181

Font A. S. et al., 2011, *MNRAS*, 417, 1260

François P. et al., 2007, *A&A*, 476, 935

Frebel A. et al., 2005, *Nature*, 434, 871

Frebel A., Bromm V., 2012, *ApJ*, 759, 115

Frebel A., Johnson J. L., Bromm V., 2007, *MNRAS*, 380, L40

Frebel A., Norris J. E., 2013a, *Metal-Poor Stars and the Chemical Enrichment of the Universe*, Oswald T. D., Gilmore G., eds., p. 55

Frebel A., Norris J. E., 2013b, Metal-Poor Stars and the Chemical Enrichment of the Universe, Oswald T. D., Gilmore G., eds., p. 55

Frebel A., Norris J. E., 2015, *ARA&A*, 53, 631

Frebel A., Simon J. D., Geha M., Willman B., 2010, *ApJ*, 708, 560

Frebel A., Simon J. D., Kirby E. N., 2014, *ApJ*, 786, 74

Fryer C. L., Belczynski K., Wiktorowicz G., Dominik M., Kalogera V., Holz D. E., 2012, *ApJ*, 749, 91

Fryxell B. et al., 2000, *ApJS*, 131, 273

Furlanetto S. R., Oh S. P., Briggs F. H., 2006, *Phys. Rep.*, 433, 181

Gao L., Theuns T., Frenk C. S., Jenkins A., Helly J. C., Navarro J., Springel V., White S. D. M., 2010, *MNRAS*, 403, 1283

Gao L., Yoshida N., Abel T., Frenk C. S., Jenkins A., Springel V., 2007, *MNRAS*, 378, 449

Gilmore G., Norris J. E., Monaco L., Yong D., Wyse R. F. G., Geisler D., 2013, *ApJ*, 763, 61

Gilmore G., Randich S., Asplund M., et al., 2012, *The Messenger*, 147, 25

Glover S. C. O., Abel T., 2008, *MNRAS*, 388, 1627

Glover S. C. O., Clark P. C., 2014, *MNRAS*, 437, 9

Gnat O., Ferland G. J., 2012, *ApJS*, 199, 20

Gnat O., Sternberg A., 2007, *ApJS*, 168, 213

Gnedin N. Y., Kravtsov A. V., 2006, *ApJ*, 645, 1054

Goldbaum N. J., Krumholz M. R., Matzner C. D., McKee C. F., 2011, *ApJ*, 738, 101

Górski K. M., Hivon E., Banday A. J., Wandelt B. D., Hansen F. K., Reinecke M., Bartelmann M., 2005, *ApJ*, 622, 759

Greif T. H., Bromm V., Clark P. C., Glover S. C. O., Smith R. J., Klessen R. S., Yoshida N., Springel V., 2012, *MNRAS*, 424, 399

Greif T. H., Glover S. C. O., Bromm V., Klessen R. S., 2010, ApJ, 716, 510

Greif T. H., Johnson J. L., Bromm V., Klessen R. S., 2007, ApJ, 670, 1

Greif T. H., Springel V., White S. D. M., Glover S. C. O., Clark P. C., Smith R. J., Klessen R. S., Bromm V., 2011, ApJ, 737, 75

Griffen B. F., Drinkwater M. J., Thomas P. A., Helly J. C., Pimblett K. A., 2010, MNRAS, 405, 375

Grimes J. P. et al., 2009, ApJS, 181, 272

Guillochon J., Ramirez-Ruiz E., 2013, ApJ, 767, 25

Heckman T. M., Alexandroff R. M., Borthakur S., Overzier R., Leitherer C., 2015, ApJ, 809, 147

Heckman T. M., Armus L., Miley G. K., 1990, ApJS, 74, 833

Heckman T. M., Borthakur S., 2016, ApJ, 822, 9

Heckman T. M., Lehnert M. D., Strickland D. K., Armus L., 2000, ApJS, 129, 493

Heckman T. M., Thompson T. A., 2017, Galactic Winds and the Role Played by Massive Stars, Alsabti A. W., Murdin P., eds., p. 2431

Heger A., Fryer C. L., Woosley S. E., Langer N., Hartmann D. H., 2003, ApJ, 591, 288

Heger A., Woosley S. E., 2002, ApJ, 567, 532

Heger A., Woosley S. E., 2010, ApJ, 724, 341

Hoopes C. G. et al., 2005, ApJ, 619, L99

Hosokawa T., Omukai K., Yorke H. W., 2012, ApJ, 756, 93

Hosokawa T., Omukai K., Yoshida N., Yorke H. W., 2011, Science, 334, 1250

Howes L. M. et al., 2015, Nature, 527, 484

Hummel J. A., Pawlik A. H., Milosavljević M., Bromm V., 2012, ApJ, 755, 72

Hunter J. D., 2007, Computing In Science & Engineering, 9, 90

Ishigaki M. N., Tominaga N., Kobayashi C., Nomoto K., 2014, ApJ, 792, L32

Iwamoto N., Umeda H., Tominaga N., Nomoto K., Maeda K., 2005, Science, 309, 451

Jeon M., Pawlik A. H., Bromm V., Milosavljević M., 2014, MNRAS, 444, 3288

Jeon M., Pawlik A. H., Greif T. H., Glover S. C. O., Bromm V., Milosavljević M., Klessen R. S., 2012, ApJ, 754, 34

Ji A. P., Frebel A., Bromm V., 2014, ApJ, 782, 95

Joggerst C. C., Almgren A., Bell J., Heger A., Whalen D., Woosley S. E., 2010, ApJ, 709, 11

Johnson J. L., Bromm V., 2006, MNRAS, 366, 247

Johnson J. L., Greif T. H., Bromm V., Klessen R. S., Ippolito J., 2009, MNRAS, 399, 37

Johnson J. L., Khochfar S., 2011, ApJ, 743, 126

Kang H., Shapiro P. R., 1992, ApJ, 386, 432

Karlsson T., 2005, A&A, 439, 93

Karlsson T., Bland-Hawthorn J., Freeman K. C., Silk J., 2012, ApJ, 759, 111

Karlsson T., Bromm V., Bland-Hawthorn J., 2013, Rev. Mod. Phys., 85, 809

Karlsson T., Gustafsson B., 2005, A&A, 436, 879

Karlsson T., Johnson J. L., Bromm V., 2008, ApJ, 679, 6

Keller S. C. et al., 2014, Nature, 506, 463

Kennicutt, Jr. R. C., 1998, ApJ, 498, 541

Kepner J. V., Babul A., Spergel D. N., 1997, ApJ, 487, 61

Kim C.-G., Kim W.-T., Ostriker E. C., 2011, ApJ, 743, 25

Kim C.-G., Ostriker E. C., Raileanu R., 2017, ApJ, 834, 25

Kirby E. N., Cohen J. G., Guhathakurta P., Cheng L., Bullock J. S., Gallazzi A., 2013, ApJ, 779, 102

Kirby E. N., Simon J. D., Geha M., Guhathakurta P., Frebel A., 2008, ApJ, 685, L43

Kitayama T., Yoshida N., 2005, ApJ, 630, 675

Kitayama T., Yoshida N., Susa H., Umemura M., 2004, ApJ, 613, 631

Klein R. I., McKee C. F., Colella P., 1994, ApJ, 420, 213

Kobayashi C., Ishigaki M. N., Tominaga N., Nomoto K., 2014, ApJ, 785, L5

Kohri K., Narayan R., Piran T., 2005, ApJ, 629, 341

Komatsu E. et al., 2011, ApJS, 192, 18

Koposov S. E., Belokurov V., Torrealba G., Evans N. W., 2015, ApJ, 805, 130

Koposov S. E., Yoo J., Rix H.-W., Weinberg D. H., Macciò A. V., Escudé J. M., 2009, ApJ, 696, 2179

Kravtsov A. V., Gnedin O. Y., 2005, ApJ, 623, 650

Kuhlen M., Madau P., 2005, MNRAS, 363, 1069

Lai D. K., Bolte M., Johnson J. A., Lucatello S., Heger A., Woosley S. E., 2008, ApJ, 681, 1524

Lai D. K., Lee Y. S., Bolte M., Lucatello S., Beers T. C., Johnson J. A., Sivarani T., Rockosi C. M., 2011, ApJ, 738, 51

Latif M. A., Schleicher D. R. G., Schmidt W., Niemeyer J., 2013, MNRAS, 432, 668

Lee D. M., Johnston K. V., Tumlinson J., Sen B., Simon J. D., 2013, ApJ, 774, 103

Lehnert M. D., Heckman T. M., Weaver K. A., 1999, ApJ, 523, 575

Leitherer C. et al., 1999, ApJS, 123, 3

Leroy A. K. et al., 2015, ApJ, 814, 83

Li M., Bryan G. L., Ostriker J. P., 2017, ApJ, 841, 101

Li Y., 2011, ArXiv e-prints

Lindner C. C., Milosavljević M., Shen R., Kumar P., 2012, ApJ, 750, 163

Lopez L. A., Krumholz M. R., Bolatto A. D., Prochaska J. X., Ramirez-Ruiz E., 2011, ApJ, 731, 91

Lunnan R., Vogelsberger M., Frebel A., Hernquist L., Lidz A., Boylan-Kolchin M., 2012, ApJ, 746, 109

Lynds C. R., Sandage A. R., 1963, ApJ, 137, 1005

Mac Low M.-M., Shull J. M., 1986, ApJ, 302, 585

Macciò A. V., Kang X., Fontanot F., Somerville R. S., Kogosov S., Monaco P., 2010, MNRAS, 402, 1995

MacFadyen A. I., Woosley S. E., 1999, ApJ, 524, 262

MacFadyen A. I., Woosley S. E., Heger A., 2001, ApJ, 550, 410

Machida M. N., Tomisaka K., Nakamura F., Fujimoto M. Y., 2005, ApJ, 622, 39

Mackey J., Bromm V., Hernquist L., 2003, ApJ, 586, 1

MacNeice P., Center. G. S. F., 1999, PARAMESH, a parallel adaptive mesh refinement community toolkit [microform] / Peter MacNeice ... [et al.]. National Aeronautics and Space Administration, Goddard Space Flight Center ; National Technical Information Service, distributor Greenbelt, Md. : Springfield, VA, p. 1 v.

Madau P., Diemand J., Kuhlen M., 2008, ApJ, 679, 1260

Madau P., Ferrara A., Rees M. J., 2001, ApJ, 555, 92

Maeder A., Meynet G., 2012, Reviews of Modern Physics, 84, 25

Maio U., Ciardi B., Dolag K., Tornatore L., Khochfar S., 2010, MNRAS, 407, 1003

Marassi S., Chiaki G., Schneider R., Limongi M., Omukai K., Nozawa T., Chieffi A., Yoshida N., 2014, ApJ, 794, 100

Marassi S., Schneider R., Limongi M., Chieffi A., Bocchio M., Bianchi S., 2015, MNRAS, 454, 4250

Marlowe A. T., Heckman T. M., Wyse R. F. G., Schommer R., 1995, ApJ, 438, 563

Martin C. L., 1998, ApJ, 506, 222

Martin C. L., 2005, ApJ, 621, 227

Martin C. L., Kobulnicky H. A., Heckman T. M., 2002, ApJ, 574, 663

Martin C. L., Shapley A. E., Coil A. L., Kornei K. A., Bundy K., Weiner B. J., Noeske K. G., Schiminovich D., 2012, ApJ, 760, 127

Martizzi D., Fielding D., Faucher-Giguère C.-A., Quataert E., 2016, MNRAS, 459, 2311

Mashchenko S., Wadsley J., Couchman H. M. P., 2008, Science, 319, 174

McCourt M., O’Leary R. M., Madigan A.-M., Quataert E., 2015, MNRAS, 449, 2

McCray R., Kafatos M., 1987, ApJ, 317, 190

McKee C. F., Tan J. C., 2008, ApJ, 681, 771

McLinden E. M. et al., 2011, ApJ, 730, 136

McLinden E. M., Rhoads J. E., Malhotra S., Finkelstein S. L., Richardson M. L. A., Smith B., Tilvi V. S., 2014, MNRAS, 439, 446

Meece G. R., Smith B. D., O’Shea B. W., 2014, ApJ, 783, 75

Melioli C., de Gouveia dal Pino E. M., Raga A., 2005, A&A, 443, 495

Mesinger A., Bryan G. L., Haiman Z., 2006, ApJ, 648, 835

Mesinger A., Dijkstra M., 2008, MNRAS, 390, 1071

Milosavljević M., Bromm V., Couch S. M., Oh S. P., 2009, ApJ, 698, 766

Milosavljević M., Couch S. M., Bromm V., 2009, ApJ, 696, L146

Milosavljević M., Lindner C. C., Shen R., Kumar P., 2012, ApJ, 744, 103

Milosavljević M., Safranek-Shrader C., 2016, in Astrophysics and Space Science Library, Vol. 423, Astrophysics and Space Science Library, Mesinger A., ed., p. 65

Moore B., Diemand J., Madau P., Zemp M., Stadel J., 2006, MNRAS, 368, 563

Morales M. F., Wyithe J. S. B., 2010, ARA&A, 48, 127

Mori M., Ferrara A., Madau P., 2002, ApJ, 571, 40

Muñoz J. A., Madau P., Loeb A., Diemand J., 2009, MNRAS, 400, 1593

Muratov A. L., Gnedin O. Y., Gnedin N. Y., Zemp M., 2013, ApJ, 773, 19

Murray N., 2011, ApJ, 729, 133

Murray N., Quataert E., Thompson T. A., 2010, ApJ, 709, 191

Nagakura T., Omukai K., 2005, MNRAS, 364, 1378

Nakasato N., Shigeeyama T., 2000, ApJ, 541, L59

Nomoto K., Kobayashi C., Tominaga N., 2013, ARA&A, 51, 457

Norris J. E., Gilmore G., Wyse R. F. G., Yong D., Frebel A., 2010a, ApJ, 722, L104

Norris J. E. et al., 2013, ApJ, 762, 28

Norris J. E., Yong D., Gilmore G., Wyse R. F. G., 2010b, ApJ, 711, 350

Oey M. S., 2000, ApJ, 542, L25

Oey M. S., 2003, MNRAS, 339, 849

Oh S. P., Haiman Z., 2002, ApJ, 569, 558

Okamoto T., Frenk C. S., Jenkins A., Theuns T., 2010, MNRAS, 406, 208

Okamoto T., Gao L., Theuns T., 2008, MNRAS, 390, 920

Omukai K., Hosokawa T., Yoshida N., 2010, ApJ, 722, 1793

Omukai K., Tsuribe T., Schneider R., Ferrara A., 2005, ApJ, 626, 627

Oppenheimer B. D., Davé R., 2006, MNRAS, 373, 1265

O'Shea B. W., Norman M. L., 2007, ApJ, 654, 66

O'Shea B. W., Norman M. L., 2008, *ApJ*, 673, 14

O'Shea B. W., Wise J. H., Xu H., Norman M. L., 2015, *ApJ*, 807, L12

Osterbrock D. E., Ferland G. J., 2006, *Astrophysics of gaseous nebulae and active galactic nuclei*

Ostriker E. C., Shetty R., 2011, *ApJ*, 731, 41

Pan L., Scannapieco E., 2010, *ApJ*, 721, 1765

Pan L., Scannapieco E., Scalo J., 2012, *Journal of Fluid Mechanics*, 700, 459

Pan L., Scannapieco E., Scalo J., 2012, *Journal of Fluid Mechanics*, 700, 459

Pan T., Kasen D., Loeb A., 2012, *MNRAS*, 422, 2701

Park K., Ricotti M., 2011, *ApJ*, 739, 2

Park K., Ricotti M., 2012, *ApJ*, 747, 9

Pawlik A. H., Milosavljević M., Bromm V., 2013a, *ApJ*, 767, 59

Pawlik A. H., Milosavljević M., Bromm V., 2013b, *ApJ*, 767, 59

Peebles P. J. E., 1984, *ApJ*, 277, 470

Peeples M. S., Shankar F., 2011, *MNRAS*, 417, 2962

Pettini M., Shapley A. E., Steidel C. C., Cuby J.-G., Dickinson M., Moorwood A. F. M., Adelberger K. L., Giavalisco M., 2001, *ApJ*, 554, 981

Planck Collaboration, Ade P. A. R., Aghanim N., et al., 2016, *A&A*, 594, A13

Plewa T., Müller E., 1999, *A&A*, 342, 179

Poludnenko A. Y., Frank A., Blackman E. G., 2002, *ApJ*, 576, 832

Pritchard J. R., Loeb A., 2012, *Reports on Progress in Physics*, 75, 086901

Qian Y.-Z., Wasserburg G. J., 2002, *ApJ*, 567, 515

Qian Y.-Z., Wasserburg G. J., 2008, *ApJ*, 687, 272

Raiter A., Schaerer D., Fosbury R. A. E., 2010, A&A, 523, A64

Rashkov V., Madau P., Kuhlen M., Diemand J., 2012, ApJ, 745, 142

Rees M. J., Ostriker J. P., 1977, MNRAS, 179, 541

Ricker P. M., 2008, ApJS, 176, 293

Ricotti M., Gnedin N. Y., 2005, ApJ, 629, 259

Ricotti M., Gnedin N. Y., Shull J. M., 2008, ApJ, 685, 21

Ritter J. S., Safrank-Shrader C., Gnat O., Milosavljević M., Bromm V., 2012, ApJ, 761, 56

Ritter J. S., Safrank-Shrader C., Milosavljević M., Bromm V., 2016, MNRAS, 463, 3354

Ritter J. S., Sluder A., Safrank-Shrader C., Milosavljević M., Bromm V., 2015, MNRAS, 451, 1190

Rosenblatt E. I., Faber S. M., Blumenthal G. R., 1988, ApJ, 330, 191

Rupke D. S., Veilleux S., Sanders D. B., 2005, ApJS, 160, 115

Safrank-Shrader C., Agarwal M., Federrath C., Dubey A., Milosavljević M., Bromm V., 2012, MNRAS, 426, 1159

Safrank-Shrader C., Bromm V., Milosavljević M., 2010, ApJ, 723, 1568

Safrank-Shrader C., Milosavljević M., Bromm V., 2014a, MNRAS, 440, L76

Safrank-Shrader C., Milosavljević M., Bromm V., 2014b, MNRAS, 438, 1669

Salpeter E. E., 1955, ApJ, 121, 161

Salvadori S., Ferrara A., 2009, MNRAS, 395, L6

Salvaterra R., Ferrara A., Schneider R., 2004, New A, 10, 113

Santoro F., Shull J. M., 2006, ApJ, 643, 26

Sarangi A., Cherchneff I., 2015, A&A, 575, A95

Sarkar K. C., Nath B. B., Sharma P., Shehekinov Y., 2015, MNRAS, 448, 328

Scannapieco E., 2017, ApJ, 837, 28

Scannapieco E., Brüggén M., 2015, ApJ, 805, 158

Scannapieco E., Ferrara A., Madau P., 2002, ApJ, 574, 590

Scannapieco E., Thacker R. J., Davis M., 2001, ApJ, 557, 605

Schaerer D., 2002, A&A, 382, 28

Schaerer D., 2003, A&A, 397, 527

Schaye J., Aguirre A., Kim T.-S., Theuns T., Rauch M., Sargent W. L. W., 2003, ApJ, 596, 768

Schneider E. E., Robertson B. E., 2017, ApJ, 834, 144

Schneider E. E., Robertson B. E., 2018, ApJ, 860, 135

Schneider R., Omukai K., Inoue A. K., Ferrara A., 2006, MNRAS, 369, 1437

Schneider R., Omukai K., Limongi M., Ferrara A., Salvaterra R., Chieffi A., Bianchi S., 2012, MNRAS, 423, L60

Sedov L. I., 1959, *Similarity and Dimensional Methods in Mechanics*

Shapiro P. R., Iliiev I. T., Raga A. C., 2004, MNRAS, 348, 753

Shapiro P. R., Kang H., 1987, ApJ, 318, 32

Shen S., Cooke R. J., Ramirez-Ruiz E., Madau P., Mayer L., Guedes J., 2015, ApJ, 807, 115

Shigeyama T., Tsujimoto T., 1998, ApJ, 507, L135

Shopbell P. L., Bland-Hawthorn J., 1998, ApJ, 493, 129

Shu F. H., Lizano S., Galli D., Cantó J., Laughlin G., 2002, ApJ, 580, 969

Simon J. D., Jacobson H. R., Frebel A., Thompson I. B., Adams J. J., Shectman S. A., 2015, ApJ, 802, 93

Sluder A., Ritter J. S., Safrank-Shrader C., Milosavljević M., Bromm V., 2016, MNRAS, 456, 1410

Smith A., Safrank-Shrader C., Bromm V., Milosavljević M., 2015a, MNRAS, 449, 4336

Smith B., Sigurdsson S., Abel T., 2008, MNRAS, 385, 1443

Smith B. D., Turk M. J., Sigurdsson S., O’Shea B. W., Norman M. L., 2009, ApJ, 691, 441

Smith B. D., Wise J. H., O’Shea B. W., Norman M. L., Khochfar S., 2015b, MNRAS, 452, 2822

Snedden C., Cowan J. J., Gallino R., 2008, ARA&A, 46, 241

Snedden C., McWilliam A., Preston G. W., Cowan J. J., Burris D. L., Armosky B. J., 1996, ApJ, 467, 819

Springel V., 2005, MNRAS, 364, 1105

Stacy A., Bromm V., Lee A. T., 2016, MNRAS, 462, 1307

Stacy A., Bromm V., Loeb A., 2011, MNRAS, 413, 543

Stacy A., Greif T. H., Bromm V., 2010, MNRAS, 403, 45

Stacy A., Greif T. H., Bromm V., 2012a, MNRAS, 422, 290

Stacy A., Greif T. H., Bromm V., 2012b, MNRAS, 422, 290

Stacy A., Greif T. H., Klessen R. S., Bromm V., Loeb A., 2013, MNRAS, 431, 1470

Steidel C. C., Erb D. K., Shapley A. E., Pettini M., Reddy N., Bogosavljević M., Rudie G. C., Rakic O., 2010, ApJ, 717, 289

Sternberg A., Hoffmann T. L., Pauldrach A. W. A., 2003, ApJ, 599, 1333

Strickland D. K., Heckman T. M., 2009, ApJ, 697, 2030

Susa H., Umemura M., 2004a, ApJ, 600, 1

Susa H., Umemura M., 2004b, ApJ, 610, L5

Suzuki T. L. et al., 2016, MNRAS, 462, 181

Takahashi K., Umeda H., Yoshida T., 2014, ApJ, 794, 40

Talbot, Jr. R. J., Arnett W. D., 1973, ApJ, 186, 51

Tassis K., Gnedin N. Y., Kravtsov A. V., 2012, ApJ, 745, 68

Taylor G., 1950, Proceedings of the Royal Society of London Series A, 201, 159

Thompson T. A., Quataert E., Zhang D., Weinberg D. H., 2016, MNRAS, 455, 1830

Thornton K., Gaudlitz M., Janka H.-T., Steinmetz M., 1998, ApJ, 500, 95

Thoul A. A., Weinberg D. H., 1996, ApJ, 465, 608

Ting Y.-S., Freeman K. C., Kobayashi C., De Silva G. M., Bland-Hawthorn J., 2012, MNRAS, 421, 1231

Tremonti C. A. et al., 2004, ApJ, 613, 898

Truran J. W., Cowan J. J., Pilachowski C. A., Sneden C., 2002, PASP, 114, 1293

Tsujimoto T., Shigeyama T., 1998, ApJ, 508, L151

Tsujimoto T., Shigeyama T., Yoshii Y., 1999, ApJ, 519, L63

Tumlinson J., 2006, ApJ, 641, 1

Tumlinson J., 2010, ApJ, 708, 1398

Turk M. J., Smith B. D., Oishi J. S., Skory S., Skillman S. W., Abel T., Norman M. L., 2011, ApJS, 192, 9

van de Voort F., Quataert E., Hopkins P. F., Kereš D., Faucher-Giguère C.-A., 2015, MNRAS, 447, 140

Vangioni E., Silk J., Olive K. A., Fields B. D., 2011, MNRAS, 413, 2987

Vargas L. C., Geha M., Kirby E. N., Simon J. D., 2013, ApJ, 767, 134

Veilleux S., Rupke D. S. N., Swaters R., 2009, ApJ, 700, L149

Vishniac E. T., 1994, ApJ, 428, 186

Wada K., Venkatesan A., 2003, ApJ, 591, 38

Walker M. G., Mateo M., Olszewski E. W., 2008, ApJ, 688, L75

Wang F. Y., Bromm V., Greif T. H., Stacy A., Dai Z. G., Loeb A., Cheng K. S., 2012, ApJ, 760, 27

Weaver R., McCray R., Castor J., Shapiro P., Moore R., 1977, ApJ, 218, 377

Webster D., Frebel A., Bland-Hawthorn J., 2016, ApJ, 818, 80

Webster D., Sutherland R., Bland-Hawthorn J., 2014, ApJ, 796, 11

Whalen D., Abel T., Norman M. L., 2004, ApJ, 610, 14

Whalen D., Norman M. L., 2008, ApJ, 673, 664

Whalen D., van Veelen B., O'Shea B. W., Norman M. L., 2008a, ApJ, 682, 49

Whalen D., van Veelen B., O'Shea B. W., Norman M. L., 2008b, ApJ, 682, 49

Whalen D. J., Fryer C. L., 2012, ApJ, 756, L19

Whalen D. J., Fryer C. L., Holz D. E., Heger A., Woosley S. E., Stiavelli M., Even W., Frey L. H., 2013, ApJ, 762, L6

White S. D. M., Frenk C. S., 1991, ApJ, 379, 52

White S. D. M., Rees M. J., 1978, MNRAS, 183, 341

Wise J. H., Abel T., 2008a, ApJ, 685, 40

Wise J. H., Abel T., 2008b, ApJ, 685, 40

Wise J. H., Demchenko V. G., Halicek M. T., Norman M. L., Turk M. J., Abel T., Smith B. D., 2014, MNRAS, 442, 2560

Wise J. H., Turk M. J., Abel T., 2008, ApJ, 682, 745

Wise J. H., Turk M. J., Norman M. L., Abel T., 2012, ApJ, 745, 50

Wongwathanarat A., Janka H.-T., Müller E., 2013, A&A, 552, A126

- Wongwathanarat A., Müller E., Janka H.-T., 2015, *A&A*, 577, A48
- Yong D. et al., 2013a, *ApJ*, 762, 26
- Yong D. et al., 2013b, *ApJ*, 762, 26
- Yoon S.-C., Dierks A., Langer N., 2012, *A&A*, 542, A113
- Yoshida N., Bromm V., Hernquist L., 2004, *ApJ*, 605, 579
- Yoshida N., Oh S. P., Kitayama T., Hernquist L., 2007, *ApJ*, 663, 687
- Zackrisson E., Rydberg C.-E., Schaerer D., Östlin G., Tuli M., 2011, *ApJ*, 740, 13
- Zhang C., Zhang H., Yuan S., Liu S., Zhang T.-J., Sun Y.-C., 2014, *Research in Astronomy and Astrophysics*, 14, 1221
- Zhang D., Thompson T. A., Quataert E., Murray N., 2017, *MNRAS*, 468, 4801
- Zhang W., Woosley S. E., Heger A., 2008, *ApJ*, 679, 639
- Zucker D. B., de Silva G., Freeman K., Bland-Hawthorn J., Hermes Team, 2012, in *Astronomical Society of the Pacific Conference Series*, Vol. 458, *Galactic Archaeology: Near-Field Cosmology and the Formation of the Milky Way*, Aoki W., Ishigaki M., Suda T., Tsujimoto T., Arimoto N., eds., p. 421